Index 35726 X
ISSN 0867-888X

POLISH
ACADEMY
OF SCIENCES
INSTITUTE
OF FUNDAMENTAL
TECHNOLOGICAL
RESEARCH

NATIONAL
ENGINEERING
SCHOOL
OF METZ

ENGINEERING TRANSACTIONS

ROZPRAWY INŻYNIERSKIE - TRAITE d'INGENIERIE

QUARTERLY
VOLUME 60
ISSUE 1

WARSZAWA - METZ 2012

Faster online
http://et.ippt.gov.pl

Contents of issue 1 vol. LX

From the Editorial Board

The Editorial Committee wishes to express many thanks and appreciation to all the referees, listed below, for their valuable opinions concerning papers submitted to the Engineering Transactions in 2011:

A. Blinowski
A. Bragov
M. Daimaruya
P. Forquin
W. Gambin
J. Gawinecki
J. Janiszewski
P. Konderla
M. Kotełko
K. Kowalczyk–Gajewska
Z.L. Kowalewski
L. Kruszka
D. Krzysztoń
P. Lipiński
T. Łodygowski
G.L. Łukaszewicz
J. Maciejewski
M. Magier
A. Manes
E. Markiewicz
Z. Nowak
J. Ostrowska–Maciejewska
R. Pęcherski
H. Petryk
V. Pushkov
W.G. Proud
J.A. Rodriquez
J. Rońda
Z. Rosenberg
A. Rusinek
S. Stupkiewicz
Z. Szcześniak
T. Szolc
R. Trębiński
Y. Vorobiev
S. Wolny
T. Yokoyama

ENGINEERING TRANSACTIONS

Founded 1952
Appears since 1953

Aims and Scope

ENGINEERING TRANSACTIONS promotes research and practise in engineering science and provides a forum for interdisciplinary publications combining mechanics with material science, electronics (mechanotronics), medical science and biotechnologies (biomechanics), environmental science, photonics, information technologies and other engineering applications. The Journal publishes original papers covering a broad area of research activities including experimental and hybrid techniques as well as analytical and numerical approaches. Engineering Transactions is a quarterly issued journal for researchers in academic and industrial communities.

Address of the Editorial Office:
Engineering Transactions
Institute of Fundamental Technological Research
Pawińskiego 5B
PL 02-106 Warsaw, Poland

Phone: (48-22) 826 12 81 ext. 206, Fax: (48-22) 826 98 15, E-mail: engtrans@ippt.pan.pl

Abstracted/indexed in:

Applied Mechanics Reviews, Current Mathematical Publications, Inspec, Mathematical Reviews, MathSci, Zentralblatt für Mathematik.

http://et.ippt.pan.pl/

Address of the Editorial Office:
Engineering Transactions
Institute of Fundamental Technological Research
Pawińskiego 5B
PL 02-106 Warsaw, Poland
Phone: (48-22) 826 12 81 ext. 206, Fax: (48-22) 826 98 15
E-mail: engtrans@ippt.pan.pl

SUBSCRIPTIONS

Subscription orders for all journals edited by Institute of Fundamental Technological Research (IPPT) may be sent directly to the Publisher: Institute of Fundamental Technological Research
e-mail: subscribe@ippt.pan.pl

Please transfer the subscription fee to our bank account:
Payee: IPPT PAN
Bank: Pekao S.A. IV O/Warszawa
Account number 05124010531111000004426875.

WARUNKI PRENUMERATY

Prenumeratę na wszystkie czasopisma wydawane przez Instytut Podstawowych Problemów Techniki PAN przyjmuje Dział Wydawnictw IPPT.

Bieżące numery Engineering Transactions można nabyć bezpośrednio w Redakcji:
ul. Pawińskiego 5B, 02-106 Warszawa
Tel.: (48-22) 826 60 22; Fax: (48-22) 826 98 15
e-mail: subscribe@ippt.pan.pl

Arkuszy wydawniczych 7.50; Arkuszy drukarskich 6.00
Papier offset. kl. III 80 g.
Skład w systemie LaTeX K. Jezierska

ZAKŁAD MECHANIKI OŚRODKÓW CIĄGŁYCH
POLSKIEJ AKADEMII NAUK

ROZPRAWY INŻYNIERSKIE

I

FRANCISZEK SZELĄGOWSKI

Rozwiązanie zagadnienia płaskiego teorii sprężystości w układzie współrzędnych prostokątnych

O pewnych szczególnych przypadkach wytrzymałości tarczy nieograniczonej z odmiennym ośrodkiem zarysu eliptycznego

WARSZAWA 1953

ROZPRAWY INŻYNIERSKIE

ZAWIERAJĄ PRACE BADAWCZE Z ZAKRESU TEORII SPRĘŻYSTOŚCI I PLASTYCZNOŚCI, HYDRO- I AEROMECHANIKI, TERMODYNAMIKI ORAZ PODSTAWOWYCH PROBLEMÓW KONSTRUKCJI

Adres Redakcji
WARSZAWA, ul. Śniadeckich 8, I p.

PAŃSTWOWE WYDAWNICTWO NAUKOWE

ENGINEERING TRANSACTIONS • *Engng. Trans.* • **60**, 1, 3–14, 2012
Polish Academy of Sciences • Institute of Fundamental Technological Research (IPPT PAN)
National Engineering School of Metz (ENIM)
SIXTY YEARS OF THE ENGINEERING TRANSACTIONS

Development of a Soft Recovery System of Supersonic Projectiles

Dong-Teak CHUNG[1)], Ihnseok RHEE[1)], Byung Yun JOO[1)], Doo Han JIN[1)], One Kwon RIM[2)], Kwan Jin PARK[2)]

[1)] *The Korea University of Technology and Education*
School of Mechatronics and Mechanical Engineering
Cheonan, Chungnam, 330-708, the Republic of Korea
e-mail: dtchung@kut.ac.kr

[2)] *4-3, Agency for Defense Development*
Daejon, Chungnam, the Republic of Korea

An effective and robust soft recovery system for supersonic projectiles is required for the test of intelligent projectiles in development phase. The survivability of the projectiles after initial impact onto the target is the most important requirement of them. A soft recovery system, consisting of multiple equally spaced metal plates, was designed and fabricated. Numerical simulations were performed to estimate the deceleration of the projectile after piercing through a thin steel plate with various speeds. Next, the thickness distribution of the plate for uniform deceleration could be designed. An aluminum foil sensor system was used to measure the arrival time of the projectile onto each plate and multi-channel time recording system for this test was developed. Field tests were done using a rifled barrel gun and a smooth bore gun. Deceleration data were acquired successfully. The trajectories of the projectile after the impact tended to veer off from the initial firing line with an increasing yaw angle. Deceleration increased with the increase of the yaw angle. Field data were used to design a final recovery system to retrieve the projectile with a minimum deceleration and damage.

Key words: soft recovery, projectile, impact, simulation.

1. Introduction

In the field of modern weapon systems, a demand for smart and intelligent warheads with maximum effectiveness and minimum collateral damage is ever increasing. The survivability of the warheads after initial impact onto the target is the most crucial requirement of them. Traditional powder gun is the most common launching method but an initial acceleration may be too severe and may not guarantee the survival of the electronic components in the projectile.

Rocket launching method is available for a less severe initial acceleration but it requires vast resources and is time consuming. And the recovery of the projectile after initial impact with minimum damage is of the utmost importance to determine the survivability of the projectile. The technique for soft recovery of supersonic projectile is not well established yet. A few researches were published related to this subject [1]. For sub-sonic projectiles, various soft and light- weight materials are utilized to "catch" them, but in case of super-sonic projectiles the magnitude of initial deceleration is either too light or too severe and most often it ends with fractured projectiles. In this study, the numerical simulations were performed to estimate individual deceleration of the projectile after perforating the thin steel plates with various speeds. The analytical interpolation equations for the deceleration rate of projectile piercing through plates of different thickness were tabulated from the data. The optimum thickness distributions of the plates for overall uniform deceleration could be determined by utilizing the equations. And a soft recovery system, consisting of steel frame with multiple equally spaced metal plates, was designed and fabricated. Finally, the field tests were conducted using a 40 mm caliber rifled barrel gun and a 155 mm caliber smooth bore gun. The test results of 40 mm gun showed all the projectiles veered off from the initial firing line and exited at the midsection of the frame; the retrieved projectiles were damaged. The 155 mm gun test results were more satisfactory, i.e., a smooth deceleration span was much longer and the projectiles were recovered intact. Comparing the results from the two different guns we can conclude that the initial spin of the projectile attributes to faster yaw increase. Even with a perfect test condition the axis symmetric assumption cannot be maintained throughout the test. Hence, further numerical studies of three- dimensional oblique impact behavior of the projectile are required. More tests with different thickness distribution of the plates and careful alignment are needed to complete the soft recovery test.

2. Numerical simulation

At the design stage of the soft recovery system, the thickness distribution of 60 equally spaced metal plates for overall uniform deceleration of projectile was estimated by the axis-symmetric normal impact simulations, changing the striking velocity of a projectile to 200, 300, 400, 500, 600 m/s and the thickness of the plate to 0.6, 1.2, 2.3, 3.2 mm, respectively. For the simulation task, the two- dimensional Lagrangian explicit finite element program using quadrilateral element NET2D developed by Chung [2, 3] was used. The AISI 4340 steel projectile was assumed to be elastic. Dynamic behavior of the steel plate was assumed to be the Johnson-Cook model [4] as in Eq. (2.1) with material parameters as shown in Table 1. This model is the most widely used phenomeno-

Table 1. Johnson-Cook model parameters for a mild steel plate.

A [GPa]	B [GPa]	C [GPa]	n	m	T_{room} [°C]	T_{melt} [°C]
0.5320	0.2295	0.0274	0.3024	1.0	25	1520

logical ductile fracture model, which decomposes the total strain rate into an elastic and plastic portion, and involves five constants: A, B, C, n and m. It was also assumed that almost deformated energy is converted into a heat. In order to describe the ductile fracture and piercing of the plate material, the element erosion algorithm was used: when the equivalent plastic strain of an element exceeds 200%, the element is deleted and is excluded from further computation.

$$\sigma_y = (A + B\overline{\varepsilon_p}^n)\left(1 + C\log\left(\dot{\overline{\varepsilon_p}}\,/\,\dot{\overline{\varepsilon_0}}\right)\right)\left(1 - \frac{T - T_{\mathrm{room}}}{T_{\mathrm{melt}} - T_{\mathrm{room}}}\right)^m. \tag{2.1}$$

It was found that the velocity reduction factor (α) of a projectile, after piercing plate, depends on both the plate thickness and the striking velocity of a projectile as shown in Fig. 1; a thicker plate with slower striking velocity produced a high reduction factor. With the simulation results, the factor α was interpolated as Eq. (2.2).

$$\alpha(t_{\mathrm{sheet}}, V_{\mathrm{strinking}}) = a(t_{\mathrm{sheet}})\exp^{-V_{\mathrm{striking}}/\tau(t_{\mathrm{sheet}})} + b(t_{\mathrm{sheet}}), \tag{2.2}$$

where parametric values of a, τ, and b are summarized in Table 2.

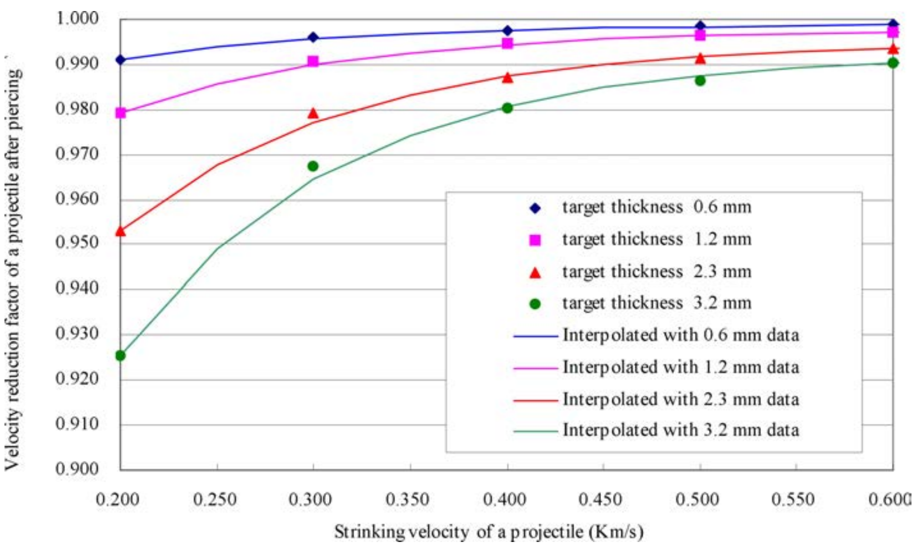

FIG. 1. Velocity reduction factors of projectile after piercing the metal plate.

Table 2. Interpolation parameters of Eq. (2.2) with various plate thicknesses.

Steel plate	Thickness: 0.6 mm	Thickness: 1.2 mm	Thickness: 2.3 mm	Thickness: 3.2 mm
a	−0.42380	−0.10103	−0.23423	−0.38021
τ	0.120482	0.117647	0.116279	0.114943
b	0.999053	0.997771	0.994868	0.992354

$$A_{\text{decel}} = \left| \frac{V^2_{\text{after piercing}} - V^2_{\text{strinking}}}{2t_{\text{sheet}}} \right| = \left| \frac{\alpha^2 - 1}{2t_{\text{sheet}}} \right| V^2_{\text{strinking}}. \tag{2.3}$$

From Eq. (2.2) and (2.3) the average deceleration of a projectile after piercing individual plate could be estimated, and the thickness distribution of the plate for overall uniform deceleration could be designed. Figures 2a and 2b show the distribution of 60 plate arrays and the estimated deceleration of a projectile with the range of constant deceleration of about 100 000 G.

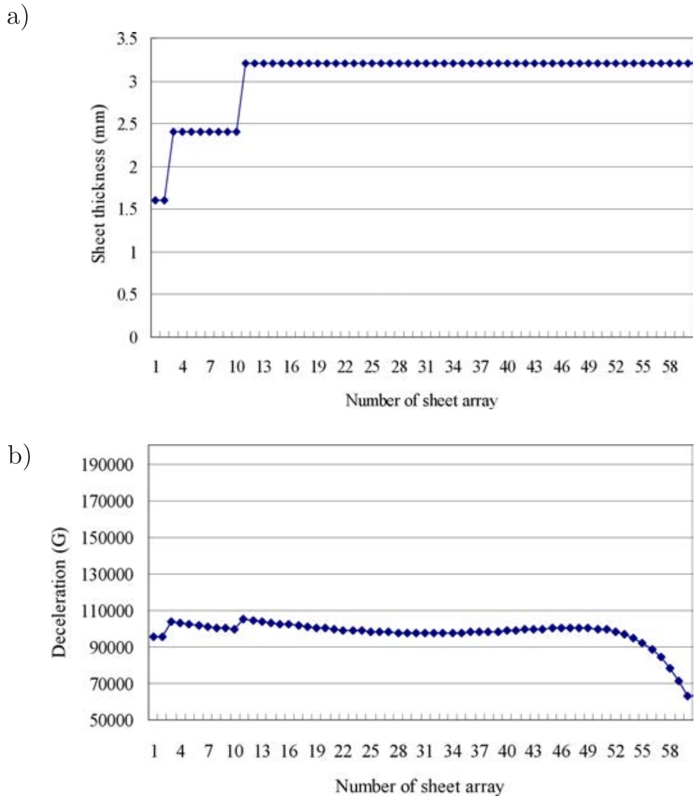

FIG. 2. Estimation of thickness distribution of plate array for soft recovery of projectile: a) thickness distribution of sheet array, b) estimated deceleration of a projectile.

3. Field tests

A soft recovery system was designed and fabricated. It consists of three identical steel frames bolted together to have an overall length of 12 m, Fig. 3. The dimensions of the frame are 900 mm × 900 mm × 4000 mm and the frame is made of 100 mm × 100 mm steel square tube. Each frame can house 19 equally spaced steel square plates of 600 mm × 600 mm which is held by steel clamps at four corners. The steel plates of three different gauges: 0.6 mm, 1.2 mm, and 2.3 mm were tested.

Fig. 3. Soft recovery system with plates installed.

An aluminum foil sensor is glued onto every plate to measure the arrival time of the projectile onto each plate. Dedicated multi-channel time recording system, to conduct this assessment, was developed in-house. The arrival time of the projectile onto each plate was captured successfully and an overall deceleration curve was obtained from the data.

Fig. 4. Velocity measuring equipment (front and rear).

For the field test 180 mm long, a 40 mm caliber hardened steel projectile weighting 1 kg was used and two different guns were used: 40 mm rifled barrel gun and 155 mm smooth bore gun with sabot. The amount of the propellant for each shot was carefully controlled to achieve muzzle velocity of 600 m/s. The sabot assembly launched by 155 mm gun was stopped by the stopper plate while the projectile continued to fly to pierce through steel plates.

After the shot, all the plates were removed, measured, and photographed. The trajectories of the projectile can be reconstructed from postmortem analysis of the plates. The high speed video system was used to record a detailed behavior of the projectile piercing through the plates.

FIG. 5. 40 mm rifled gun.

FIG. 6. 155 mm smooth bore gun.

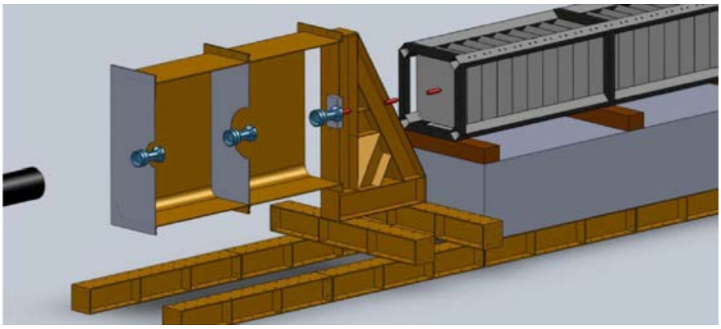

FIG. 7. Schematic of projectile and sabot separation.

FIG. 8. Sabot assembly.

FIG. 9. Deformed plates, front section.

Fig. 10. Deformed plates, mid section.

Fig. 11. Deformed plates end section.

Fig. 12. Projectile wedged in wooden block.

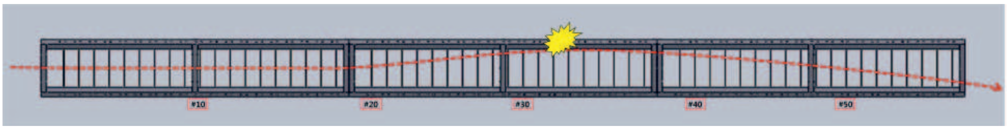

Fig. 13. Trajectory of projectile reconsructed from plates data.

4. Results and discussion

Two different guns were used for the field firing test: a rifled barrel gun and smooth bore gun. Total of eight effective shots were fired by 40 mm rifled gun and three different gauge plates were tested. Only two projectiles were retrieved but were severely deformed and fractured. The clamps holding the plates were often damaged and had to be replaced for subsequent tests. Sections of the frame were also damaged by the high speed projectile exiting out of the frame's sideway. The test results were almost identical regardless of a thickness of the plate. The projectiles veered off from the initial firing line and exited at the mid-section of the frame. Initially, the projectile was piercing through 10–15 plates with no significant yaw angle deviation occurring at two to three meters. Then, the projectile experienced a rapid deceleration caused by fast increase of yaw angle. Finally, the projectile started to tumble. The projectile was deformed and fractured by high impact forces acting from random directions. Once the axis of

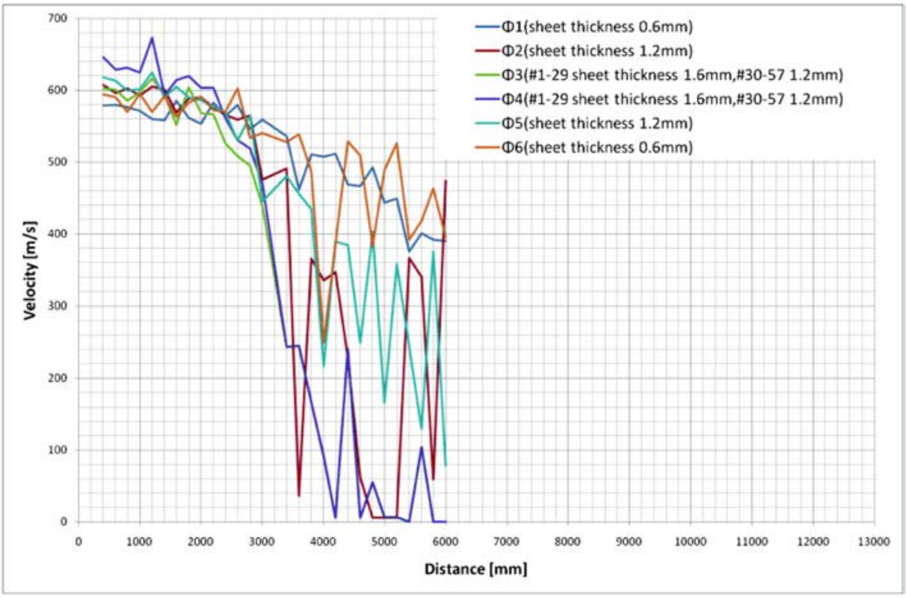

Fig. 14. Distance-velocity data using 40 mm rifled gun.

the projectile is not parallel with flying line, the directions of the stopping forces exerted from the plates are not in the axis of the projectile, i.e., axis-symmetric assumption is no longer valid. Consequently, magnitude of the stopping force increases with the yaw angle.

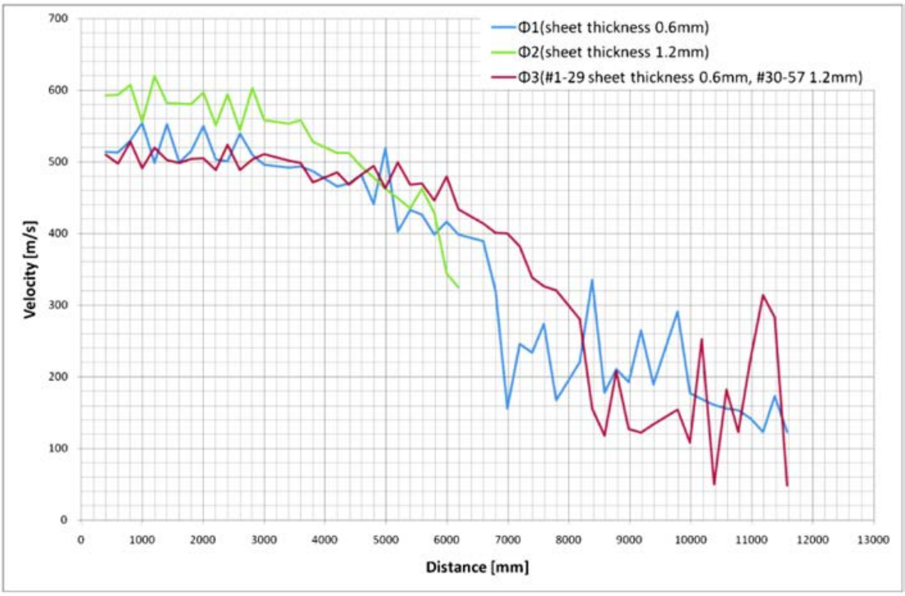

FIG. 15. Distance-velocity data using 155 mm smooth bore gun.

Next, the four effective shots were fired by 155 mm smooth bore gun with plastic sabot assembly. The sabot assembly, launched without a spin, was stopped by stopper plate while the projectile continued to fly, in the end, piercing through steel plates. A short cylinder chunk of the plastic sabot, which punched through the hole of the stopper plate, was following the projectile. This plastic chunk was piercing the larger hole in the plates made in a place where there was already a hole made by the projectile. Thus, the trajectory and posture data were destroyed. Fortunately, the high speed video was operational to record the trajectory and posture data. One projectile was found wedged into the wooden block behind the frame with a minor deformation and another one was found intact on the ground before the end of the frame. According to the high speed video the last projectile entered the test section with initial yaw about 10 degrees thus slowed down much faster and tumbled away. The initial yaw may be caused by a misalignment of the stopper plate in front of the frame. Compared with the rifled gun case, a smooth bore gun test results were more satisfactory, i.e., smooth deceleration span was much longer and projectiles were recovered intact. In the case of 0.6 mm thick plates, the projectile pierced through first

20–30 plates, in a span of four to six meters, with no significant yaw angle deviation. The average deceleration rate, about 0.3%, calculated from the test data agrees well with a numerical simulation estimation. In case of next 10–15 plates, in a span of two to three meters, the deceleration rate increased slightly with a slight increase of yaw angle. Then, the projectile speed was slow enough and the projectile experienced rapid deceleration caused by a fast increase of yaw angle. In Fig. 13 we can find the projectile trajectory reconstructed from the post-mortem analysis of the recovered plates. The projectile was piercing through the plates in a straight manner and started to veer slowly to top- left direction around a half span and changed direction to bottom- right while rubbing with metal clamps about two- thirds of the span. Finally it exited through the end of the frame, then wedged into the wooden block in the back, see Fig. 12. For 1.2 mm thickness case, the same sequence was observed but the projectile stopped in a half length of the span.

For the projectile with a zero spin and zero yaw, the deceleration characteristics can be described by three different zones: (1) smooth and steady deceleration, (2) deceleration rate increases yet remains constant, (3) sudden increase of deceleration. A perfect alignment of the projectile and the plates is the crucial condition for a successful soft- recovery test but it cannot avoid the axis force components. Comparing the results from the two different guns, it is evident that the initial spin of the projectile attributes to a faster yaw increase. The fast yaw angle increase is caused by the gyroscopic force from the interaction between the spinning projectile and the plate. The final phase of an abrupt deceleration begins at critical speed or critical yaw angle.

Even with perfect test condition, the axis symmetric assumption cannot be maintained throughout the test. Hence, further numerical studies of three-dimensional oblique impact behavior of the projectile are required. More tests with different thickness distribution of the plates and careful alignment are needed to complete the soft recovery test.

Acknowledgment

This work was supported by an ADD fundamental research grant to the Korea University of Technology and Education (UD080011GD).

References

1. Goldsmith W., *Review Non-ideal projectile impact on targets*, International Journal of Impact Engineering, **22**, 95–395, 1999.

2. Yoo Y.H., Chang S.N., Chung D.T., *Numerical Simulation of High-Velocity Oblique Impact of Mild Steel Spheres Against Mild Steel Plates*, Journal of KSME, **26**, 3, 576–585, 2002.

3. Park M.S., Yoo J.H., Chung D.-T., *An Optimization of a Multi-Layered Plate under Ballistic Impact*, International Journal of Solids and Structures, **27**, 1, 123–137, 2005.

4. Johnson G.R., Cook W.H., '*Lagrangian EPIC code computations for oblique, yawed-rod impacts into thin-plate and spaced-plate targets at various velocities*, International Journal of Impact Engineering, **14**, 373–383, 1993.

5. Meyers M.A., *Dynamics behavior of materials*, John Wiley & Sons, Inc., New York, 1994.

Received January 11, 2011; revised version August 15, 2011.

ENGINEERING TRANSACTIONS • *Engng. Trans.* • **60**, 1, 15–29, 2012
Polish Academy of Sciences • Institute of Fundamental Technological Research (IPPT PAN)
National Engineering School of Metz (ENIM)
SIXTY YEARS OF THE ENGINEERING TRANSACTIONS

Perforation Modes of Metal Plates Struck by a Blunt Rigid Projectile

Chen XIAOWEI[1)], Liang GUANJUN[2)]

[1)] *China Academy of Engineering Physics*
Institute of Structural Mechanics
P.O.Box 919-401, Mianyang, Sichuan, 621900
e-mail: chenxiaoweintu@yahoo.com

[2)] *Southwest University of Science & Technology*
School of Civil Engineering
Mianyang, Sichuan, 621010

The present paper analyzes the possible modes of shear plugging and adiabatic shear plugging in the perforation of metal plates struck by a blunt rigid projectile. The modified ballistic limit and residual velocity under the condition of adiabatic shear plugging are further formulated. Further experimental analyses are conducted on the perforations of Weldox E steel plates in order to discuss the effects of plate thickness and material strength/hardness on the terminal ballistic performance. More experimental evidence confirms the jump of residual velocity at the ballistic limit induced by the structural response of the plate. With increasing the thickness of plate and the material strength, failure modes of the plate may transform from shear plugging to adiabatic shear plugging.

Key words: blunt rigid projectile, metallic plate, perforation, shear plugging, adiabatic shear plugging.

1. Introduction

Perforation of intermediate thick metallic plates by a blunt rigid projectile has been paid much attention [1–7] for a long time because of its civil and military applications, and recent work may be referenced to Børvik *et al.* [2, 8–11], Dey *et al.* [4], Chen and Li [12–13], and Chen *et al.* [1, 14–16]. With increasing the plate thickness and impact velocity, shear plugging becomes a likely failure mode of the final perforation of an intermediate thick metallic plate.

There exist many analytical models to predict the ballistic performance, e.g. Wen and Jone [17], Bai and Johnson [18], and Ravid and Bodner [19].

Based on the conservation of momentum and energy, Recht and Ipson [20] proposed a shear plugging model to predict the residual velocity according to a given impact velocity and a ballistic limit velocity obtained from a dimensional analysis. Recht and Ipson [20] completely ignore the structural response for relatively thin plates and the local penetration for relatively thick plate. Using the energy-balance approach, Srivathsa and Ramakrishnan [21, 22] derived a ballistic performance index to estimate and compare the ballistic quality of metal materials. This index is a function of the commonly determined mechanical properties of the target material and the striking velocity of the projectile. Chen and Li [12] presented closed-form analytic solutions for ballistic perforation of ductile circular plates struck by blunt projectiles. In addition to the localized shear deformation at the peripheral of the central plug, their rigid-plastic structural model also considered the effect of plate bending and membrane stretching. The local indentation/penetration employs a dynamic cavity model. With the assistance of numerical simulation, Chen *et al.* [16] further discuss the applicability of this model and its discrepancy when compared to the experimental results and simulation.

Basically, the perforation mechanism of the ballistic performances depends on the target material property (e.g., strength or hardness), target dimensions, projectile nose shape, mass and impact velocity. By means of experiment and numerical simulation, Børvik *et al.* [2] and Dey *et al.* [3] systematically analyzed the effect of target thickness and strength on the ballistic performance. In general, the ballistic limit rises monotonically with increasing the target thickness and strength when the shear plugging dominates in the perforation of the plate. However, the perforation is always an adiabatic heat process and under the adiabatic condition, the majority of the plastic energy is converted into heat. This generates localized high temperature and adiabatic shearing occurs when the thermal softening outbalances the incremental strain and the strain-rate hardening of the target material, which eventually leads to the catastrophic failure within the Adiabatic Shear Band (ASB). With increasing the target thickness and strength, the failure mode easily transform from shear plugging to adiabatic shear plugging. ASB distinctly influences the ballistic performance, and one deduction is that the monotonic relationship between the ballistic limit and target thickness and strength never come into existence. Instead, it becomes an approximate relationship [23, 24]. With further considering the possible transforming mechanism of material failure, Chen *et al.* [1] check the initiation condition for adiabatic shear band failure and present the criterion of adiabatic shear plugging in the case of a blunt projectile perforating a metallic plate.

Based on the analytical models by Chen and Li [12] and Chen *et al.* [1], the present paper analyzes the possible modes of shear plugging and adiabatic shear plugging in the perforation of metal plates struck by a blunt rigid projectile. The modified ballistic limit and residual velocity under condition of adiabatic shear plugging are further formulated. Further experimental analyses are conducted on the perforations of Weldox E steel plates [2, 3], to discuss the effects of plate thickness and material strength/hardness on the terminal ballistic performance.

2. Shear plugging and perforation of ductile circulate plates struck by a blunt projectile

Chen and Li [12] studied the formation of shear plug during the perforation of ductile circular plates struck by a blunt projectile. In their studies, the effects of shear, plate bending, and membrane stretching were considered via a rigid-plastic analysis, while the local indentation/penetration was represented in a dynamic cavity expansion model.

Consider a blunt projectile of mass M and caliber d impacting a clamped ductile circular plate of thickness H and diameter D. The yielding stress and density of target material are σ_y and ρ respectively. Thus the dimensionless thickness and mass of target are $\chi = H/d$ and $\eta = \rho\pi d^2 H/4M$ respectively. The intermediate thick plate and plate bending are included only, i.e., membrane stretching and local indentation/penetration are ignored. It corresponds to the case of $\chi_1 < \chi \leq \sqrt{3}\,(A + B\Phi_J)/4$, in which χ_1 is the empirical upper limit of thin plate and it depends on the target material and diameter D, usually we have $\chi_1 \approx 0.2$. A and B are the dimensionless material constants used in the dynamic cavity model.

It is assumed that a central plug will be formed in front of the projectile at a critical condition when the total compressive force on the projectile nose equals to the fully plastic shear force on the peripheral of the plug. After the plug is formed, it moves with the projectile under constant shear resistance, Q_0, which is equal to $H\tau_y = H\sigma_y/\sqrt{3}$ according to the von Mises yielding criterion, where τ_y and σ_y are the shear yield stress and compressive yield stress of the material, respectively. Dimensionless mass between the central plug and projectile is denoted by $\eta = \rho\pi d^2 H/4M$. $M_0 = \sigma_y H^2/4$ and $N_0 = \sigma_y H$ are the fully-plastic bending moment and membrane force in a rigid-perfectly-plastic circular plate, respectively. With considering the plate bending, Chen and Li [12] presents the ballistic limit of plate and residual velocity of projectile are as following,

$$
\begin{aligned}
V_{BL} &= 2\sqrt{\frac{2\chi\,(1+\eta)\,(\eta+\vartheta)}{\sqrt{3}}}\cdot\sqrt{\frac{\sigma_y}{\rho}},\\
V_r &= \frac{\vartheta V_i + \eta\sqrt{\left(V_i^2 - V_{BL}^2\right)}}{(1+\eta)\,(\eta+\vartheta)} \geq V_{\mathrm{Jump}}.
\end{aligned}
\tag{2.1}
$$

Regarding the residual velocity, a jump of residual velocity

$$V_{\text{Jump}} = \frac{\vartheta V_{BL}}{(1+\eta)(\eta+\vartheta)} > 0$$

exists at the ballistic limit. ϑ in Eqs. (2.1) is a dimensionless parameter which depends on the plate thickness and diameter,

$$\vartheta = \begin{cases} \dfrac{3\left(1-\sqrt{3}\chi\right)(1+\eta)}{2\,(2\xi/d-1)\,(\xi/d+1)}, & \chi_1 < \chi < \dfrac{1}{\sqrt{3}}\left[\dfrac{(D/d)^2-1}{(D/d+1)^2+2}\right], \\ \dfrac{3\left(1-\sqrt{3}\chi\right)(1+\eta)}{(D/d-1)\,(D/d+2)}, & \dfrac{1}{\sqrt{3}}\left[\dfrac{(D/d)^2-1}{(D/d+1)^2+2}\right] \le \chi < \dfrac{1}{\sqrt{3}}. \end{cases} \tag{2.2}$$

If $1/\sqrt{3} \le \chi \le \sqrt{3}\,(A+B\Phi_J)/4$, we have $\vartheta = 0$, and in that case, Eq. $(2.1)_2$ of residual velocity is same as RECHT and IPSON [20]. ξ in Eq. (2.2) denotes the stationary location of a bending hinge during the shear sliding phase, and we have [12],

$$\frac{\xi}{d} = \begin{cases} \dfrac{\sqrt{3}\chi + \sqrt{1+2\sqrt{3}\chi - 6\chi^2}}{2\left(1-\sqrt{3}\chi\right)}, & \chi_1 < \chi < \dfrac{1}{\sqrt{3}}\left[\dfrac{(D/d)^2-1}{(D/d+1)^2+2}\right], \\ \dfrac{D}{2d}, & \dfrac{1}{\sqrt{3}}\left[\dfrac{(D/d)^2-1}{(D/d+1)^2+2}\right] \le \chi < \dfrac{1}{\sqrt{3}}. \end{cases} \tag{2.3}$$

3. TRANSITION CRITERIA FROM SHEAR PLUGGING TO ADIABATIC SHEAR PLUGGING

The target material property (e.g., strength or hardness), target thickness and impact velocity have obviously influence on the ballistic performances of a blunt projectile impacting on a metallic plate. Under the adiabatic condition, accompanied with increasing the target thickness and strength, the failure mode easily transforms from shear plugging to adiabatic shear plugging or to the hybrid of these two modes. ASB distinctly influences the ballistic performance, and CHEN *et al.* [1] further check the initiation condition for adiabatic shear band failure for the case of a blunt projectile perforating a metallic plate.

The characteristic width of a shear hinge is $e_b = \alpha H/3$, and α is an empirical coefficient,

$$\alpha = \begin{cases} 1, & V_i/c_p < 1; \\ \exp\left[C\,(1 - V_i/c_p)\right], & V_i/c_p \ge 1, \end{cases} \tag{3.1}$$

where $c_p = \sqrt{E_h/3\rho}$ is the propagating velocity of shear hinge disturbance and E_h is the linear hardening modulus which may decrease due to thermal softening. C is an empirical constant and suppose $C = 5$. More details on the discussion of the characteristic width of a shear hinge can be found in Chen *et al.* [1]. Consequently, in case of un-perforation or ballistic limit, i.e., $V_i \leq V_{BL}$, the maximum engineering shear strain and the average shear strain rate within the shear hinges around the peripheral of the striker are calculated respectively as follows [1],

$$\begin{aligned}\gamma_1 &= \frac{3\sqrt{3}}{16\alpha\chi\,(1+\eta)\,(\eta+\vartheta)} \cdot \frac{\rho V_i^2}{\sigma_y},\\ \dot{\gamma}_1 &= \frac{3}{4\alpha\,(1+\eta)} \cdot \frac{V_i}{H}.\end{aligned} \tag{3.2}$$

Whereas in case of perforation, i.e., $V_i > V_{BL}$, the maximum engineering shear strain and the average shear strain rate within the shear hinges are different,

$$\begin{aligned}\gamma_{1*} &= \frac{1.5}{\alpha},\\ \dot{\gamma}_{1*} &= \frac{2\sqrt{3}\,(\eta+\vartheta)}{\alpha\left[V_i - \sqrt{\left(V_i^2 - V_{BL}^2\right)}\right]} \cdot \frac{\sigma_y}{\rho d}.\end{aligned} \tag{3.3}$$

Taking into account the effects of temperature and strain-rate, and using the Johnson-Cook flow law, we have a simple shear constitutive equation of the following form:

$$\tau = \frac{1}{\sqrt{3}}\left[a + b\left(\frac{\gamma}{\sqrt{3}}\right)^n\right]\left[1 + c\ln\left(\frac{\dot{\gamma}}{\sqrt{3}\dot{\varepsilon}_0}\right)\right]\left[1 - \left(\frac{T-T_r}{T_m-T_r}\right)^m\right] \tag{3.4}$$

in which the von Mises equivalent stress, strain, and strain rate (i.e., $\tau = \sigma/\sqrt{3}$, $\varepsilon = \gamma/\sqrt{3}$ and $\dot{\varepsilon} = \dot{\gamma}/\sqrt{3}$) are used in the formulation. The parameters: a (or $a = \sigma_y$), b (nearly as E_h), c and n are all material constants, and $\dot{\varepsilon}_0$ is a prescribed reference strain rate. T_r and T_m are respectively the environmental reference temperature and the melting temperature of target material.

The adiabatic temperature-rise within the shear hinges may be integrated by the formula $dT = \dfrac{\beta}{\rho\, C_V}\tau\, d\gamma$ and Eq. (3.4). Simply, we have $m = 1$, and C_V is the specific heat and β is the Taylor-Quinney coefficient. Usually, the strain-rate effects are measured by its average value during the dynamic deformation. Thus, the expression for the maximum shear stress ($d\tau = 0$) criterion with constant strain-rate ($d\dot{\gamma} = 0$) is [25],

$$\frac{\partial\tau}{\partial\gamma} + \frac{\beta\tau}{\rho\, C_V} \cdot \frac{\partial\tau}{\partial T} = 0. \tag{3.5}$$

According to the definitions of maximum engineering shear strain and average shear strain rate within the shear hinges, i.e. Eqs. (3.2), (3.3). The critical velocity V_A corresponding to the initiation of adiabatic shear failure may be deducted from Eq. (3.5) [1]. Hence, we have,

$$\begin{aligned}
&\left[a + b\cdot\left(\frac{3\rho V_A^2}{16\alpha\chi\left(1+\eta\right)\left(\eta+\vartheta\right)\sigma_y}\right)^n\right]^2\left[1 + c\ln\left(\frac{\sqrt{3}V_A}{4\alpha\left(1+\eta\right)\dot{\varepsilon}_0 H}\right)\right] \\
&\qquad = \frac{nb\rho C_V\left(T_m - T_r\right)}{\beta}\cdot\left(\frac{3\rho V_A^2}{16\alpha\chi\left(1+\eta\right)\left(\eta+\vartheta\right)\sigma_y}\right)^{n-1}, \quad \text{if } V_i \le V_{BL}, \\
&\left[a + b\cdot\left(\frac{\sqrt{3}}{2\alpha}\right)^n\right]^2\left[1 + c\ln\left(\frac{2\left(\eta+\vartheta\right)}{\alpha\left[V_A - \sqrt{\left(V_A^2 - V_{BL}^2\right)}\right]\dot{\varepsilon}_0}\right)\right] \\
&\qquad = \frac{nb\rho C_V\left(T_m - T_r\right)}{\beta}\cdot\left(\frac{\sqrt{3}}{2\alpha}\right)^{n-1}, \quad \text{if } V_i > V_{BL}.
\end{aligned} \tag{3.6}$$

Actually, Eqs. (3.6) are the explicit relations among the critical velocities corresponding to adiabatic shear failure, target thickness, target parameters (material hardness, density and mechanics etc.) and projectile parameters (geometry, mass).

4. Adiabatic shear plugging of ductile circulate plates struck by a blunt projectile

Once the initiation condition for adiabatic shear band failure is achieved for the case of a blunt projectile perforating a metallic plate, the adiabatic temperature-rise within the shear hinges will cause the material thermal softening in the local zone, and thus the material failure of the target will be reached much more easily, as it requires less energy compared to shear failure. It is reasonable that the failure mode of blunt projectile perforating a metallic plate will transform from shear plugging to adiabatic shear plugging. Therein the perforation includes two possible failure modes, i.e, shear plugging and adiabatic shear plugging. The ballistic performance of the first mode can be completely depicted by Sec. 2. Regarding the second mode, i.e., adiabatic shear plugging, the perforation scenarios are much more complicated and respectively need to be analyzed.

1. $V_A \le V_{BL}$

Adiabatic shear plugging occurs prior to the shear plugging, and it is concluded that the perforation mode is the first one. Thus, the ballistic limit is modified as

$$V_{ASB-BL} = V_A. \tag{4.1}$$

Chen *et al.* [1] indicated that this scenario corresponds to a thicker plate and the structural response of the plate is ignored. Under higher impact velocity than the ballistic limit, the residual velocity of both projectile and plug is

$$V_r = \sqrt{\left(V_i^2 - V_{ASB-BL}^2\right)} \Big/ (1+\eta). \tag{4.2}$$

2. $V_A > V_{BL}$

Chen *et al.* [1] indicated that this scenario corresponds to a thinner plate and the structural response of the plate should be taken into account.

In the case of an un-perforation or in the ballistic limit, i.e., $V_i \leq V_{BL} < V_A$, no adiabatic shear plugging occurs.

If $V_{BL} < V_i < V_A$, the projectile perforates the plate as shear plugging and no adiabatic shear failure occurs. Therein its ballistic performance is formulated by Eq. (2.1) of Sec. 2.

If $V_i \geq V_A$, the projectile perforates the plate as adiabatic shear plugging. Since the failure mode is transformed, the residual velocity of Eq. $(2.1)_2$ is modified to

$$V_r = \frac{\vartheta V_i + \eta\sqrt{\left(V_i^2 - V_{ASB-BL}^2\right)}}{(1+\eta)(\eta+\vartheta)} \tag{4.3}$$

and we suppose $V_{ASB-BL} = V_A$ here.

Furthermore, during the transformation from shear plugging to adiabatic shear plugging, the material failure mode in the shear hinge is not absolutely singleness. The experimental results indicate that it should be a hybrid of shear failure and adiabatic shear failure. More generally, we suppose that the ballistic limit of the adiabatic shear plugging has the following relationship,

$$V_{ASB-BL} = (1-\delta)\cdot V_A + \delta \cdot V_{BL}, \qquad \text{where} \quad 0 < \delta \leq 1, \tag{4.4}$$

where the value of δ depends on which one dominates in the target material failure. If $\delta = 0.5$, we have $V_{ASB-BL} = (V_A + V_{BL})/2$. Employing Eq. (4.4) into this section, the modified ballistic performance of blunt projectile perforating metallic plate as adiabatic shear plugging is obtained.

5. Experimental analyses

Chen and Li [12] first theoretically explained some special phenomenon, such as, that the residual velocity will behave as a jump near the ballistic limit in the case of perforation of a thin metallic plate and the ballistic limit abnormally descend with increasing the target thickness regarding a range of plate thicknesses. The present paper further analyzes the experimental data of Børvik *et al.* [2] and Dey *et al.* [3] and again confirm these special phenomenon. Also we will discuss the applicability of Chen and Li [12], Chen et al. [1] and the present modified model with changing the target thickness and strength.

The present analytical model assumes that the projectile and plug have the same residual velocity after perforation. In order to compare the analytical results with experimental data, a nominal residual velocity in a test is defined based on the conservation of momentum

$$V_r = \frac{M \cdot V_{pr} + M_{pl} \cdot V_{plr}}{(M + M_{pl})}, \tag{5.1}$$

where, in a test, V_{pr} and V_{plr} are the residual velocities of the projectile and the target plug respectively. The mass of target plug is $M_{pl} = \pi \rho d^2 H/4$.

The target material in Børvik *et al.* [2] is Weldox460E and the corresponding material properties can be found in that reference. Dey *et al.* [3] employed three steel alloys of Weldox460E, Weldox700E and Weldox900E, which have different yielding strength, i.e., 499 MPa, 859 MPa and 992 MPa, respectively. The blunt projectile is made of high strength steel of Arne with $\sigma_y = 1900$ MPa. Its mass is 0.197 kg, and its diameter and length are 20 mm and 80 mm respectively.

5.1. *Effect of target thickness on the ballistic performance*

Børvik *et al.* [2] published a large amount of experimental results on the ballistic performance of ductile plates struck by blunt projectiles, as seen in Fig. 1. Their plate thicknesses ranged from thin to intermediate, i.e., target thickness are $H = 6$ mm, 8 mm, 10 mm, 12 mm, 16 mm, and 20 mm respectively. The corresponding dimensionless thickness are $\chi = 0.3$, 0.4, 0.5, 0.6, 0.8, and 1.0, respectively.

The experimental results of Børvik *et al.* [2] showed that regarding relatively thin plates, i.e., $\chi = 0.3$, 0.4 and 0.5, due to the bending response of plate, a jump of residual velocity occurs at the ballistic limit and its value decreases with raising the target thickness; whereas regarding the thick targets ($\chi = 0.6$, 0.8 and 1.0), the curves of residual velocity vary continuously. Figure 1 demonstrates the comparison between experimental data and theoretical predictions by Chen and Li [12], and it clearly shows validation of Chen and Li's [12] model. The experimental data are the weighted average values of the residual velocities of projectile and plug.

Figure 2 shows the effect of target thickness ($\chi = H/d$) of Weldox 460E on the ballistic limit. The test data of Børvik *et al.* [2] showed that regarding

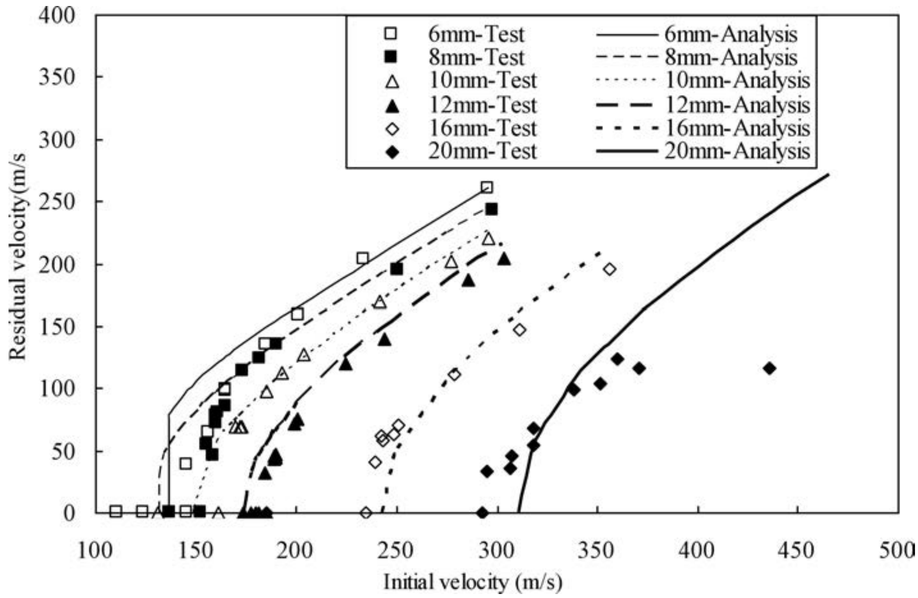

Fig. 1. Comparison between the prediction from Chen and Li [12] and the test data of ballistic performances [2].

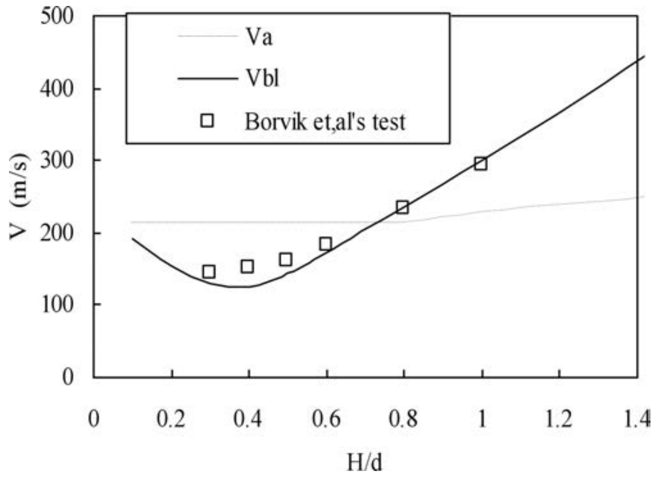

Fig. 2. Variations of critical velocities for the ballistic limit (V_{BL}) and initiation of adiabatic shear (V_A) against plate thickness (H/d).

the thin plates, the ballistic limit rises very slowly with increasing the target thickness; differently, it rises linearly and distinctly regarding the thick plates. Further popularly, Chen and Li [12] indicate in a range of target thickness that it is due to the structural response of thin plate that results in the abnormal descending of ballistic limit with increasing target thickness.

Figure 2 simultaneously presents the prediction of the critical velocity of adiabatic shear failure with varying thickness. Børvik *et al.* [2, 8, 9] also analyzed the different failure modes of the perforation of plates with different thickness. It demonstrates that with increasing the target thickness, the deformation of plate transforms from structural response of thin plate and local shear plugging to adiabatic shear failure. The adiabatic shear failure behaves as a deformed ASB and a transformed ASB respectively.

It is emphasized that the two theoretical curves in Fig. 2 intersect at $\chi = 0.7$. This indicates that, in the case of $\chi < 0.7$, as $V_A > V_{BL}$, even if the impact velocity is greater than the ballistic limit, the target failure may be still shear plugging. The adiabatic shear failure does not easily occur, and it requires a higher impact velocity, i.e., $V_i > V_A$. In case of $\chi > 0.7$, as $V_A < V_{BL}$, adiabatic shear failure may appear easily, even if impact at lower velocity and no perforation. In particular, the ballistic limit should be modified based on Eq. (4.4) because of the hybrid of failure modes. In Fig. 2, the test data locate much close to the prediction of shear plugging, and it indicates the shear plugging dominates in the perforation rather than adiabatic shear failure. Therein suggest $\delta = 0.9$ in Eq. (4.4) regarding Børvik *et al.* [2] test.

Chen *et al.* [1] discussed in detail the variation of adiabatic temperature-rise, strain and strain rate against the target thickness and impact velocity in a local shear zone, which agrees well with the experimental results and numerical simulation. Here, this is not repeated.

Regarding the thin plates, the prediction of the ballistic limit and jump of residual velocity in Fig. 1 is somehow discrepant from the test data. Chen and Li [12] also presented a thinner plate model with considering the membrane effect, and demonstrated that the test data is located between the predictions of thinner and medium plates. However, regarding the thicker plates, e.g., $\chi = 1.0$, the discrepancy of residual velocity between the prediction and test of residual velocity is due to the assumption of rigid projectile. In that case, the projectile deforms and blunts more seriously and much more impact energy is devoted to the plastic deformation of projectile. The projectile even breaks when it perforates much thicker plates, e.g., $\chi = 1.25$ or $\chi = 1.5$. Therein, the model of Chen and Li [12] has its specific applicability for target thickness.

5.2. Effect of target strength or hardness on the ballistic performance

There are limited experimental data to show the affect of material strength on the ballistic performance of a small thickness target (or plate). Sangoy *et al.* [23] demonstrated that there are three zones in the hardness-ballistic limit relationships, i.e., (1) low hardness regime, where perforation resistance increases with hardness, (2) medium hardness regime, where the ballistic limit decreases due to the onset of adiabatic shear damage, and (3) high hardness regime, where perforation resistance increases again due to the projectile break-up. It means that ASB distinctly influences the ballistic performance. In an engineering perspective, it is usually assumed that the hardness is proportional to the material yielding strength; and thus, the monotonic relationship between the ballistic limit and target thickness and strength never come into existence. Instead it converts into an approximate relationship [23, 24], i.e., the variation of the ballistic limit may have a phenomenon of an "up-down-up" trend with an increase in the target thickness and strength.

Dey *et al.* [3] conducted a large amount of perforation tests on the steel alloy plates of Weldox 460E, Weldox 700E, and Weldox 900E respectively with thickness $H = 12$ mm, and analyzed the effect of target strength or hardness on the ballistic performance. The main discrepancy of the three steel alloys is that they have different yielding strength, i.e., 499 MPa, 859 MPa, and 992 MPa respectively. Thus, in this analysis we assume that the other parameters of Weldox 700E and Weldox 900E are same as those of Weldox 460E.

A Johnson-Cook material model is employed in Chen *et al.* [1] to discuss the influence of adiabatic shear failure, and the effect of target material strength is demonstrated as well. Figure 3 shows the critical velocity at initiation of adiabatic shear failure and the variation of the ballistic limit against the target material yielding a strength as predicted by Chen and Li [12], as well as the experimental results of ballistic limit. According to the model of shear plugging, the theoretical ballistic limit V_{BL} increases monotonously with the yielding stress (hardness) of plate material. On the other hand, according to the model of adiabatic shear plugging, the critical velocity V_A at adiabatic shear failure increases more gently with the yielding stress in the lower range of σ_y, and then gently

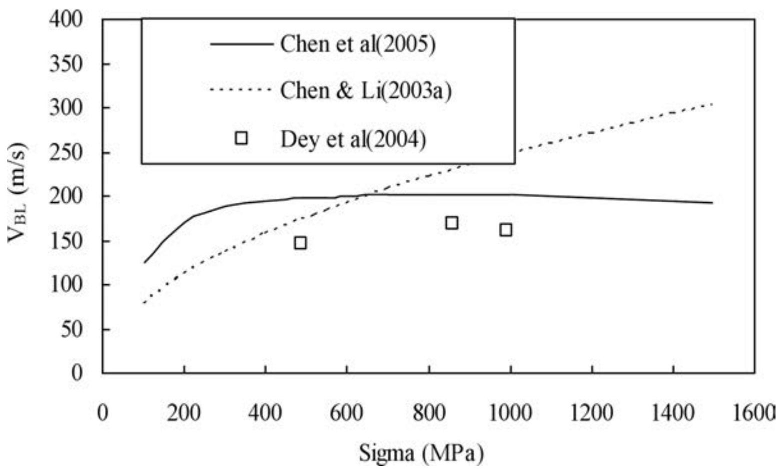

Fig. 3. Affect of plate strength on ballistic performance for $\chi = H/d = 0.6$.

decreases. Particularly in thinner plates, this phenomenon of up-and-down trend against σ_y seems more remarkable. It concludes that Chen *et al.* [1] may also have predicted the first two zones defined by Sangoy *et al.* [23]. In the present study, the projectile is assumed non-deformable, and thus, Fig. 3 demonstrates the performance in the low- to medium-hardness regime only, but fails to predict the phenomenon in the high-hardness regime.

Figures 4–6 show the test data of residual velocity of Weldox 460E, Weldox 700E, and Weldox 900E plates and the corresponding theoretical predictions by

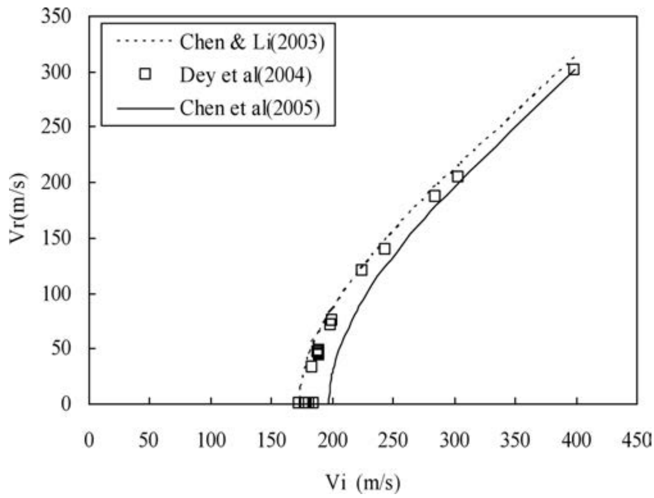

Fig. 4. Prediction of residual velocity and test data (Weldox 460E).

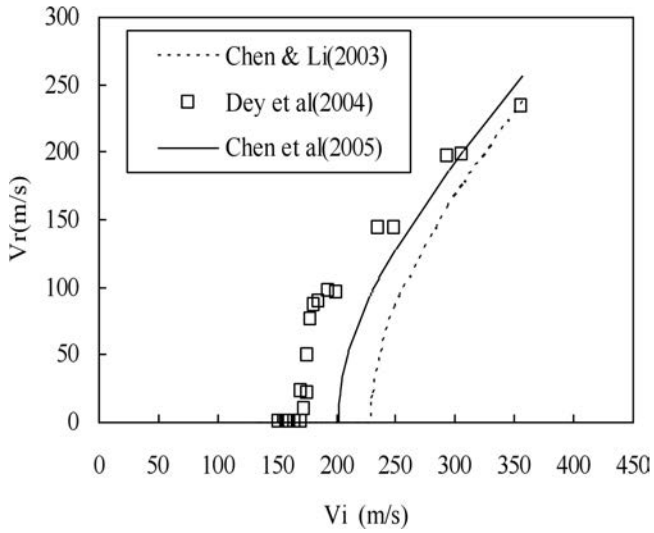

Fig. 5. Prediction of residual velocity and test data (Weldox 700E).

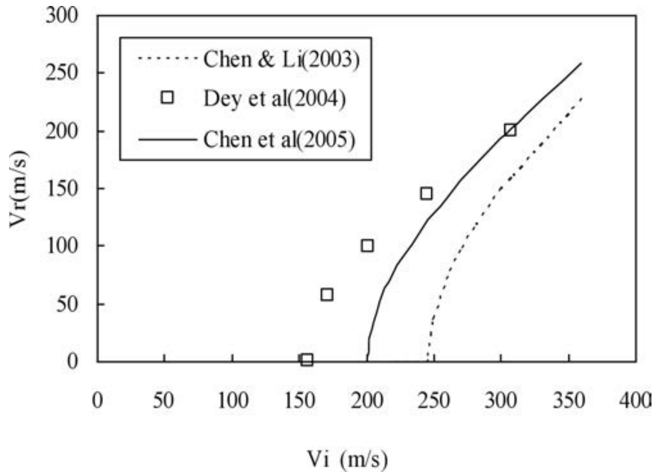

Fig. 6. Prediction of residual velocity and test data (Weldox 900E).

Chen and Li [12] and Chen *et al.* [1]. Obviously, for Weldox 460E, the test data of a lower impact velocity fits Chen and Li [12] well and implies that the dominating failure mode of the plate is shear plugging; whilst the data of a higher impact velocity locate between two models and thus shear plugging and adiabatic shear plugging both play an important role in plate perforation. Regarding Weldox 700E and Weldox 900E, all of the test data are close to Chen *et al.* [1] and the dominating failure mode of plate is adiabatic shear plugging.

The similar transition of perforation mode is also found in the sharp projectile striking Weldox 460E, Weldox 700E, and Weldox 900E plates [3]. In general, accompanied by an increase of target strength and thickness, the assumption of a rigid projectile trends to violated, and the perforation model tends toward transformation. It should be emphasized that any theoretical model has its specific applicable range.

6. Conclusions

Based on the analytical models by Chen and Li [12] and Chen *et al.* [1], the present paper analyzes the possible modes of shear plugging and adiabatic shear plugging in the perforation of metal plates struck by a blunt rigid projectile. The modified ballistic limit and residual velocity under the condition of adiabatic shear plugging are further formulated. Further experimental analyses were conducted on the perforations of Weldox E steel plates [2, 3], to discuss the affect of plate thickness and material strength/hardness on the terminal ballistic performance. More experimental evidence confirms the jump of residual velocity at ballistic limit induced by the structural response of plate. With increasing plate thickness and material strength, failure modes of plate may transform from shear plugging to adiabatic shear plugging. Due to adiabatic shear plugging, the monotonic relationship between the ballistic limit and target thickness and strength never come into existence.

References

1. Chen X.W., Li Q.M., Fan S.C., *Initiation of adiabatic shear failure in a clamped circular plate struck by a blunt projectile*, Int. J. Impact Eng., **31**, 7, 877–893, 2005.
2. Børvik T., Hopperstad O.S., Langseth M., Malo K.A., *Effect of target thickness in blunt projectile penetration of Weldox 460E steel plates*, Int. J. Impact Eng., **28**, 4, 413–464, 2003.
3. Dey S., Børvik T., Hopperstad O.S., Leinum J.R., Langseth M., *The effect of target strength on the perforation of steel plates using three different projectile nose shapes*, Int. J. Impact Eng., **30**, 1005–1038, 2004.
4. Backman M.E., Goldsmith W., *Mechanics of penetration of projectiles into targets*, Int. J. Impact Eng., **16**, 1–99, 1978.
5. Anderson Jr. C.E., Bodner S.R., *Ballistic impact: the status of analytical and numerical modeling*, Int. J. Impact Eng., **7**, 9–35, 1988.
6. Corbett G.G., Reid S.R., Johnson W., *Impact loading of plates and shells by free-flying projectiles: a review*, Int. J. Impact Eng., **18**, 141–230, 1996.
7. BenDor G., Dubinsky A., Elperin T., *Ballistic impact: recent advances in analytical modeling of plate penetration dynamics-a review*, ASME Applied Mechanics Reviews, **58**, 11, 355–371, 2005.
8. Børvik T., Langseth M., Hopperstad O.S., Malo K.A., *Ballistic penetration of steel plates*, Int. J. Impact Eng., **22**, 855–886, 1999.
9. Børvik T., Leinum J.R., Solberg J.K., Hopperstad O.S., Langseth M., *Observations on shear plug formation in Weldox 460E steel plates impacted by blunt-nosed projectiles*, Int. J. Impact Eng., **25**, 553–572, 2001.
10. Børvik T., Langseth M., Hopperstad O.S., Malo K.A., *Perforation of 12 mm thick steel plates by 20 mm diameter projectiles with blunt, hemispherical and conical noses, Part I: Experimental study*, Int. J. Impact Eng., **27**, 1, 19–35, 2002.
11. Børvik T., Hopperstad O.S., Berstad T., Langseth M., *Perforation of 12 mm thick steel plates by 20 mm diameter projectiles with blunt, hemispherical and conical noses, Part II: Numerical simulations*, Int. J. Impact Eng., **27**, 1, 37–64, 2002.
12. Chen X.W., Li Q.M., *Shear plugging and perforation of ductile circular plates struck by a blunt projectile*, Int. J. Impact Eng., **28**, 5, 513–536, 2003.
13. Chen X.W., Li Q.M., *Perforation of a thick plate by rigid projectiles*, Int. J. Impact Eng., **28**, 7, 743–759, 2003.
14. Chen X.W., Li Q.M., Fan S.C., *Oblique perforation of thick metallic plates by rigid projectiles*, ACTA Mechanic Sinica, **22**, 367–376, 2006.

15. Chen X.W., Yang Y.B., Lu Z.H., Chen Y.Z., *Perforation of Metallic Plates Struck by a Blunt Projectile with a Soft Nose*, Int. J. Impact. Eng., **35**, 6, 549–558, 2008.

16. Chen X.W., Zhou X.Q., Li X.L., *On Perforation of Ductile Metallic Plates by Blunt Rigid Projectile*, European Mechanics/A, **28**, 2, 273–283, 2009.

17. Wen H.M., Jones N., *Low-velocity perforation of punch-impact-loaded metal plates*, J. Pressure Vessel Technol., **118**, 2, 181–7, 1996.

18. Bai Y.L., Johnson W., *Plugging: physical understanding and energy absorption*, Metals Technol., **9**, 182–90, 1982.

19. Ravid M., Bodner S.R., *Dynamic perforation of viscoplastic plates by rigid projectiles*, Int. J. Impact Eng., **21**, 6, 577–91, 1983.

20. Recht R.F., Ipson T.W., *Ballistic perforation dynamics*, J. Appl. Mech., **30**, 385–91, 1963.

21. Srivathsa B., Ramakrishnan N., *On the Ballistic Performance of Metallic Materials*, Bull. Mater. Sci., **20**, 1, 111–23, 1997.

22. Srivathsa B., Ramakrishnan N., *A ballistic performance index for thick metallic armour*, Comput. Model Simul. Eng., **3**, 1, 33–39, 1998.

23. Sangoy L., Meunier Y., Pont G., *Steels for ballistic protection*, Israel J. Tech., **24**, 319–26, 1988.

24. Li Q.M., Chen X.W., *Penetration and Perforation into Metallic Targets by a Non-deformable Projectile*, Chapter 10, pp. 173–192, Engineering Plasticity and Impact Dynamics (Edt. Zhang LZ), World Scientific Publishing, 2001.

25. Bai Y.L., Dodd B., *Adiabatic shear localization: occurrence, theories and application*, UK: Pergamon Press, 1992.

Received January 11, 2011; revised version August 2, 2011.

ENGINEERING TRANSACTIONS • *Engng. Trans.* • **60**, 1, 31–39, 2012
Polish Academy of Sciences • Institute of Fundamental Technological Research (IPPT PAN)
National Engineering School of Metz (ENIM)
SIXTY YEARS OF THE ENGINEERING TRANSACTIONS

Analysis of the Cutting Parameters Influence During Machining Aluminium Alloy A2024-T351 with Uncoated Carbide Inserts

Badis HADDAG[1)], Samir ATLATI[1),2)], Mohammed NOUARI[1)],
Claude BARLIER[1)], Mohammed ZENASNI[2)]

[1)] *LEMTA CNRS-UMR 7563 – InSIC*
Laboratory of Energetics and Theoretical and Applied Mechanics
27 rue d'Hellieule, 88100 St-Dié-des-Vosges, France
e-mail: badis.haddag@insic.fr

[2)] *EMCS-ENSAO, Mohamed I University*
Team of Mechanics and Scientific Calculations
Oujda, Maroco

This work aims to analyze the effect of the cutting parameters on chip segmentation of the aluminium alloy A2024-T351 during machining process. In this work, two parameters are considered: the tool rake angle of the cutting tool and the feed under dry machining. An orthogonal cutting FE model is developed in Abaqus/Explicit for this purpose. A thermo-visco-plastic-damage model for the machined material and thermo-rigid behaviour for the cutting tool have been assumed. At the chip/tool contact zone, the modified Coulomb friction model has been adopted. Thermal effects are considered by taking into account the heat flux generated by visco-plastic strain and also by friction at the tool-workpiece interface. The obtained results showed the effect of the tool rake angle and feed on the cutting force and chip morphology as well as temperature distribution at the tool rake face.

Key words: orthogonal cutting, tool rake angle, feed, FE analysis, cutting force, chip segmentation.

1. Introduction

Machining processes are widely used in industry to produce parts with complex shapes. An accurate modelling of cutting operations requires consideration of several interacting factors and remains a challenge in industry. Behaviour and numerical aspects should be well considered to obtain accurate results which can be exploited later in an optimisation procedure. To generate a chip in machining, particularly segmented chip, modelling should include a suitable behaviour law for the workpiece and cutting tool, taking into account work-hardening, strain-rate and temperature effects [2], and adequate contact behaviour at the workpiece-tool interface. A thermo-mechanical coupling should be considered, like the evolution of the heat generated by inelastic strain in the workpiece material and by friction between the chip and tool [3].

To analyse the chip formation process in machining several studies have been carried out following the analytical approach (e.g., [7, 8]). With the development of numerical methods and computation codes simulation of more realistic machining case became possible. The Finite Element (FE) method is widely used for this purpose [3]. Recently, the Smoothed Particle Hydrodynamics (SPH) method has been also applied to analyse cutting processes [4]. In the present paper, an orthogonal cutting operation has been analysed by FE simulations, using Abaqus/Explicit software [1], to analyse both the tool rake angle and feed rate effects on the cutting force, chip morphology as well as temperature distribution at the tool rake face during machining aluminium alloy A2024-T351 with uncoated carbide inserts.

2. Modelling considerations

Since the machining involves intense thermo-mechanical phenomena, each material point in the cutting tool and the workpiece should satisfy simultaneously two equilibrium equations:

$$\mathrm{div}\sigma + f_v = \rho\ddot{u} \qquad \text{and} \qquad k\nabla^2 T - \rho c_p \dot{T} + \dot{q} = 0, \tag{2.1}$$

where σ is the Cauchy stress tensor, f_v is the body forces, $\ddot{u}$ is the acceleration, T is the temperature, ρ is the material density, k is the thermal conductivity, c_p is the thermal capacity, and $\dot{q}$ is the heat source. These equations are strongly nonlinear and coupled, since the stress σ depends on the temperature T via the material behaviour law, as it can be seen in the relationships (2.2)–(2.3). Also, a part of the mechanical inelastic work is to transform to heat, so a part of the heat flux $\dot{q}$ is a function of the flow stress and plastic strain (see Eq. (2.5)). Moreover, in the contact zone a part of $\dot{q}$ is generated by the friction process (see Eq. (2.7)). The heat flux can then be written as $\dot{q} = \dot{q}_p + \dot{q}_f$, where $\dot{q}_p$ and $\dot{q}_f$ are the heat fluxes due to inelastic and friction work, respectively.

2.1. Constitutive model

To represent the behaviour of the workpiece material during machining a Johnson-Cook visco-plastic-damage model has been adopted. The flow stress is given by the following constitutive equation:

$$\overline{\sigma} = \left[A + B(\overline{\varepsilon}^p)^n\right]\left[1 + C\ln(\dot{\overline{\varepsilon}}^p/\dot{\overline{\varepsilon}}_0)\right]\left[1 - ((T - T_0)/(T_m - T_0))^m\right], \tag{2.2}$$

where A, B, C, m, and n are the material parameters, $\overline{\varepsilon}^p$ is the Von Mises equivalent plastic strain, $\dot{\overline{\varepsilon}}^p$ is the strain rate, $\dot{\overline{\varepsilon}}_0$ is the reference equivalent plastic strain rate, T_m and T_0 are, respectively, the material melting and reference ambient temperatures. The fracture behaviour is described by a damage initiation criterion and a damage evolution law up to fracture. The damage initiation criterion is given by:

$$\begin{aligned} &\omega_d = \int \frac{d\overline{\varepsilon}^p}{\overline{\varepsilon}^p_d} \qquad \text{with} \qquad 0 \le \omega_d \le 1 \qquad \text{and} \\ &\overline{\varepsilon}^p_d = [d_1 + d_2 \exp(d_3 P/\overline{\sigma})] \left[1 + d_4 \ln \dot{\overline{\varepsilon}}^*\right] [1 - d_5 T^*] , \end{aligned} \tag{2.3}$$

where $\overline{\varepsilon}^p_d$ is the equivalent strain at the onset of damage, function of the stress triaxiality, plastic strain rate, and temperature, while $d_1, ..., d_5$ are the material damage parameters. The criterion for damage initiation is met when $\omega_d = 1$. The true stress evolution after damage initiation ($\omega_d = 1$) and the damage evolution are given by:

$$\widetilde{\sigma} = (1 - d)\overline{\sigma} \qquad \text{with} \qquad d = \overline{u}^p/\overline{u}_f = L\overline{\varepsilon}^p/\overline{u}_f, \tag{2.4}$$

where $\overline{u}^p$ is the equivalent plastic displacement and $\overline{u}_f$ is the equivalent plastic displacement at failure, which is a function of the equivalent plastic strain $\overline{\varepsilon}^p$ and the characteristic length L of the corresponding finite element. This law is introduced to avoid the mesh dependency during damage at the FE scale [1].

As the mechanical behaviour is affected by temperature, the mechanical plastic work generates a heat flux, which results in a temperature rise. The heat flux due to this phenomenon is described by:

$$\dot{q}_p = \eta_p \sigma : \dot{\varepsilon}_p, \tag{2.5}$$

where η_p is the plastic work conversion factor, generally taken equal to 0.9 for metals.

2.2. Tool-workpiece interface behaviour

The contact behaviour at the tool-workpiece interface is defined by the relationship between the normal friction stress σ_n and the shear friction stress τ_f:

$$\tau_f = \min(\mu\sigma_n, \tau_{\max}), \tag{2.6}$$

where μ is the friction coefficient and $\tau_{\max}$ is the shear stress limit considered generally equal to the initial plastic flow shear stress. The friction heat flux at the contact interface is given by:

$$\dot{q}_f = f_f \eta_f \tau_f \dot{\gamma}, \tag{2.7}$$

where $\dot{\gamma}$ is the sliding velocity, τ_f is the friction stress (Eq. (2.6)), η_f is the frictional work conversion factor (η_f is assumed as equal 1), and f_f is the fraction of the thermal energy conducted into the chip. The value of f_f depends on the thermal properties of the cutting tool and workpiece materials, as well as the temperature gradient near the chip-tool interface [3] (f_f is assumed as equal 0.9).

3. Problem description

The problem of the orthogonal cutting test is simulated, with the cutting conditions given Table 1. The corresponding experimental tests are taken from [5]. The experimental setup used to perform the tests is shown in Fig. 1.

Table 1. Cutting conditions: variation of feed and tool rake angle.

Cutting speed V_C [m/min]	Width of cut w [mm]	Feed f [mm]	Tool rake angle α [°]
60	4	0.05, 0.1, 0.3	0, 15, 30

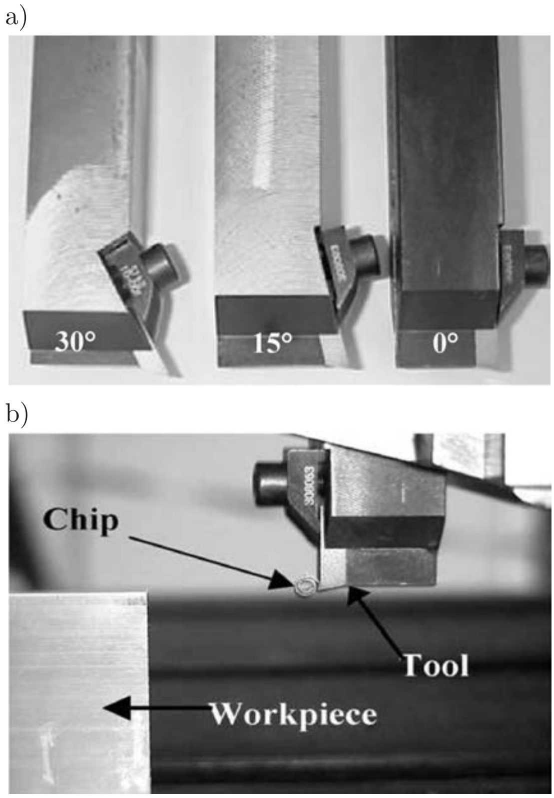

Fig. 1. Experimental setup used for the numerical analysis [5]: a) tool geometry with different tool rake angles, b) orthogonal cutting device.

Geometrical characteristics of the cutting tool and workpiece are given in Fig. 2. Basic physical properties of the workpiece and tool materials are given in Table 2 and behaviour parameters of the workpiece material are given in Table 3.

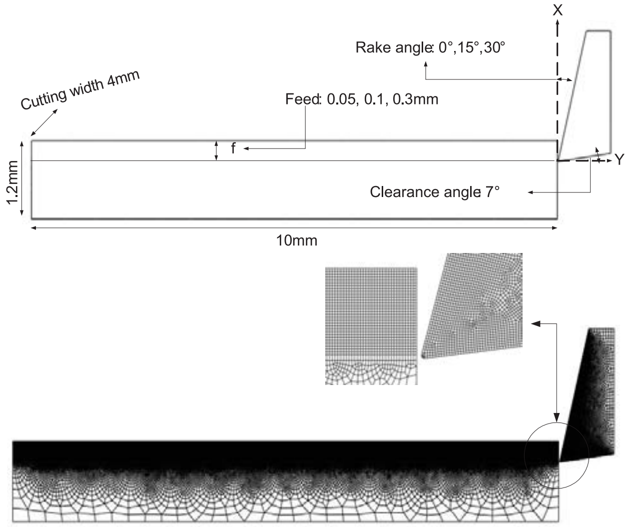

FIG. 2. Geometrical characteristics and mesh of the model.

Table 2. Basic thermo-mechanical properties of the machined workpiece and cutting tool [6].

Physical parameter	Workpiece (A2024-T351)	Tool (WC)
Density, ρ [kg/m^3]	2700	11900
Elastic modulus, E [GPa]	73	534
Poisson's ratio, ν	0.33	0.22
Specific heat, Cp [J/kg/°C]	$Cp = 0.557T + 877.6$	400
Thermal conductivity, λ [W/m/C]	$25 \leq T \leq 300 : \lambda = 0.247T + 114.4$ $300 \leq T \leq Tm : \lambda = 0.125T + 226$	50
Thermal expansion, α [µm·m/°C]	$\alpha = 8.9 \times 10^{-3}T + 22.2$	×
T_m [°C]	520	×
T_0 [°C]	25	25

Table 3. Johnson-Cook parameters of the machined workpiece [6].

Visco-plastic parameters					Damage parameters					
A [MPa]	B [MPa]	n	C	m	$d1$	$d2$	$d3$	$d4$	$d5$	$\overline{u}_f$ [mm]
352	440	0.42	0.0083	1	0.13	0.13	1.5	0.011	0	0.02

4. Results and analysis

4.1. Chip morphology

Several numerical simulations have been performed; some of them are illustrated by Fig. 3. The comparison between the numerical and experimental results shows the direct influence of the cutting parameters on the chip morphology and the temperature distribution at the tool-chip interface. From simulations, the chip thickness and its curvature are dependent on the feed rate as well as on the tool rake angle. This point has been confirmed by experiments. For small feeds ($f = 0.05$ and 0.1 mm), the simulation confirmed the continuous shape of chips, while for large feeds ($f = 0.3$ mm), the chip segmentation is well produced compared to experimental tests. Segmentation intensity is more pronounced for high feeds and small rake angles. The segmentation process is due to the strain localisation in adiabatic shear bands where the thermal softening dominates inducing a decrease of the yield stress inside the bands.

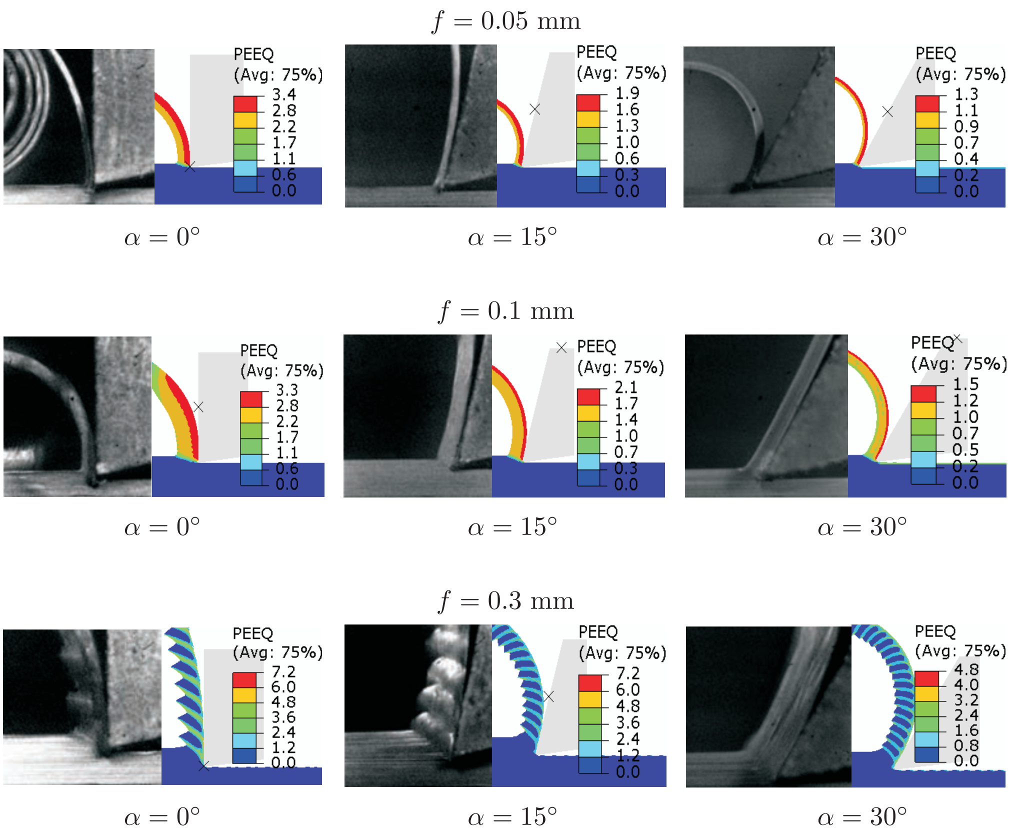

FIG. 3. Comparison between the morphology of the experimental and numerical chips.

4.2. Compression ratio and cutting forces

Variation of the cutting forces with the feed and tool rake angle at a constant cutting velocity is summarized in Fig. 4a. One can observe an increase in the cutting force vs. the feed rate and a decrease vs. the tool-rake angle.

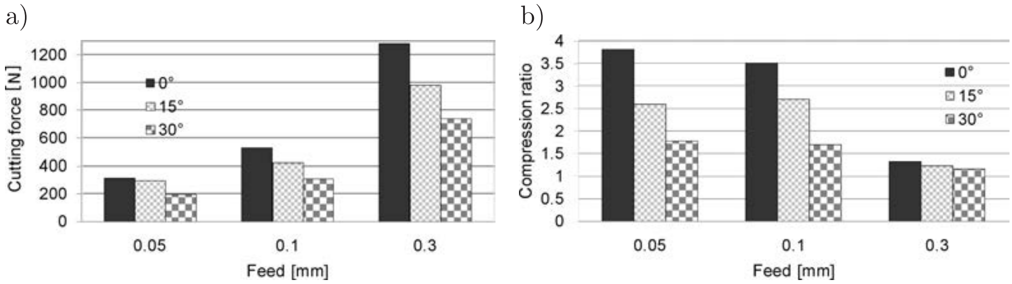

FIG. 4. Cutting force and compression ratio as a function of the tool rake angle and feed.

Variation of the compression ratio, defined as a ratio between the chip thickness and feed, decreases with both feed rate and tool rake angle, as shown in Fig. 4b. A high value is obtained for the small feed and tool rake angle ($f = 0.05$ mm and $\alpha = 0°$), while the small one corresponds to the high feed and tool rake angle ($f = 0.3$ mm and $\alpha = 30°$).

4.3. Tool-chip interface temperature

As shown in Fig. 5, the tool-chip interface temperature increases with the feed ($f = 0.05$, 0.1, and 0.3 mm) and decreases with the tool rake angle ($\alpha =$ 0, 15, and 30°). For the high feed (0.3 mm) and high rake angles (30°), the maximum temperature is about 250°C, while for the smallest one, i.e., for the feed (0.05 mm) and tool rake angle (0°), about 150°C is obtained.

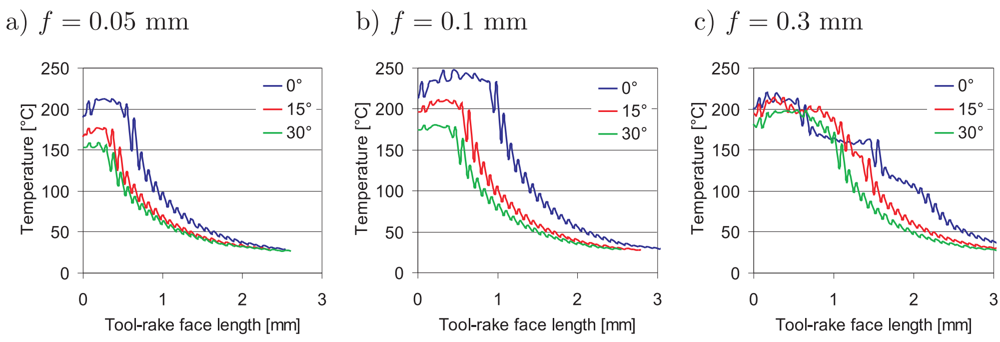

FIG. 5. Tool-rake face temperature distribution at the same cutting length.

The decrease in the temperature level with the rake angle can be explained by the fact that during machining of metallic materials, when the rake angle is large enough, the material flow occurs under sliding contact and with low plastic deformation at the secondary shear zone. Then the produced heat during the chip formation process is lower for the large angles than for the smallest one.

5. Conclusions

The numerical analysis of the cutting process shows in this study the impact of two cutting parameters on some important factors such as the chip morphology, cutting forces, temperature, and compression ratio. The main obtained results can be summarized as follows:

1. For small feeds ($f = 0.05$ and 0.1 mm), the chip has a continuous shape, while for high feeds ($f = 0.3$ mm) it exhibits a segmented shape. However, the numerical simulation for the segmentation process has to be improved, since for $f = 0.3$ mm and $\alpha = 30°$ a continuous shape is shown by experimental tests.
2. Cutting forces show an increase function vs. the feed rate and a decrease function vs. the tool rake angle. It has also been shown in numerical simulations that oscillations in the cutting force curve are obtained when the segmentation occurs.
3. The compression ratio is inversely proportional to both the feed rate and tool rake angle. With this parameter the plastic deformation intensity can be estimated in the chip.
4. One important result from this work concerns the evolution of the cutting temperature with cutting parameters. The numerical results confirm that the tool-chip temperature can be strongly controlled by the tool geometry and feed.

In a future work, chip segmentation prediction will be improved by introducing an adequate damage behaviour for the workpiece material. Simulations with a high cutting speed (HSM) will be performed to highlight its impact on the chip morphology and cutting force reduction.

References

1. ABAQUS Documentation for version 6.8. Dassault Systems Simulia, 2008.

2. Johnson G.R., Cook W.H., *Fracture characteristics of three metals subjected to various strains, strain rates, temperatures and pressures*, Engineering Fracture Mechanics, **21**, 31–48, 1985.

3. Li K., Gao X.-L., Sutherland J.W., *Finite element simulations of the orthogonal metal cutting process for qualitative understanding of the effects of crater wear on the chip formation process*, Journal of Materials Processing Technology, **127**, 309–324, 2002.

4. Limido J., Espinosa C., Salaün M., Lacome J.L., *SPH method applied to high speed cutting modelling*, International Journal of Mechanical Sciences, **49**, 898-908, 2007.

5. List G., Nouari M., Géhin D., Gomez S., Manaud J.P., Le Petitcoprs Y., Girot F., *Wear behaviour of cemented carbide tools dry machining of aluminium alloy*, Wear, **259**, 1177–1189, 2005.

6. Mebrouki T., Girardin F., Asad M., Rigal J-F., *Numerical and experimental study of dry cutting for an aeronautic aluminium alloy (A2024-T351)*, International Journal of Machine Tools and Manufacture, **48**, 1187–1197, 2008.

7. Molinari A., Moufki A., *The Merchant's model of orthogonal cutting revisited: A new insight into the modelling of chip formation*, International Journal of Mechanical Sciences, **50**, 124–131, 2008.

8. Ozlu E., Budak E., Molinari A., *Analytical and experimental investigation of rake contact and friction behaviour in metal cutting*, International Journal of Machine Tools and Manufacture, **49**, 865–875, 2009.

Received May 10, 2011; revised version August 23, 2011.

ENGINEERING TRANSACTIONS • *Engng. Trans.* • **60**, 1, 41–54, 2012
Polish Academy of Sciences • Institute of Fundamental Technological Research (IPPT PAN)
National Engineering School of Metz (ENIM)
SIXTY YEARS OF THE ENGINEERING TRANSACTIONS

Theoretical Basis of Determining the Translation and Rotation of Steering Wheel Stub Axle

Józef STRUSKI, Krzysztof WACH

Cracow University of Technology, Faculty of Mechanical Engineering
Institute of Automobiles and Internal Combustion Engines
Al. Jana Pawła II 37, 31-864 Kraków, Poland
e-mail: rust@mech.pk.edu.pl

In the paper a theoretical basis of determination of the steering wheel stub axle position and orientation in the suspension movements space, realized by the suspension mechanism are presented. The designed instrument allows measurement of quantities that are needed to compute the translation and orientation of the stub axleand to draw the kinematic characteristics of the suspension.

Key words: passenger car, multi-link suspension, steering wheel translation and orientation.

1. Introduction

Analysis of the car movement parameters on the curved track is one of the fundamental issues of stability and steerability. A change of these parameters is always caused by a change of the external forces acting on the vehicle.

The car comparative studies carried out so far show that even at the same kinematic extortion, realized by the change of steering angle, the change of the forces generated at the wheel-road contact patch is dependent on many factors associated with tire, suspension, and steering system construction.

Steering wheels are carried out against the car body through the spatial mechanisms with flexible constraints. Flexibility is the reason that during a car ride along the same path, with different speeds, the real kinematic steering ratio is changing; a significant difference between the real and theoretical steering angles appears. Measurement of real steering and camber angles in experimental car studies has a significant value. Results of such measurements are used to work out the relationships between car movement parameters as well as for stability and steerability evaluation [4, 9].

In case of independent suspensions, wheel vertical movements caused by unevenness of the road surface cause a track change. It leads to wheels drifting and adversely affects straight driving [6, 11]. Measurement of position and orientation of the wheel relative to the car body is very difficult, only a few studies on this topic, mainly related to the dynamic measurement of the steering angle, can be found in the literature [1, 7]. A Datron RV-3 instrument [12] allows measurement of position and orientation of the steering wheel relative to the car body. This measurement, however, is complicated and measured values are not obtained directly but as a result of complex calculations. This instrument has large dimensions and considerable weight as compared to the weight of the wheel. Persistence of the instrument is being reduced under the influence of dynamic loads generated while driving the car over the road unevenness.

2. The goal and scope of the work

The main goal of the work is introduction of an indirect measurement method of the stub axle with steering wheel translation and rotation.

The scope of this work concerns problems of resolving the kinematics of a four-link suspension and the proposed instrument mechanisms, as well as determination of the steering and camber angles and the characteristics of lateral displacements of the wheel centre.

3. Multi-link steering wheels suspension mechanism structure

In Fig. 1, a four-link steering wheel suspension mechanism scheme is shown. Points B_1, B_2, B_4, and B_5 are centres of ball joints connecting links with the stub axle. Point B_3 is the centre of the ball joint connecting steering linkage with the stub axle arm.

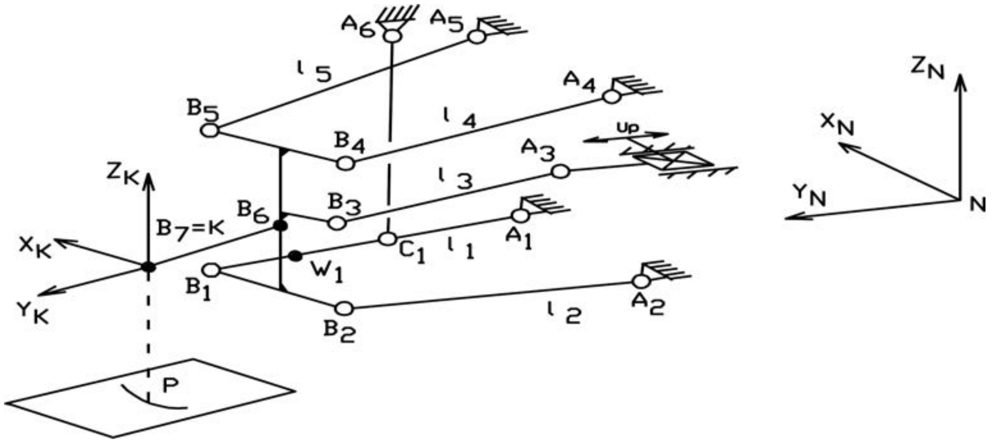

Fig. 1. Scheme of a four-link steering wheels suspension mechanism.

Points A_1, A_2, A_4, and A_5 are centres of ball joints which replace metal-rubber joints connecting links with the car body. Point A_3 is the centre of the ball joint connecting the steering linkage with a rack. A lower front link, represented in the figure by the link A_1B_1, is connected with an anti-roll bar at the point W. A telescopic column is connected with this link at the point C. Frames $\{N\}$ and $\{K\}$ are associated, respectively, with the car body and the stub axle.

4. Equations of geometric constrains of the suspension mechanism

The equations of geometric constraints of the mechanism shown in Fig. 1 can be written as 14 or 5 non-linear algebraic equations. In the first method the equations express squares of distances between characteristic points of the suspension:

$$\begin{aligned} &\mathbf{r}^T_{A_jB_j} \cdot \mathbf{r}_{A_jB_j} = l_j^2, \qquad \text{for } j = (1)5, \\ &\mathbf{r}^T_{B_jB_k} \cdot \mathbf{r}_{B_jB_k} = l_{jk}^2 \qquad \text{for } \begin{cases} j = 1 \ \text{ and } \ k = (2)5, \\ j = 2 \ \text{ and } \ k = (3)5, \\ j = 3 \ \text{ and } \ k = (4)5. \end{cases} \end{aligned} \tag{4.1}$$

In the above system of equations given parameters are: the coordinate z_{B1} of the point $B_1(x_{B1}, y_{B1}, z_{B1})$ and the steering rack displacement u_p, added to the coordinate y_{A3} of the point $A_3(x_{A3}, y_{A3}+u_p, z_{A3})$. At the given parameters z_{B1} and u_p, coordinates of the point $B_j(x_{Bj}, y_{Bj}, z_{Bk})$, for $j = 1, \ldots, 5$ and $k = 2, \ldots, 5$ are determined from the system (4.1). The constructional positions of the points B_6 and B_7 are given, therefore, determination of their coordinates in the movements space of the suspension $\{N\}$ is possible from the following systems of equations:

– for the point B_6

$$\mathbf{r}^T_{B_kB_j} \cdot \mathbf{r}_{B_kB_j} = l_{kj}^2, \qquad \text{for} \quad \begin{cases} k = 6 \ \text{ and } \ j = 1, \\ k = 6 \ \text{ and } \ j = 3, \\ k = 6 \ \text{ and } \ j = 5, \end{cases} \tag{4.2}$$

– for the point B_7

$$\mathbf{r}^T_{B_kB_j} \cdot \mathbf{r}_{B_kB_j} = l_{kj}^2, \qquad \text{for} \quad \begin{cases} k = 7 \ \text{ and } \ j = 1, \\ k = 7 \ \text{ and } \ j = 2, \\ k = 7 \ \text{ and } \ j = 4. \end{cases} \tag{4.3}$$

In the second method, the equations of the geometric constraints are expressed by the squares of lengths of vectors beginning and ending, respectively, at the points A_j and B_j, for $j = 1, \ldots, 5$, written as:

$$(4.4)\quad (\mathbf{r}_{NK.N}+\mathbf{A}_{NK}\cdot\mathbf{r}_{KB_j.K}-\mathbf{r}_{NA_j.N})^T \cdot(\mathbf{r}_{NK.N}+\mathbf{A}_{NK}\cdot\mathbf{r}_{KB_j.K}-\mathbf{r}_{NA_j.N}) = l_j^2, \qquad \text{for} \quad j=1,\ldots,5,$$

where

$$(4.5)\quad \mathbf{A}_{NK}=\mathbf{A}_\gamma\mathbf{A}_\beta\mathbf{A}_\alpha=\begin{bmatrix} c\gamma & -s\gamma & 0\\ s\gamma & c\gamma & 0\\ 0 & 0 & 1\end{bmatrix}\cdot\begin{bmatrix} c\beta & 0 & s\beta\\ 0 & 1 & 0\\ -s\beta & 0 & c\beta\end{bmatrix}\cdot\begin{bmatrix} 1 & 0 & 0\\ 0 & c\alpha & -s\alpha\\ 0 & s\alpha & c\alpha\end{bmatrix}$$

is a rotation matrix of $\{K\}$ against $\{N\}$.

From the system of Eq. (4.4) at given parameters q_3 and u_p, coordinates q_1 and q_2 of the wheel centre $K(q_1,\, q_2,\, q_3)$, as well as the rotation angles of $\{K\}$ against $\{N\}$: α, β, γ, are determined.

To ensure equivalence of the computing range of the algorithms based on the systems (4.1) and (4.4), determination of the rotation angles of $\{K\}:\alpha,\ \beta,\ \gamma$ against $\{N\}$ is needed. Thus, the system of Eqs. (4.1) must be supplemented by calculations of the mentioned angles. After calculating the coordinates of the points K and B_j $(j=1,\ldots,5)$ three vectors $\mathbf{r}_{KB_j}$ for $j\in\{1,2,3,4,5\}$ can be created. For each of these vectors a following matrix equation is satisfied:

$$(4.6)\qquad \mathbf{r}_{KB_j.K}=\mathbf{A}_{KN}\cdot\mathbf{r}_{KB_j.N},$$

where $\mathbf{r}_{KB_j.K}$ is a vector in $\{K\}$, $\mathbf{r}_{KB_j.N}$ is a vector in $\{N\}$,

$$(4.7)\quad \mathbf{A}_{KN}=\mathbf{A}_{NK}^T=\begin{bmatrix} c\beta\cdot c\gamma & c\beta\cdot s\gamma & -s\beta\\ s\alpha\cdot s\beta\cdot c\gamma-c\alpha\cdot s\gamma & s\alpha\cdot s\beta\cdot s\gamma+s\alpha\cdot c\gamma & s\alpha\cdot c\beta\\ c\alpha\cdot s\beta\cdot c\gamma+s\alpha\cdot s\gamma & c\alpha\cdot s\beta\cdot s\gamma-s\alpha\cdot c\gamma & c\alpha\cdot c\beta\end{bmatrix}.$$

Denoting the vectors' coordinates:

$$\mathbf{r}_{KB_j.K}=[x_{bj},y_{bj},z_{bj}]^T,\qquad \mathbf{r}_{KB_j.N}=[x_{jb},y_{jb},z_{jb}]^T$$

and assuming $j=n,m,v$ on the basis of (4.6) we obtain:

$$(4.8)\qquad \begin{aligned} x_{bn}&=(x_{nb}\cdot c\gamma+y_{nb}\cdot s\gamma)c\beta-z_{nb}\cdot s\beta,\\ x_{bm}&=(x_{mb}\cdot c\gamma+y_{mb}\cdot s\gamma)c\beta-z_{mb}\cdot s\beta,\\ x_{bv}&=(x_{vb}\cdot c\gamma+y_{vb}\cdot s\gamma)c\beta-z_{vb}\cdot s\beta.\end{aligned}$$

From the system of Eqs. (4.8), the rotation angles β and γ are calculated. In order to calculate the angle α Eq. (4.9) is used:

$$(4.9)\quad y_{bv}=(x_{vb}\cdot s\beta\cdot c\gamma)s\alpha-(x_{vb}\cdot s\gamma)c\alpha + (y_{vb}\cdot s\beta\cdot s\gamma)s\alpha+(y_{vb}\cdot c\gamma)c\alpha+(z_{vb}\cdot c\beta)s\alpha.$$

Then, having the rotation angles of the system $\{K\}$ against system $\{N\}$, coordinates of the vector $\mathbf{r}_{B_6B_7.N}$ are:

$$\mathbf{r}_{B_6B_7.N} = \mathbf{A}_{NK} \cdot \mathbf{r}_{B_6B_7.K}, \tag{4.10}$$

the unit vector $\mathbf{e}_K = [e_{kx}, e_{ky}, e_{kz}]^T$, lying on the wheel rotation axis, as well as the steering and camber angles:

$$\delta_k = -\operatorname{arc}\tan\left(\frac{e_{kx}}{e_{ky}}\right), \tag{4.11}$$

$$\gamma_k = -\operatorname{arc}\,\sin(e_{kz}), \tag{4.12}$$

were calculated.

Calculation of the angles δ_k and γ_k in both algorithms is similar.

It should be noted that solution of the algorithm based on the system of fourteen Eqs. (4.1) takes much less time than the solution based on the system (4.4) consisting of five transcendental equations [10].

5. Solving of the geometric constraints systems of equations of the suspension mechanism

Solutions of the systems of Eqs. (4.1) and (4.4) were obtained by the perturbation method [3, 7]. In the case of the five transcendental Eqs. (4.4) trigonometric functions were expanded into the series:

$$\sin(x_0 + x) = \sin x_0 + x\cos x_0 - \frac{x^2 \sin x_0}{2}, \tag{5.1}$$

$$\cos(x_0 + x) = \cos x_0 - x\sin x_0 - \frac{x^2 \cos x_0}{2}. \tag{5.2}$$

System of equations which can be written down in a general form:

$$f_j(q_1, q_2, \alpha, \beta, \gamma) = 0, \qquad j = 1, \ldots, 5, \tag{5.3}$$

were obtained.

Equations of the system (5.3) were separated into nonlinear and linear parts:

$$f_{jN}(q_1, q_2, \alpha, \beta, \gamma) + f_{jL}(q_1, q_2, \alpha, \beta, \gamma) = 0, \qquad j = 1, \ldots, 5. \tag{5.4}$$

Nonlinear parts of these equations were multiplied by the perturbation parameter ε and a system of auxiliary equations was obtained:

$$g_j(\varepsilon, q_1, q_2, \alpha, \beta, \gamma) = \varepsilon \cdot f_{jN} + f_{jL}, \qquad j = 1, \ldots, 5. \tag{5.5}$$

For $\varepsilon = 1$ systems of Eqs. (5.4) and (5.5) are identical, whereas for $\varepsilon = 0$ system (5.5) consists only of linear equations. It was assumed that solutions of the system (5.5) are the numerical series:

$$\tag{5.6} \begin{gathered} q_1 = \sum_{i=0}^{m} \varepsilon^i q_{1i}, \qquad q_2 = \sum_{i=0}^{m} \varepsilon^i q_{2i}, \\ \alpha = \sum_{i=0}^{m} \varepsilon^i \alpha_i, \qquad \beta = \sum_{i=0}^{m} \varepsilon^i \beta_i, \qquad \gamma = \sum_{i=0}^{m} \varepsilon^i \gamma_i. \end{gathered}$$

After substituting (5.6) to (5.5) we obtain:

$$\tag{5.7} g_j(\varepsilon, q_1(\varepsilon), q_2(\varepsilon), \alpha(\varepsilon), \beta(\varepsilon), \gamma(\varepsilon)) = 0, \qquad j = 1, \ldots, 5.$$

The system of Eq. (5.7) was expanded into a series with respect to ε powers:

$$\tag{5.8} \sum_{i=0}^{3} \varepsilon^i g_{ji} = 0, \qquad j = 1, \ldots, 5.$$

Then the linear systems of equations $g_{ji} = 0$ were solved, first for $i = 0$ then for $i = 1, 2, 3$. The solutions which can be presented in a general form:

$$\tag{5.9} \begin{gathered} q_1 = \sum_{i=0}^{3} q_{1i}, \qquad q_2 = \sum_{i=0}^{3} q_{2i}, \\ \alpha = \sum_{i=0}^{3} \alpha_i, \qquad \beta = \sum_{i=0}^{3} \beta_i, \qquad \gamma = \sum_{i=0}^{3} \gamma_i, \end{gathered}$$

were obtained.

The systems of Eqs. (4.1) were solved in an analogical way.

6. Characteristic points of the suspension mechanism coordinates

A constructional location of the mechanism in the suspension movements space $\{N\}$, defined by the coordinates of ball joints connecting links with the car body and the stub axle [2]:

A_1 $(144.1, 345.2, -92.2)$;	A_2 $(-229.2, 362.2, -101.7)$;
A_3 $(-99.7, 400.0, 306.2)$;	A_4 $(-69.0, 396.3, 413.5)$;
A_5 $(134.6, 428.5, 408.9)$;	B_1 $(28.7, 690.9, -98.0)$;
B_2 $(-24.4, 687.0, -131.6)$;	B_3 $(-135.7, 617.1, 286.9)$;
B_4 $(-18.1, 639.8, 388.4)$;	B_5 $(15.4, 673.3, 389.5)$.

The coordinates of points B_6 and $B_7 \equiv K$ lying on the wheel rotation axis:

$$B_6\ (0.5, 647.0, 1.1); \qquad B_7\ (1.0, 747.0, 0.6).$$

Coordinates values were given in [mm].

7. The structure and mobility of the measuring instrument mechanism

The measuring mechanism to determinate the translation and rotation of the steering wheel stub axle shown in Fig. 2 is composed of six links d_i, $i = 1, \ldots, 6$, connected by rotary-sliding kinematic pairs s_i, $i = 1, \ldots, 6$. At the points D_1, D_2, and D_3 links are connected with the stub axle by kinematic pairs. It is characteristic for this mechanism that the point D_1 is a common centre of three joints, point D_2 is a centre of two such joints, and the point D_3 is a centre of the ball joint. By points H_i, $i = 1, \ldots, 6$, centres of ball joints connecting links with the car body were noted in the figure.

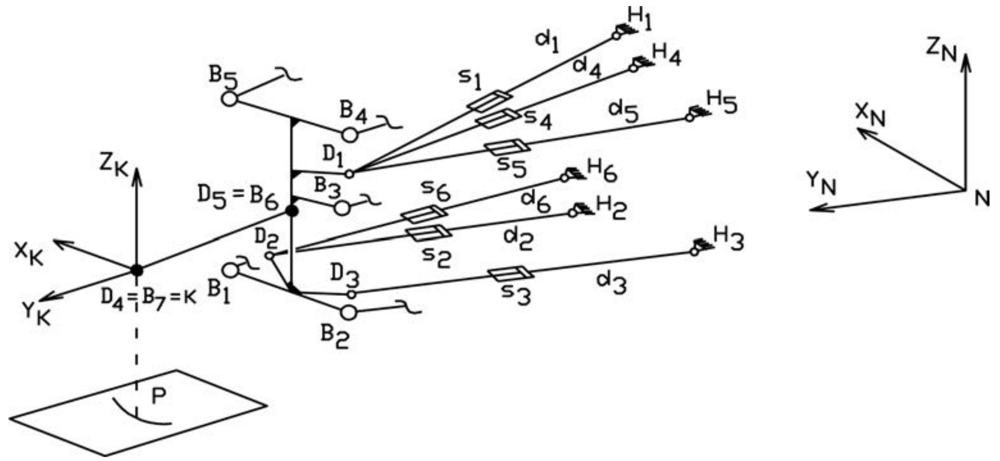

Fig. 2. Scheme of the measuring instrument to determine the translation and rotation of the steering wheel stub axle.

The instrument mechanism has 6 mobility degrees – using the formula from the theory of mechanisms and machines:

$$R = R_t - R_p, \tag{7.1}$$

where

$$R_t = 6(n-1) - \sum_{i=1}^{5} i \cdot p_i, \tag{7.2}$$

where R is real mobility of the mechanism, R_t is theoretical mobility of the mechanism, R_p is apparent mobility of the mechanism, p_i is kinematic pairs of the i-th class, n is number of links creating the mechanism.

With regard to the considered mechanism: $n = 13$, $p_4 = 6$, $p_3 = 12$, $p_5 = p_2 = p_1 = 0$, $R_t = 18$. After subtracting the apparent degrees of mobility $R_p = 12$ from the theoretical mobility, the real mobility $R = 6$; it is equal to the stub axle degrees of freedom in {N}.

8. Kinematics of the measuring instrument mechanism

Centres of the ball joints: D_1, D_2, and D_3 belong to the wheel stub axle. So the distances of these points from the points B_j, $j = 1, \ldots, 6$ can be calculated. However, the coordinates of the points: D_1, D_2, and D_3 in $\{N\}$ can be determined from the systems of equations:

– for the point D_1

$$\mathrm{r}^T_{B_j D_1.N} \cdot \mathbf{r}_{B_j D_1.N} = l^2_{D_1 B_j}, \qquad \text{for} \quad j = 1, 2, 3. \tag{8.1}$$

– for the point D_2

$$\mathbf{r}^T_{B_j D_2.N} \cdot \mathbf{r}_{B_j D_2.N} = l^2_{D_2 B_j}, \qquad \text{for} \quad j = 1, 3, 5. \tag{8.2}$$

– for the point D_3

$$\mathbf{r}^T_{B_j D_{3.N}} \cdot \mathbf{r}_{B_j D_3.N} = l^2_{D_3 B_j}, \qquad \text{for} \quad j = 2, 4, 5. \tag{8.3}$$

Thus, it becomes possible to calculate relative elongations s_i of links d_i, $i = 1, \ldots, 6$, relative to their constructional distances. Elongations s_i depend on the given parameters q_3 and u_p, i.e., $s_i(q_3, u_p)$.

In practical applications of the measuring instrument for determining the rotation and translation of the steering wheel stub axle it is needed to measure the coordinates of points D_1, D_2, and D_3, as well as H_i, $i = 1, \ldots, 6$, for the constructional suspension configuration; links elongations $s_i(q_3, u_p)$ measured by the sensors are also needed.

Determination of the steering wheel stub axle rotation and translation using a measuring instrument boils down to solving of the inverse problem. In this case, at given elongations $s_i(q_3$ and $u_p)$ of the links d_i, $i = (1)6$ and constructional positions of the points D_1, D_2, and D_3, as well as the additional point, e.g., $D_4 \equiv B_7$, the coordinates of these points as the functions of parameters q_3 and u_p should be determined from the systems of equations:

– for the point D_1

$$\mathbf{r}^T_{D_1 H_i.N} \cdot \mathbf{r}_{D_1 H.N} = (l_{D_1 H_i} + s_i)^2, \qquad \text{for} \quad i = 1, 4, 5. \tag{8.4}$$

– for the point D_2

$$
\begin{aligned}
&\mathbf{r}^T_{D_2D_1.N} \cdot \mathbf{r}_{D_2D_1.N} = l^2_{D_2D_1}, \\
&\mathbf{r}^T_{D_2H_i.N} \cdot \mathbf{r}_{D_2H_i.N} = (l_{D_2H_i} + s_i)^2, \qquad \text{for} \quad i = 2, 6.
\end{aligned} \tag{8.5}
$$

– for the point D_3

$$
\begin{aligned}
&\mathbf{r}^T_{D_3D_1.N} \cdot \mathbf{r}_{D_3D_1.N} = l^2_{D_3D_1}, \\
&\mathbf{r}^T_{D_3D_2.N} \cdot \mathbf{r}_{D_3D_2.N} = l^2_{D_3D_2}, \\
&\mathbf{r}^T_{D_3H_3.N} \cdot \mathbf{r}_{D_3H_3.N} = (l_{D_3H_3} + s_3)^2.
\end{aligned} \tag{8.6}
$$

– for the point D_4

$$
\begin{aligned}
&\mathbf{r}^T_{D_4D_1.N} \cdot \mathbf{r}_{D_4D_1.N} = l^2_{D_4D_1}, \\
&\mathbf{r}^T_{D_4D_2.N} \cdot \mathbf{r}_{D_4D_2.N} = l^2_{D_4D_2}, \\
&\mathbf{r}^T_{D_4D_3.N} \cdot \mathbf{r}_{D_4D_3.N} = l^2_{D_4D_3}.
\end{aligned} \tag{8.7}
$$

The coordinates of the point $\mathrm{D}_5 \equiv \mathrm{B}_6$ are calculated similarly to the one of the point D_4.

The way of determining the angles of rotation α, β, γ $\{K\}$ against $\{N\}$, the steering and camber angles δ_d, γ_d on the basis of the coordinates of the points D_i, $i = 1, \ldots, 5$, and the points B_j, $j = 1, \ldots, 6$, is the same.

9. Coordinates of the measuring instrument to the car body and the stub axle anchorage points

The coordinates of the centres of joints D_1, D_2, and D_3 in [mm], as well as coordinates of the points D_4 and D_5 belonging to the wheel rotation axis assigned to the constructional configuration of the suspension are given below:

$$
\begin{array}{lll}
H_1(90.0, 355.0, -40.0); & H_2(10.0, 250.0, -70.0); & H_3(-40.0, 280.0, 270.0); \\
H_4(45.0, 360.0, -90.0); & H_5(110.0, 362.0, 10.0); & H_6(30.0, 300.0, -95.0); \\
D_1(50.0, 560.0, -30.0); & D_2(25.0, 580.0, -90.0); & D_3(-50.0, 600.0, 200.0).
\end{array}
$$

The coordinates of the points $D_4 \equiv K$ and D_5 belonging to the wheel rotation axis are as follows:

$$
D_4(1.0, 747.0, 0.6); \qquad D_5(0.5, 647.0, 1.1).
$$

10. Characteristics of the stub axle rotation angles

In Fig. 3 the stub axle rotation angles characteristics are shown. α, β, and γ are angles of rotation of the frame $\{K\}$ against the x, y, z axes of the frame $\{N\}$.

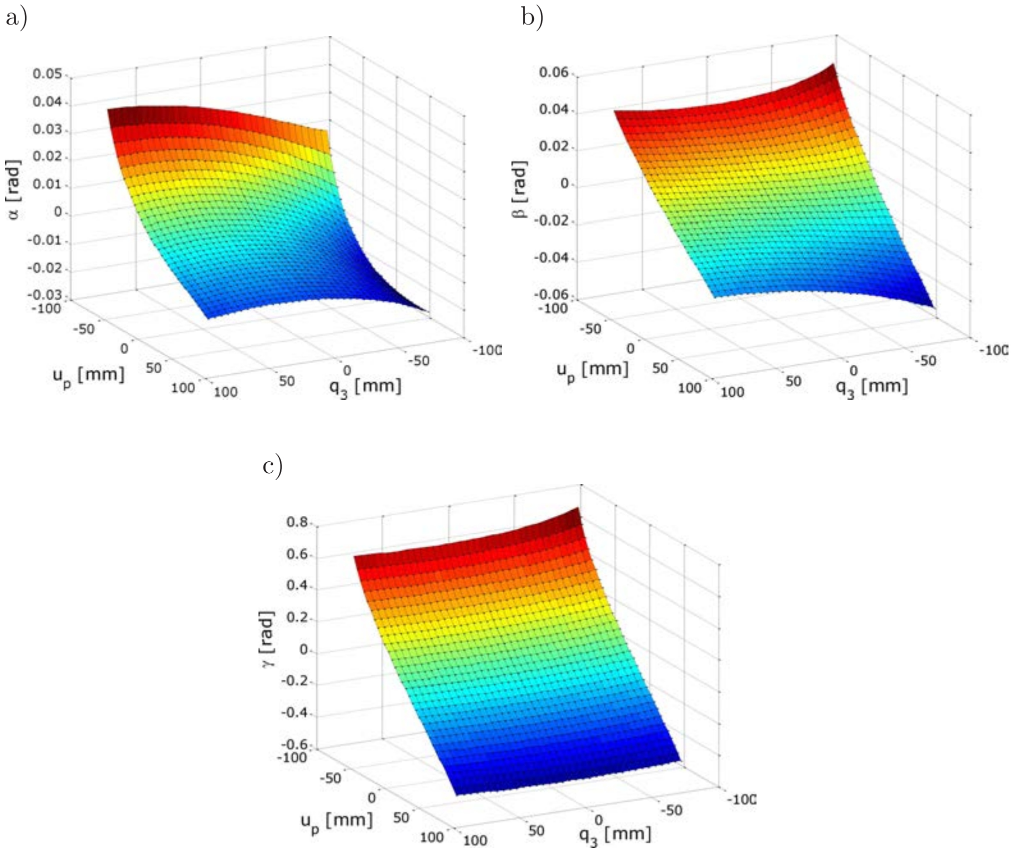

Fig. 3. Dependences of the stub axle rotation angles on suspension deflection q_3 and steering rack displacement u_p.

11. Elongations of the measuring instrument links as a function of the suspension deflection and the steering rack displacement

The following graphs show dependences of individual links of the measuring instrument elongations on the steering rack displacement u_p and the suspension deflection q_3. As the elongations of the sensors are simultaneously the suspension deflection and the steering rack displacement functions, they were shown on spatial graphs.

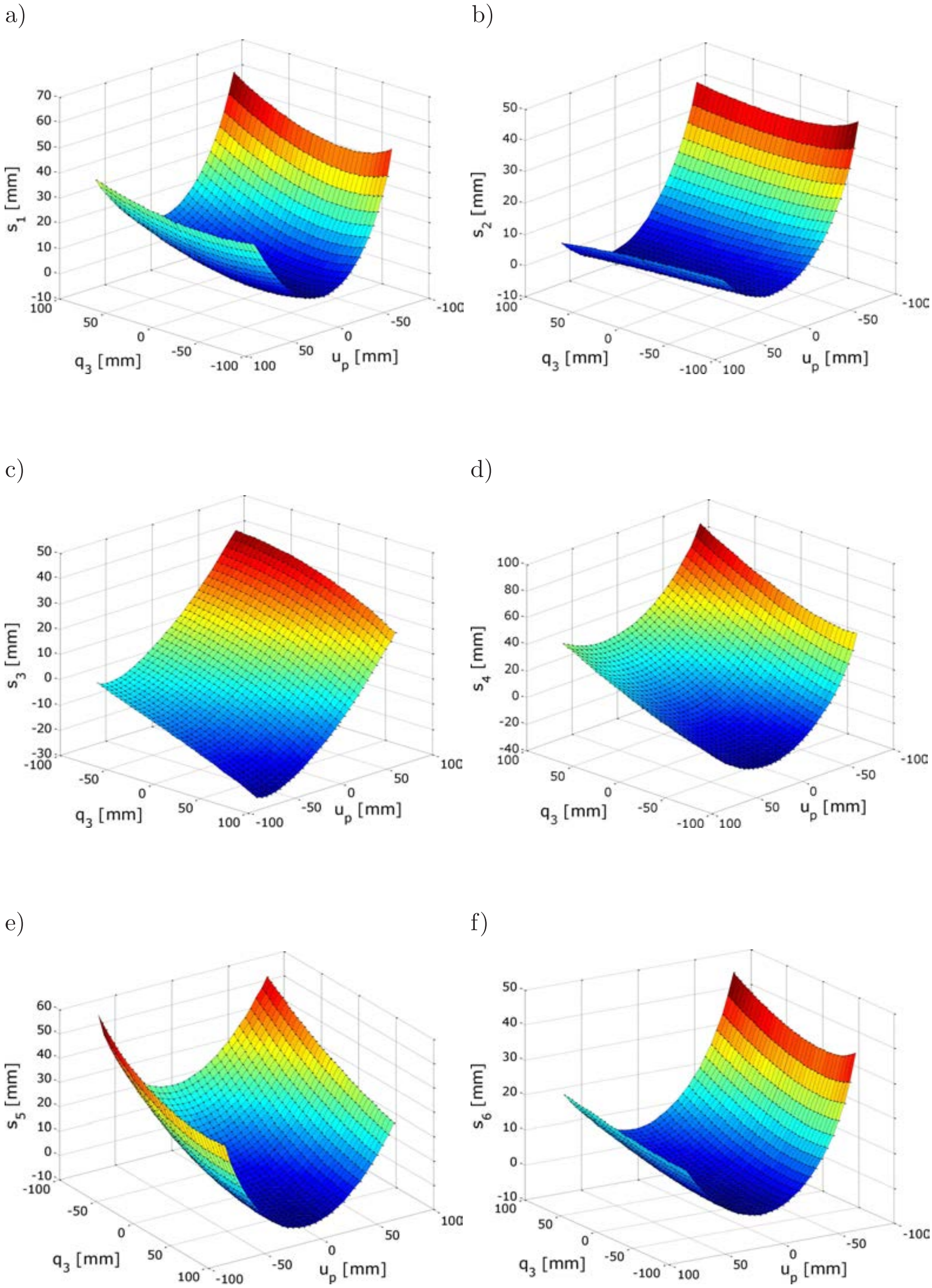

FIG. 4. Dependences of the measuring instrument links elongations on suspension deflection q_3 and steering rack displacement u_p.

12. Suspension characteristics

In Figs. 5, 6, and 7 characteristics of the analysed mechanism obtained on the basis of its kinematics solution and using the described measuring instrument are shown.

a) b)

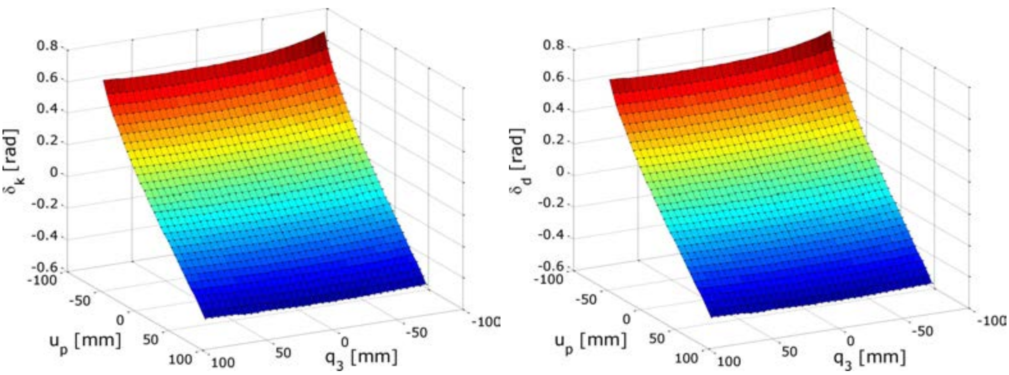

Fig. 5. Dependences of the steering angle δ on suspension deflection q_3 and steering rack displacement u_p, determined on the basis of: a) the suspension kinematics solution, b) using measuring instrument.

a) b)

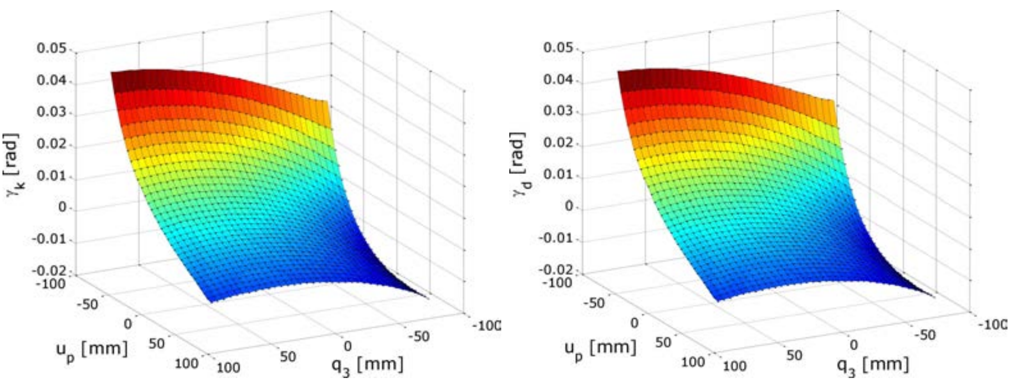

Fig. 6. Dependences of the camber angle γ on suspension deflection q_3 and steering rack displacement u_p, determined on the basis of: a) the suspension kinematics solution, b) using measuring instrument.

a) b)

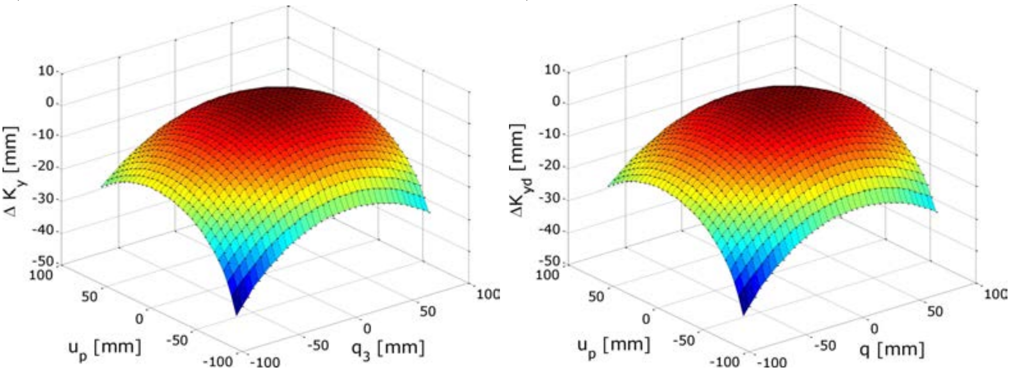

Fig. 7. Relative changes in the lateral position of the wheel centre, depending on suspension deflection q_3 and steering rack displacement u_p, determined on the basis of: a) the suspension kinematics solution, b) using measuring instrument.

13. Conclusion

The structure of the proposed measuring instrument mechanism enables its connection to the stub axle via three joints. One of these joints is a conjunction of three joints with a common centre, each with three degrees of freedom. This solution allows easiest measuring instrument joints to the stub axle connection. A Stewart platform mechanism can be used instead of the presented instrument to translation and rotation of the stub axle determination; it requires six ball joints connections to the stub axle.

The basis of the method of indirect measurement of translation and rotation of the stub axle with the steering wheel in the suspension movements space are algorithms that include geometric constraints system of equations of four-link suspension and measuring instrument mechanisms. Solutions of these systems of equations were used to compile characteristics of steering and camber angles and of wheel centre displacement in the lateral direction.

On the basis of an analysis of the results of a computer simulation of the measure method it is to conclude that the worked out instrument can be used in experimental car tests.

Analysis of the kinematic characteristics contained in the work shows that the examined mechanism does not have singular points in the suspension movements space.

References

1. Blumenfeld W., Schneider W., *Opto-electronic measuring method of steering and camber angles of driven vehicle* [in German: *Opto-elektronisches Verfahren zur Spur- und Sturz-winkelmessung am fahrenden Farzeug*], ATZ, **87**, 1, 17–21, 1985.

2. Góra M., *The kinematic analysis of multi-link suspensions car mechanisms* [in Polish: *Analiza kinematyczna wielowahaczowych mechanizmów zawieszeń samochodów*], Doctoral Thesis, Cracow University of Technology, Kraków, 2008.

3. Grzyb A., *On a perturbation method for the analysis of the kinetostatics of mechanisms*, Akademie Verlag, ZAMM, Z. Angew. Math. Mech., **72**, 615–618, 1992.

4. Janczur R., *The experimental analytic method of car handling characteristics study* [in Polish: *Analityczno-eksperymentalna metoda badań sterowności samochodów*], Doctoral Thesis, Cracow University of Technology, Kraków, 2002.

5. Reimpell J., Betzler W., *Car chassis. Basics of construction* [in Polish: *Podwozia samochodów. Podstawy konstrukcji*], WKiŁ, Warszawa, 2002.

6. Rill G., *Steady State Cornering on Uneven Roadways*, SEA Technical Paper No. **860575**, Warrendale, PA, 1986.

7. Struski J., Kowalski M., *Theoretical basis of generalized tasks on the parametrization of wheel guidance systems with respect to the car body* [in Polish: *Podstawy teoretyczne uogólnionych zagadnień z zakresu parametryzacji układów prowadzenia kół względem nadwozia*], Czasopismo Techniczne PK, **6**, 119–129, 2008.

8. Struski J., *Instrument for dynamic steering angle measuring* [in Polish: *Przyrząd do pomiaru dynamicznego kąta skrętu koła kierowanego*], Patent no. P-267693.

9. Struski J., *Quasi-statistic modelling of car handling* [in Polish: *Quasi-statyczne modelowanie sterowności samochodu*], Wydawnictwo Politechniki Krakowskiej, Monograph **144**, Cracow, 1993.

10. Struski J., Kowalski M., *Influence of the multi-link suspensions mechanisms geometric constraints equations structure on numerical efficiency* [in Polish: *Wpływ struktury równań więzów geometrycznych mechanizmów wielowahaczowych zawieszeń kół na efektywność numeryczną*], Conference materials of XV Scientific Workshops PTSK, Krynica Zdrój, 2010.

11. Walczak S., *Analysis of the dynamic loads of different types of independent suspensions* [in Polish: *Analiza dynamicznych obciążeń różnych typów niezależnego zawieszenia kół samochodu*], Doctoral Thesis, Cracow University of Technology, Kraków, 2003.

12. CORSYS-DATRON RV-3, *Wheel Vector Sensor*, User manual, Wetzlar, Germany, 2006.

Received June 10, 2011; revised version January 12, 2012.

ENGINEERING TRANSACTIONS • *Engng. Trans.* • **60**, 1, 55–68, 2012
Polish Academy of Sciences • Institute of Fundamental Technological Research (IPPT PAN)
National Engineering School of Metz (ENIM)
SIXTY YEARS OF THE ENGINEERING TRANSACTIONS

Effect of Rotation and Suspended Particles on the Stability of an Incompressible Walters' (Model B') Fluid Heated from Below Under a Variable Gravity Field in a Porous Medium

G.C. RANA[1)], SANJEEV KUMAR[2)]

[1)] *NSCBM Govt. P. G. College*
Department of Mathematics
Hamirpur-177 005, Himachal Pradesh, India
e-mail: drgcrana15@gmail.com

[2)] *Govt. P. G. College, Department of Mathematics*
Mandi-175 001, Himachal Pradesh, India

The effect of rotation and suspended particles on the stability of an incompressible Walters' (model B') fluid heated from below under a variable gravity field in a porous medium is considered. By applying a normal mode analysis method, the dispersion relation has been derived and solved numerically. It is observed that the rotation, gravity field, suspended particles, and viscoelasticity introduce oscillatory modes. For stationary convection, the rotation has a stabilizing effect and suspended particles are found to have a destabilizing effect on the system, whereas the medium permeability has a stabilizing or destabilizing effect on the system under certain conditions. The effect of rotation, suspended particles, and medium permeability has also been shown graphically.

Key words: Walters' (model B') fluid, rotation, suspended particles, variable gravity field, porous medium.

MSC 2010: 76A05; 76A10; 76E06; 76E07; 76E19; 76E25; 76S05.

Notations

$\mathbf{q}$ – velocity of fluid,
p – pressure,
$\mathbf{g}$ – gravitational acceleration vector,
g – gravitational acceleration,
k – wave number of disturbance,
p_1 – thermal Prandtl number,
P_l – dimensionless medium permeability.

Greek symbols

ϵ – medium porosity,
$\boldsymbol{\rho}$ – fluid density,
μ – fluid viscosity,
μ' – fluid viscoelasticity,
υ – kinematic viscosity,
υ' – kinematic viscoelasticity,
κ – thermal diffusitivity,
α – thermal coefficient of expansion,
β – adverse temperature gradient,
θ – perturbation in temperature,
δ – perturbation in respective physical quantity,
ζ – Z-component of vorticity,
$\mathbf{\Omega}$ – rotation vector having components $(0, 0, \Omega)$.

1. Introduction

A detailed account of the thermal instability of a Newtonian fluid under varying assumptions of hydrodynamics and hydromagnetics has been given by Chandrasekhar [1]. Lapwood [2] has studied the convective flow in a porous medium using the linearized stability theory. The Rayleigh instability of a thermal boundary layer in flow through a porous medium has been considered by Wooding [15], whereas Scanlon and Segel [7] have considered the effect of suspended particles on the onset of Be'nard convection and found that the critical Rayleigh number was reduced solely because the heat capacity of the pure gas was supplemented by the particles. The suspended particles were thus found to destabilize the layer. Sharma [8] has studied thermal instability of a viscoelastic fluid in hydromagnetics.

Sharma and Sunil [9] have studied thermal instability of an Oldroydian viscoelastic fluid with suspended particles in hydromagnetics in a porous medium. There are many viscoelastic fluids that cannot be characterized by Maxwell's or Oldroyd's constitutive relations. One such class of fluids is Walters' (model B') viscoelastic fluid having relevance both in the chemical technology and industry. Walters' [14] reported that the mixture of polymethyl methacrylate and pyridine at 25°C containing 30.5 g of polymer per litre with density 0.98 g per litre behaves very nearly as the Walters (model B') viscoelastic fluid. Walters' (model B') viscoelastic fluid forms the basis for the manufacture of many important polymers and useful products.

Stommel and Fedorov [13] and Linden [3] have remarked that the length scalar characteristic of double diffusive convecting layers in the ocean may be sufficiently large, so that the Earth's rotation might be important in their formation. Moreover, the rotation of the Earth distorts the boundaries of a hexagonal convection cell in a fluid through a porous medium, and the distortion plays an important role in extraction of energy in geothermal regions. The problem of thermal instability of a fluid in a porous medium is of importance in geophysics, soil sciences, ground water hydrology, and astrophysics. The scientific importance of the field has also increased because hydrothermal circulation is the dominant heat transfer mechanism in the development of a young oceanic crust (Lister, [4]).

Thermal instability of a fluid layer under a variable gravitational field heated from below or above is investigated analytically by Pradhan and Samal [5]. Although the gravity field of the Earth is varying with the height from its surface, we usually neglect this variation for laboratory purposes and treat the field as constant. However, this may not be the case for large scale flows in the ocean, atmosphere, or mantle. It can become imperative to consider gravity as a quantity varying with distance from the centre of the Earth.

Sharma and Rana [10] have studied thermal instability of a Walters' (model B') viscoelastic fluid in the presence of a variable gravity field and rotation in a porous medium. Sharma and Rana [11] have also studied the thermosolutal instability of Rivlin-Ericksen rotating fluid in the presence of a magnetic field and variable gravity field in a porous medium. Recently, Sharma and Gupta [12] have studied the effect of rotation on thermal convection of micropolar fluids in the presence of suspended particles, whereas Rana and Kango [6] have studied the effect of rotation on thermal instability of a compressible Walters' (model B') viscoelastic fluid in a porous medium.

Keeping in mind the importance in various applications mentioned above, our interest in the present paper is to study the effect of rotation and suspended particles on the stability of an incompressible Walters' (model B') fluid heated from below under a variable gravity field in a porous medium.

2. Formulation of the problem and perturbation equations

Here we consider an infinite, horizontal, incompressible Walters' (model B') viscoelastic fluid of the depth d, bounded by the planes $z = 0$ and $z = d$ in an isotropic and homogeneous medium of porosity ϵ and permeability k_1, which is acted upon by a uniform rotation $\mathbf{\Omega}(0, 0, \Omega)$ and variable gravity $\mathbf{g}(0, 0, -g)$, where $g = \lambda g_0$, $g_0(> 0)$ is the value of g at $z = 0$, and λ can be positive or negative as the gravity increases or decreases upwards from its value g_0. This layer is heated from below such that a steady adverse temperature gradient $\beta \left(= \left|\frac{dT}{dz}\right|\right)$ is maintained. The character of equilibrium of this initial static state is determined by supposing that the system is slightly disturbed and then following its further evolution.

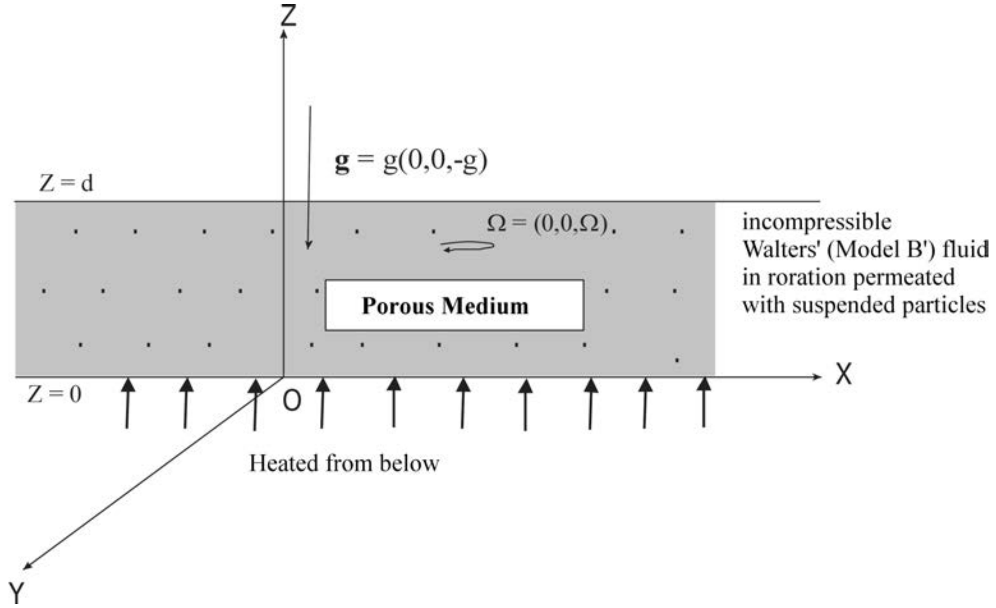

Schematic Sketch of Physical Situation

Let ρ, υ, υ', p, ϵ, T, α, and $\mathbf{q}(0,0,0)$, denote, respectively, the density, kinematic viscosity, kinematic viscoelasticity, pressure, medium porosity, temperature, thermal coefficient of expansion, and velocity of the fluid. The equations expressing the conservation of momentum, mass, temperature, and equation of state for the Walters' (model B') viscoelastic fluid are as follows:

$$\text{(2.1)}\quad \frac{1}{\epsilon}\left[\frac{\partial q}{\partial t}+\frac{1}{\epsilon}(q.\nabla)\,q\right]=-\frac{1}{\rho_0}\nabla p+g\left(1+\frac{\delta\rho}{\rho_0}\right)$$
$$-\frac{1}{k_1}\left(\upsilon-\upsilon'\frac{\partial}{\partial t}\right)q+\frac{2}{\epsilon}(q\times\Omega)+\frac{K'N}{\rho_0\epsilon}(q_d-q),$$

$$\text{(2.2)}\qquad \nabla.q=0,$$

$$\text{(2.3)}\qquad E\frac{\partial T}{\partial t}+(q.\nabla)\,T+\frac{mNC_{pt}}{\rho_0 C_f}\left[\epsilon\frac{\partial}{\partial t}+q_d.\nabla\right]T=\kappa\,\nabla^2\mathrm{T},$$

and

$$\text{(2.4)}\qquad \rho=\rho_0\left[1-\alpha(T-T_0)\right],$$

where the suffix zero refers to values at the reference level $z=0$.

Here $q_d(\overline{x}, t)$ and $N(\overline{x}, t)$ denote the velocity and number density of the particles, respectively, $q_d = (l, r, s)$, $\overline{x} = (xyz)$, $K = 6\pi\eta\rho v$, where η is the Stokes drag coefficient, where η is the particle radius and,

$$E = \epsilon + (1 - \epsilon)\left(\frac{\rho_s c_s}{\rho_0 c_f}\right)$$

is constant, κ is the thermal diffusivity, and ρ_s, c_s, ρ_0, c_f denote the density and heat capacity of the solid (porous) matrix and fluid, respectively.

If mN is the mass of particles per unit volume, then the equations of motion and continuity for the particles are as follows:

$$mN\left[\frac{\partial q_d}{\partial t} + \frac{1}{\epsilon}\left(q_d.\nabla\right) q_d\right] = K'N\left(q - q_d\right), \tag{2.5}$$

$$\epsilon\frac{\partial N}{\partial t} + \nabla.\left(Nq_d\right) = 0. \tag{2.6}$$

The presence of particles adds an extra force term proportional to the velocity difference between particles and fluid, and appears in the equation of motion (2.1). Since the force exerted by the fluid on the particles is equal and opposite to that exerted by the particles on the fluid, there must be an extra force term, equal in magnitude but opposite in sign, in the equations of motion for the particles (2.6). The buoyancy force on the particles is neglected. Interparticles' reactions are not considered either since we assume that the distance between the particles is quite large as compared to their diameters. These assumptions have been used in writing the equations of motion (2.6) for the particles.

The initial state of the system is taken to be quiescent layer (no settling) with a uniform particle distribution number. The initial state is as follows:

$$\begin{gathered} q = (0,0,0), \qquad q_d = (0,0,0), \\ T = -\beta z + T_0, \qquad \rho = \rho_0(1 + \alpha\beta z), \qquad N_0 = \text{ constant} \end{gathered} \tag{2.7}$$

and is an exact solution to the governing equations.

Let $q(u, v, w)$, $q_d(l, r, s)$, θ, δp, and $\delta\rho$ denote the perturbations, respectively, in fluid velocity $q(0,0,0)$, particle velocity $q_d(0,0,0)$, temperature T, pressure p, and density ρ.

The change in density $\delta\rho$ caused by the perturbation θ in temperature is given by:

$$\delta\rho = -\alpha\rho_0\theta. \tag{2.8}$$

The linearized perturbation equations governing the motion of fluids are as follows:

$$\frac{1}{\epsilon}\frac{\partial q}{\partial t} = -\frac{1}{\rho_0}\nabla\delta p - g\frac{\delta\rho}{\rho_0} - \frac{1}{k_1}\left(\upsilon - \upsilon'\frac{\partial}{\partial t}\right)q + \frac{K'N}{\epsilon}\left(q_d - q\right) + \frac{2}{\epsilon}\left(q \times \Omega\right), \tag{2.9}$$

$$\nabla q = 0, \tag{2.10}$$

$$\left(\frac{m}{K'}\frac{\partial}{\partial t} + 1\right)q_d = q, \tag{2.11}$$

$$\left(E + b\epsilon\right)\frac{\partial\theta}{\partial t} = \beta\left(w + bs\right) + \kappa\nabla^2\theta, \tag{2.12}$$

where $b = \dfrac{mNC_{pt}}{\rho_0 C_f}$, and w, s are the vertical fluid and particles velocity.

In the Cartesian form, Eqs. (2.9)–(2.12) with the help of Eq. (2.8) can be expressed as follows:

$$\frac{1}{\epsilon}\left(\frac{m}{K'}\frac{\partial}{\partial t} + 1\right)\frac{\partial u}{\partial t} = -\frac{1}{\rho_0}\left(\frac{m}{K'}\frac{\partial}{\partial t} + 1\right)\frac{\partial}{\partial x}\left(\delta p\right) - \frac{1}{k_1}\left(\upsilon - \upsilon'\frac{\partial}{\partial t}\right)\left(\frac{m}{K'}\frac{\partial}{\partial t} + 1\right)u - \frac{mN}{\epsilon\rho_0}\frac{\partial u}{\partial t} + \frac{2}{\epsilon}\left(\frac{m}{K'}\frac{\partial}{\partial t} + 1\right)\Omega v, \tag{2.13}$$

$$\frac{1}{\epsilon}\left(\frac{m}{K'}\frac{\partial}{\partial t} + 1\right)\frac{\partial v}{\partial t} = -\frac{1}{\rho_0}\left(\frac{m}{K'}\frac{\partial}{\partial t} + 1\right)\frac{\partial}{\partial y}\left(\delta p\right) - \frac{1}{k_1}\left(\upsilon - \upsilon'\frac{\partial}{\partial t}\right)\left(\frac{m}{K'}\frac{\partial}{\partial t} + 1\right)v - \frac{mN}{\epsilon\rho_0}\frac{\partial v}{\partial t} + \frac{2}{\epsilon}\left(\frac{m}{K'}\frac{\partial}{\partial t} + 1\right)\Omega u, \tag{2.14}$$

$$\frac{1}{\epsilon}\left(\frac{m}{K'}\frac{\partial}{\partial t} + 1\right)\frac{\partial w}{\partial t} = -\frac{1}{\rho_0}\left(\frac{m}{K'}\frac{\partial}{\partial t} + 1\right)\frac{\partial}{\partial z}\left(\delta p\right) - \frac{1}{k_1}\left(\upsilon - \upsilon'\frac{\partial}{\partial t}\right)\left(\frac{m}{K'}\frac{\partial}{\partial t} + 1\right)w - \frac{mN}{\epsilon\rho_0}\frac{\partial w}{\partial t} + g\left(\frac{m}{K'}\frac{\partial}{\partial t} + 1\right)\alpha\theta, \tag{2.15}$$

$$\frac{\partial u}{\partial x} + \frac{\partial v}{\partial y} + \frac{\partial w}{\partial z} = 0, \tag{2.16}$$

$$\left(E + b\epsilon\right)\frac{\partial\theta}{\partial t} = \beta\left(w + bs\right) + \kappa\nabla^2\theta. \tag{2.17}$$

Operating Eqs. (2.13) and (2.14) by $\frac{\partial}{\partial x}$ and $\frac{\partial}{\partial y}$, respectively, adding them and using Eq. (2.16), we get:

$$\begin{aligned}(2.18)\qquad \frac{1}{\epsilon}\left(\frac{m}{K'}\frac{\partial}{\partial t}+1\right)\frac{\partial}{\partial t}\left(\frac{\partial w}{\partial z}\right) &= \frac{1}{\rho_0}\left(\frac{m}{K'}\frac{\partial}{\partial t}+1\right)\left(\nabla^2-\frac{\partial^2}{\partial z^2}\right)\delta p \\ &- \frac{1}{k_1}\left(\upsilon-\upsilon'\frac{\partial}{\partial t}\right)\left(\frac{m}{K'}\frac{\partial}{\partial t}+1\right)\left(\frac{\partial w}{\partial z}\right)-\frac{mN}{\epsilon\rho_0}\frac{\partial}{\partial t}\left(\frac{\partial w}{\partial z}\right) \\ &- \frac{2}{\epsilon}\left(\frac{m}{K'}\frac{\partial}{\partial t}+1\right)\Omega\zeta,\end{aligned}$$

where $\zeta = \frac{\partial v}{\partial x}-\frac{\partial u}{\partial y}$ is the z-component of vorticity.

Operating Eqs. (2.15) and (2.18) by $\left(\nabla^2-\frac{\partial^2}{\partial z^2}\right)$ and $\frac{\partial}{\partial z}$, respectively, and adding them to eliminate δp between these equations, we get:

$$\begin{aligned}(2.19)\qquad \frac{1}{\epsilon}\left(\frac{m}{K'}\frac{\partial}{\partial t}+1\right)\frac{\partial}{\partial t}\left(\nabla^2 w\right) &= -\frac{1}{k_1}\left(\upsilon-\upsilon'\frac{\partial}{\partial t}\right)\left(\frac{m}{K'}\frac{\partial}{\partial t}+1\right)\nabla^2 w \\ &+ g\left(\frac{\partial^2}{\partial x^2}+\frac{\partial^2}{\partial y^2}\right)\left(\frac{m}{K'}\frac{\partial}{\partial t}+1\right)\alpha\theta-\frac{mN}{\epsilon\rho_0}\frac{\partial}{\partial t}\left(\nabla^2 w\right) \\ &- \frac{2}{\epsilon}\left(\frac{m}{K'}\frac{\partial}{\partial t}+1\right)\Omega\frac{\partial\zeta}{\partial z},\end{aligned}$$

where $\nabla^2 = \frac{\partial^2}{\partial x^2}+\frac{\partial^2}{\partial y^2}+\frac{\partial^2}{\partial z^2}$.

Operating Eqs. (2.13) and (2.14) by $-\frac{\partial}{\partial y}$ and $\frac{\partial}{\partial x}$, respectively, and adding them, we get

$$\begin{aligned}(2.20)\qquad \frac{1}{\epsilon}\left(\frac{m}{K'}\frac{\partial}{\partial t}+1\right)\frac{\partial\zeta}{\partial t} &= -\frac{1}{k_1}\left(\upsilon-\upsilon'\frac{\partial}{\partial t}\right)\left(\frac{m}{K'}\frac{\partial}{\partial t}+1\right)\zeta \\ &- \frac{mN}{\epsilon\rho_0}\frac{\partial\zeta}{\partial t}+\frac{2}{\epsilon}\left(\frac{m}{K'}\frac{\partial}{\partial t}+1\right)\Omega\frac{\partial w}{\partial z}.\end{aligned}$$

3. The dispersion relation

Following the normal mode analyses, we assume that the perturbation quantities have x, y, and t dependence of the form:

$$(3.1)\qquad [w,s,\theta,\zeta] = [W(z),S(z),\Theta(z),Z(z)]\exp\left(ik_x x+ik_y y+nt\right),$$

where k_x and k_y are the wave numbers in the x and y directions, $k = \left(k_x^2 + k_y^2\right)^{1/2}$ is the resultant wave number, and n is the frequency of the harmonic disturbance, which is, in general, a complex constant.

Using expression (3.1) Eqs. (2.19), (2.20), and (2.17) become:

$$\frac{n}{\epsilon}\left[\frac{d^2}{dz^2} - k^2\right] W = -gk^2\alpha\Theta - \frac{1}{k_1}\left(\upsilon - \upsilon' n\right)\left(\frac{d^2}{dz^2} - k^2\right) W - \frac{mNn}{\epsilon\rho_0\left(\frac{m}{K'}n + 1\right)}\left(\frac{d^2}{dz^2} - k^2\right) W - \frac{2\Omega}{\epsilon}\frac{dZ}{dz}, \tag{3.2}$$

$$\frac{n}{\epsilon} Z = -\frac{1}{k_1}\left(\upsilon - \upsilon' n\right) - \frac{mNn}{\epsilon\rho_0\left(\frac{m}{K'}n + 1\right)} Z + \frac{2\Omega}{\epsilon}\frac{dW}{dz}, \tag{3.3}$$

$$\left(E + b\epsilon\right) n\Theta = \beta\left(W + bS\right) + \kappa\left(\frac{d^2}{dz^2} - k^2\right)\Theta. \tag{3.4}$$

Equations (3.2)–(3.4) in a non-dimensional form become:

$$\left[\frac{\sigma}{\epsilon}\left(1 + \frac{M}{1 + \tau_1\sigma}\right) + \frac{1 - F\sigma}{P_l}\right]\left(D^2 - a^2\right) W + \frac{ga^2d^2\alpha\Theta}{\upsilon} + \frac{2\Omega d^3}{\epsilon\upsilon} DZ = 0, \tag{3.5}$$

$$\left[\frac{\sigma}{\epsilon}\left(1 + \frac{M}{1 + \tau_1\sigma}\right) + \frac{1 - F\sigma}{P_l}\right] Z = \left(\frac{2\Omega d}{\epsilon\upsilon}\right) DW, \tag{3.6}$$

$$\left[\left(D^2 - a^2\right) - E_1 p_1 \sigma\right]\Theta = -\frac{\beta d^2}{\kappa}\left(\frac{B + \tau_1\sigma}{1 + \tau_1\sigma}\right) W, \tag{3.7}$$

where we have put:

$$a = kd, \qquad \sigma = \frac{nd^2}{\upsilon}, \qquad \tau = \frac{m}{K'}, \qquad \tau_1 = \frac{\tau\upsilon}{d^2},$$
$$M = \frac{mN}{\rho_0}, \qquad E_1 = E + b\epsilon, \qquad B = b + 1, \qquad F = \frac{\upsilon'}{d^2},$$

and $P_l = \frac{k_1}{d^2}$ is the dimensionless medium permeability, $p_1 = \frac{\upsilon}{\kappa}$, is the thermal Prandtl number.

Eliminating Θ and Z from Eqs. (3.5)–(3.7), we obtain:

$$\left[\frac{\sigma}{\epsilon}\left(1 + \frac{M}{1 + \tau_1\sigma}\right) + \frac{1 - F\sigma}{P_l}\right]\left(D^2 - a^2\right)\left(D^2 - a^2 - E_1 p_1\sigma\right) W - Ra^2\lambda\left(\frac{B + \tau_1\sigma}{1 + \tau_1\sigma}\right) W + \left[\frac{\frac{T_A}{\epsilon^2}\left(D^2 - a^2 - E_1 p_1\sigma\right)}{\frac{\sigma}{\epsilon}\left(1 + \frac{M}{1 + \tau_1\sigma}\right) + \frac{1 - F\sigma}{P_l}}\right] D^2 W = 0, \tag{3.8}$$

where $R = \dfrac{g_0 \alpha \beta d^4}{\upsilon \kappa}$, is the thermal Rayleigh number and $T_A = \left(\dfrac{2\Omega d^2}{\upsilon}\right)^2$, is the Taylor number.

Here we assume that the temperature at the boundaries is kept fixed, the fluid layer is confined between two boundaries, and adjoining medium is electrically non-conducting. The boundary conditions appropriate to the problem are (Chandrasekhar, [1]):

$$W = D^2 W = DZ = \Theta = 0 \qquad \text{at} \qquad z = 0 \qquad \text{and} \qquad z = 1. \tag{3.9}$$

The case of two free boundaries, though a little artificial, is the most appropriate for stellar atmospheres. Using the boundary conditions (3.9), we can show that all the even order derivatives of W must vanish for $z = 0$ and $z = 1$, and hence the proper solution of W characterizing the lowest mode is:

$$W = W_0 \sin \pi z, \tag{3.10}$$

where W_0 is a constant.

Substituting Eq. (3.10) in (3.8), we obtain the following dispersion relation:

$$\begin{aligned} R_1 x \lambda = {} & \left[\frac{i\sigma_1}{\epsilon}\left(1 + \frac{M}{1 + \tau_1 \pi^2 i\sigma_1}\right) + \frac{1 - F\pi^2 i\sigma_1}{P}\right] \\ & \cdot (1+x)(1+x+E_1 p_1 i\sigma_1)\left(\frac{1+\tau_1\pi^2 i\sigma_1}{B+\tau_1\pi^2 i\sigma_1}\right) \\ & + \frac{\dfrac{T_{A_1}}{\epsilon^2}(1+x+E_1 p_1 i\sigma_1)}{\dfrac{i\sigma_1}{\epsilon}\left(1 + \dfrac{M}{1+\tau_1\pi^2 i\sigma_1}\right) + \dfrac{1-F\pi^2 i\sigma_1}{P}}\left(\frac{1+\tau_1\pi^2 i\sigma_1}{B+\tau_1\pi^2 i\sigma_1}\right), \end{aligned} \tag{3.11}$$

where

$$R_1 = \frac{R}{\pi^4}, \qquad T_{A_1} = \frac{T_A}{\pi^4}, \qquad x = \frac{a^2}{\pi^2}, \qquad i\sigma_1 = \frac{\sigma}{\pi^2}, \qquad P = \pi^2 P_l.$$

Equation (3.11) is a required dispersion relation accounting for the effect of suspended particles, medium permeability, variable gravity field, rotation on the stability of a Walters' (model B') viscoelastic fluid heated from below in a porous medium.

4. Stability of the system and oscillatory modes

Here we examine the possibility of oscillatory modes, if any, in a Walters' (model B') viscoelastic fluid due to the presence of suspended particles, rotation, viscoelasticity, and variable gravity field. Multiplying Eq. (3.5) by W^*, the complex conjugate of W, integrating over the range of z, and making use of Eqs. (3.6)–(3.7) with the help of the boundary conditions (3.9), we obtain:

$$\begin{aligned}(4.1)\quad &\left[\frac{\sigma}{\epsilon}\left(1+\frac{M}{1+\tau_1\sigma}\right)+\frac{1-F\sigma}{P_l}\right]I_1-\frac{\alpha a^2\lambda g_0\kappa}{\upsilon\beta}\left(\frac{1+\tau_1\sigma^*}{B+\tau_1\sigma^*}\right)\\ &\times\left(I_2+E_1p_1\sigma^* I_3\right)+d^2\left[\frac{\sigma^*}{\epsilon}\left(1+\frac{M}{1+\tau_1\sigma}\right)+\frac{1-F\sigma^*}{P_l}\right]I_4=0,\end{aligned}$$

where

$$I_1=\int_0^1\left(|DW|^2+a^2|W|^2\right)dz,\qquad I_2=\int_0^1\left(|D\Theta|^2+a^2|\Theta|^2\right)dz,$$

$$I_3=\int_0^1|\Theta|^2\,dz,\qquad I_4=\int_0^1|Z|^2\,dz.$$

The integral parts I_1–I_4 are all positive definite. Putting $\sigma=i\sigma_i$ in Eq. (4.1), where σ_i is real and equating the imaginary parts, we obtain:

$$\begin{aligned}(4.2)\quad &\sigma_i\left[\frac{1}{\epsilon}\left(1+\frac{M}{1+\tau_1^2\sigma_i^2}\right)-\frac{F}{P_l}\right]\left(I_1+d^2I_4\right)+\frac{\alpha a^2\lambda g_0\kappa}{\upsilon\beta}\\ &\cdot\left[\left(\frac{\tau_1(B-1)}{B^2+\tau_1^2\sigma_i^2}\right)I_2+\frac{B+\tau_1^2\sigma_i^2}{B^2+\tau_1^2\sigma_i^2}E_1p_1I_3\right]=0.\end{aligned}$$

Equation (4.2) implies that $\sigma_i=0$ or $\sigma_i\neq 0$, which means that modes may be non-oscillatory or oscillatory. The oscillatory modes are introduced due to the presence of rotation, gravity field, suspended particles, and viscoelasticity.

5. The stationary convection

For the stationary convection, putting $\sigma=0$ in Eq. (3.11) reduces it to:

$$(5.1)\qquad R_1=\frac{1+x}{\lambda xB}\left[\frac{1+x}{P}+\frac{T_{A_1}}{\epsilon^2}P\right],$$

which expresses the modified Rayleigh number R_1 as a function of the dimensionless wave number x and the parameters T_{A_1}, B, P; and then the Walters' (model B') viscoelastic fluid behaves like an ordinary Newtonian fluid, since the viscoelastic parameter F vanishes with σ.

To study the effects of suspended particles, rotation, and medium permeability, we examine the behavior of $\dfrac{dR_1}{dB}$, $\dfrac{dR_1}{dT_{A_1}}$, and $\dfrac{dR_1}{dP}$ analytically.

Equation (5.1) yields:

$$\frac{dR_1}{dB} = -\frac{1+x}{\lambda x B^2}\left[\frac{1+x}{P} + \frac{T_{A_1}}{\epsilon^2}P\right], \tag{5.2}$$

which is negative implying thereby that the effect of suspended particles is to destabilize the system when the gravity increases upwards from its value g_0 (i.e., $\lambda > 0$).

From Eq. (5.1), we also get:

$$\frac{dR_1}{dT_{A_1}} = \frac{1+x}{\lambda x B \epsilon^2}P, \tag{5.3}$$

which shows that rotation has a stabilizing effect on the system when the gravity increases upwards from its value g_0 (i.e., $\lambda > 0$).

It is evident from Eq. (5.1) that:

$$\frac{dR_1}{dP} = -\frac{1+x}{\lambda x B}\left[\frac{1+x}{P^2} - \frac{T_{A_1}}{\epsilon^2}\right]. \tag{5.4}$$

From Eq. (5.4), we observe that the medium permeability has a destabilizing effect when $\dfrac{1+x}{P^2} > \dfrac{T_{A_1}}{\epsilon^2}$, and it has a stabilizing effect when $\dfrac{1+x}{P^2} < \dfrac{T_{A_1}}{\epsilon^2}$, when the gravity increases upwards from its value g_0 (i.e., $\lambda > 0$).

In the absence of rotation and for a constant gravity field, $\dfrac{dR_1}{dP}$ is always negative implying thereby the destabilizing effect of the medium permeability.

The dispersion relation (5.1) is analyzed numerically. Graphs have been plotted by giving some numerical values to the parameters, to depict the stability characteristics.

In Fig. 1, Rayleigh number R_1 is plotted against suspended particles B for $\lambda = 2$, $T_{A_1} = 5$, $\epsilon = 0.5$, $P = 0.2$ for fixed wave numbers $x = 0.2$, $x = 0.5$, and $x = 0.8$. For the wave numbers $x = 0.2$, $x = 0.5$, and $x = 0.8$, suspended particles have a destabilizing effect.

In Fig. 2, Rayleigh number R_1 is plotted against rotation T_{A_1} for $B = 3$, $\lambda = 2$, $\epsilon = 0.5$, $P = 0.2$ for fixed wave numbers $x = 0.2$, $x = 0.5$, and $x = 0.8$. This shows that rotation has a stabilizing effect for fixed wave numbers $x = 0.2$, $x = 0.5$, and $x = 0.8$.

In Fig. 3, Rayleigh number R_1 is plotted against the medium permeability P for $B = 3$, $\lambda = 2$, $\epsilon = 0.5$, $T_{A_1} = 5$ for fixed wave numbers $x = 0.2$, $x = 0.5$, and $x = 0.8$. This shows that the medium permeability has a destabilizing effect for $P = 0.1$ to 0.3, and has a stabilizing effect for $P = 0.3$ to 1.0.

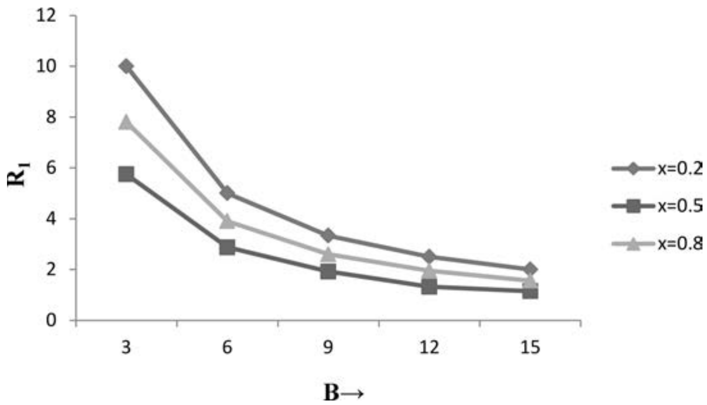

FIG. 1. Variation of Rayleigh number R_1 with suspended particles B for $\lambda = 2$, $T_{A_1} = 5$, $\epsilon = 0.5$, $P = 0.2$ for fixed wave numbers $x = 0.2$, $x = 0.5$, and $x = 0.8$.

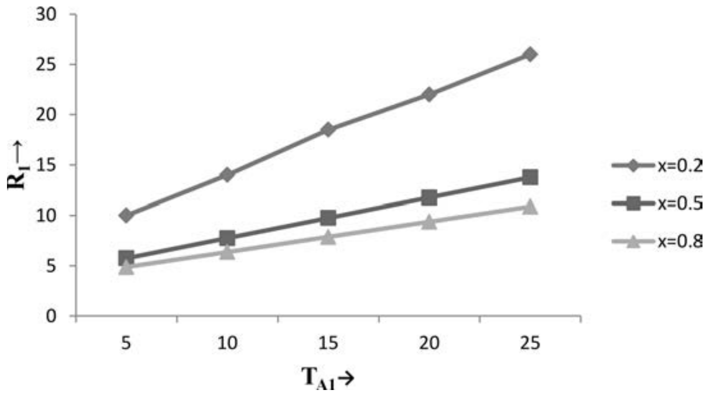

FIG. 2. Variation of Rayleigh number R_1 with rotation T_{A_1} for $B = 3$, $\lambda = 2$, $\epsilon = 0.5$, $P = 0.2$ for fixed wave numbers $x = 0.2$, $x = 0.5$, and $x = 0.8$.

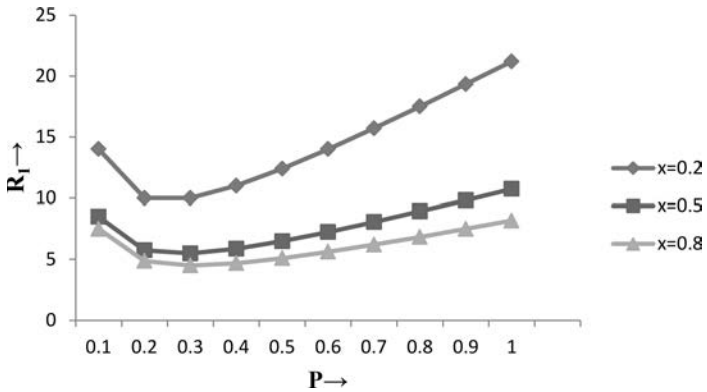

FIG. 3. Variation of Rayleigh number R_1 with the medium permeability P for $B = 3$, $\lambda = 2$, $\epsilon = 0.5$, $T_{A_1} = 5$ for fixed wave numbers $x = 0.2$, $x = 0.5$, and $x = 0.8$.

6. Conclusions

The effect of rotation and suspended particles on the stability of an incompressible Walters' (model B') fluid heated from below under a variable gravity field in a porous medium has been investigated. For the stationary convection, it has been found that the rotation has a stabilizing effect for $\lambda > 0$ and destabilizing effect for $\lambda < 0$, opposite to the Newtonian fluids. Suspended particles are found to have a destabilizing effect on the system as the gravity increases upwards from its value g_0 (i.e., for $\lambda > 0$) and a stabilizing effect as the gravity decreases upwards from its value g_0 (i.e., for $\lambda < 0$), whereas the medium permeability has a destabilizing/stabilizing effect on the system for $\frac{1+x}{P^2} > \frac{T_{A_1}}{\epsilon^2} \Big/ \frac{1+x}{P^2} < \frac{T_{A_1}}{\epsilon^2}$ as the gravity increases upwards from its value g_0 (i.e., for $\lambda > 0$). The presence of rotation, gravity field, suspended particles, and viscoelasticity introduces oscillatory modes. The effects of rotation, suspended particles, and medium permeability on thermal instability have also been shown graphically.

References

1. Chandrasekhar S., *Hydrodynamic and Hydromagnetic Stability*, Dover Publication, York, 1981.

2. Lapwood E.R., *Convection of a fluid in a porous medium*, Proc. Camb. Phil. Soc., **44**, 508–519, 1948.

3. Linden P.F., *Salt fingers in a steady shear flow*, Geophysics Fluid Dynamics, **6**, 1–27, 1974.

4. Lister C.R.B., *On the thermal balance of a mid ocean ridge*, Geophysics. J. Roy. Astr. Soc., **26**, 515–535, 1972.

5. Pradhan G.K., Samal P.C., *Thermal instability of a fluid layer under variable body forces*, J. Math. Anal. Appl., **122**, 487–498, 1987.

6. Rana G.C., Kango S.K., *Effect of rotation on thermal instability of compressible Walters' (model B') elastico-viscous fluid in porous medium*, JARAM, **3**, 44–57, 2011.

7. Scanlon J.W., Segel L.A., *Effect of suspended particles on onset of Be'nard convection*, Phys. Fluids, **16**, 1573–78, 1973.

8. Sharma R.C., *Thermal instability of viscoelastic fluid in hydromagnetics*, Acta Physica Hungarica, **38**, 293–298, 1975.

9. Sharma R.C., Sunil, *Thermal instability of an Oldroydian viscoelastic fluid with suspended particles in hydromagnetics in porous medium*, J. of Polymer Plastic Technology and Engineering, **33**, 323–339, 1994.

10. Sharma V., Rana G.C., *Thermal instability of a Walters' (model B') elastico-viscous fluid in the presence of variable gravity field and rotation in porous medium*, J. Non-Equilib. Thermodyn., **26**, 31–40, 2001.

11. Sharma V., Rana G.C., *Thermosolutal instability of a Walters' (model B') elastico-viscous rotating fluid in the presence of magnetic field and variable gravity field in porous medium*, Proc. Nat. Acad. Sci. INDIA, **73**, 93–111, 2003.

12. Sharma V., Gupta S., *Effect of rotation on thermal convection of micropolar fluids in the presence of suspended particles*, Arch. Mech., **60**, 403–419, 2008.

13. Stomel H., Fedorov K.N., *Small scale structure in temperature and salinity near Timor and Mindanao*, Tellus, **19**, 306–325, 1967.

14. Walters K., *The solution of flow problems in the case of materials with memory*, J. Mecanique, **1**, 469–778, 1962.

15. Wooding R.A., *Rayleigh instability of a thermal boundary layer in flow through a porous medium*, J. Fluid Mech., **9**, 183–192, 1960.

Received September 28, 2011.

ENGINEERING TRANSACTIONS • *Engng. Trans.* • **60**, 1, 69–96, 2012
Polish Academy of Sciences • Institute of Fundamental Technological Research (IPPT PAN)
National Engineering School of Metz (ENIM)
SIXTY YEARS OF THE ENGINEERING TRANSACTIONS

Selected Topics of High Speed Machining Analysis*)

Tomasz ŁODYGOWSKI[1)], Alexis RUSINEK[2)], Tomasz JANKOWIAK[1)], Wojciech SUMELKA[1)]

[1)] *Poznan University of Technology*
Faculty of Civil and Environmental Engineering
Institute of Structural Engineering
Piotrowo 5,60-965 Poznań, Poland
e-mail: {Tomasz.Lodygowski, Tomasz.Jankowiak, Wojciech.Sumelka}@put.poznan.pl

[2)] *National Engineering School of Metz (ENIM)*
Laboratory of Mechanics, Biomechanics, Polymers and Structures (LaBPS)
1 route d'Ars Laquenexy, 57000 Metz, France
e-mail: Rusinek@enim.fr

Some aspects of numerical analysis of problems related to high strain rates with thermal effects are considered. The attention is focused on constitutive modelling that describes the accompanied phenomena like plastic strain localization and softening. The importance of proper formulation of failure criteria is stressed. Also the complexity of computations is discussed.

Key words: high speed machining, numerical simulation, plasticity and softening.

1. Introduction

The high speed processes that generate rates of deformation of order 10^4–10^7 s^{-1} for ductile and brittle materials are still in focus of interests. There are crucial for those who work on constitutive modeling as well as computations. These two areas have to be carefully investigated. In particular, when we face the problems of softening due to fundamental thermal effects one can expect the difficulties connected with mathematical well posedness of the boundary value problems and in consequence the uniqueness of the obtained results. This effect appears when non-positive constitutive stiffness follows the overcoming of local peak in stress-strain space. In classical plasticity formulation the consequences of softening drive to lose of the type of the governing set of differential equa-

*)Initial lecture for VIII International Conference HIGH SPEED MACHINING, December 08-10, 2010, Metz, France.

tions and this requires a regularization. It can be done in different manner: 1) on the level of mathematical formulation of constitutive relations (rate dependent viscoplastic models, higher order gradient etc) or 2) on the level of numerical applications (introducing the localization zones into the approximation). Both those treatments we believe could be successful and the results for some particular cases are comparable with the real behavior of the matter, however only this which has the strong physical background should be acceptable.

2. Selected constitutive models

2.1. General remarks

The constitutive formulations which introduce the rate dependence have a chance for regularization of initial value problems and in consequence, after numerical discretization, can reproduce the behavior with a proper accuracy.

There are some main constitutive formulations commonly used which serve to describe the behavior of ductile materials including plastic strain localization and thermal softening. These constitutive models introduce implicitly or explicitly the internal length scale which plays the role of regularization parameter. These formulations will be discussed. The discussion will be focused on viscoplastic (eg. Perzyna's type) but also Rusinek–Klepaczko models which will be compared with commonly used and applied in numerical codes like Johnson-Cook one. Let stress that we focus our attention onto fast dynamic processes. The governing set of equations is of hyperbolic type until the softening effects are not present. The speed of the process is measured rather by the rate of stains than by the velocity of the movements. The process under consideration has to describe the strain localization followed by local fracture, development of cracks and finally the failure of the specimen.

2.2. Johnson-Cook model

Let us start with the well established constitutive model proposed by Johnson and Cook (JC) [5] and shortly remind the its well known properties. The JC model allows to take into account hardening, strain rate and temperature sensitivity. The explicit formulation of the JC model is defined as follows

$$\sigma(\varepsilon_{pl}, \dot{\varepsilon}_{pl}, T) = (A + B\varepsilon_{pl}^n)\left[1 + C\ln\left(\frac{\dot{\varepsilon}_{pl}}{\dot{\varepsilon}_0}\right)\right]\left[1 - \left(\frac{T - T_0}{T_{\mathrm{melt}} - T_0}\right)^m\right], \tag{2.1}$$

where A is a yield stress, B and n are strain hardening coefficients, C is a strain rate sensitivity coefficient and m describes the temperature sensitivity. To define the thermal softening of the material during dynamic loading, the heat equation is used. It allows to compute the temperature rise based on the quantity of plastic work converted into heat

$$\Delta T(\varepsilon, \dot{\varepsilon}) = \frac{\beta}{\rho C_p} \int\limits_{\varepsilon^e}^{\varepsilon^{\max}} \sigma d\varepsilon^{pl}, \tag{2.2}$$

where β is the Quinney–Taylor coefficient proportional to the quantity of plastic work converted into heat, ρ is a density of the material and C_p is a specific heat. Thus the current temperature T is defined as

$$T(\varepsilon^{pl}, \dot{\varepsilon}) = T_0 + \Delta T(\varepsilon^{pl}, \dot{\varepsilon}), \tag{2.3}$$

where T_0 is the initial temperature. So to describe any material (metal) one has to identify 5 constitutive parameters except of knowing its physical constants.

Because of its relative simplicity JC model is widely used in many engineering applications however in comparison with experiments it underestimates the results for very high strain rates. The constitutive model is implemented in Abaqus/Explicit environment and will be used for comparison with the other discussed models.

2.3. Rusinek–Klepaczko model

To describe the thermoviscoplastic behaviour of mild steel, an original constitutive relation has been used which couples hardening, temperature and strain rate sensitivity. However, it allows to take into account the non linearity in term of strain rate and temperature sensitivity. The equivalent stress $\sigma(\varepsilon^{pl}, \dot{\varepsilon}^{pl}, T)$ is an addition of two components, the internal stress $\sigma_\mu(\varepsilon^{pl}, \dot{\varepsilon}^{pl}, T)$ and the effective stress $\sigma^*(\dot{\varepsilon}^{pl}, T)$. The first one describes the hardening and the second one, the sensitivity and the reciprocity between strain rate and temperature. It base mainly on the Arrhenius equation. Due to the microstructure of the material, BCC, an additive decomposition is used, Eq. (2.4) allowing for a better description [7, 23, 28]

$$\sigma(\varepsilon^{pl}, \dot{\varepsilon}^{pl}, T) = \frac{E(T)}{E_0} \left[\sigma_\mu(\varepsilon^{pl}, \dot{\varepsilon}^{pl}, T) + \sigma^*(\dot{\varepsilon}^{pl}, T)\right], \tag{2.4}$$

where $E(T)$ is the Young's modulus depending on temperature and E_0 is the Young's modulus at $T = 0$ K.

The Young's modulus itself is defined as follows Eq. (2.5),

$$E(T) = E_0 \left\{1 - \frac{T}{T_m} \exp\left[\theta^* \left(1 - \frac{T_m}{T}\right)\right]\right\}, \tag{2.5}$$

where θ^* is a material constant depending of the microstructure. For ferritic steel $\theta^* = 0.59$ and for austenitic steel $\theta^* = 0.9$ as discussed in [26].

The explicit relations for the internal stresses $\sigma_\mu(\varepsilon^{pl}, \dot{\varepsilon}^{pl}, T)$ and the effective stresses $\sigma^*(\dot{\varepsilon}^{pl}, T)$ are the following, Eqs. (2.6) and (2.7)

$$\sigma_\mu(\varepsilon^{pl}, \dot{\varepsilon}^{pl}, T) = B(\dot{\varepsilon}^{pl}, T)(\varepsilon_0 + \varepsilon^{pl})^{n(\dot{\varepsilon}^{pl}, T)}, \tag{2.6}$$

$$\sigma^*(\dot{\varepsilon}^{pl}, T) = \sigma_0^* \left\langle 1 - D_1 \left(\frac{T}{T_m}\right) \log\left(\frac{\dot{\varepsilon}_{\max}}{\dot{\varepsilon}^{pl}}\right)\right\rangle^{m^*}, \tag{2.7}$$

where $B(\dot{\varepsilon}^{pl}, T)$ is the modulus of plasticity proportional to the yield stress and depends on strain rate and temperature. The exponent $n(\dot{\varepsilon}^{pl}, T)$ is the hardening coefficient which depends on strain rate and temperature and allows to define properly thermal softening during plastic deformation. D_1 is a material constant, T_m is the melting temperature, σ_0^* is a constant of the material, m^* is the strain rate sensitivity parameter. ε_0 is a material constant allowing to adjust the yield stress and $\dot{\varepsilon}_{\max} = 10^7\ \mathrm{s}^{-1}$ is the maximum strain rate allowed for model based on experiments.

The explicit expressions for $n(\dot{\varepsilon}^{pl}, T)$ and $B(\dot{\varepsilon}^{pl}, T)$ are defined by Eqs. (2.8) and (2.9)

$$n(\dot{\varepsilon}^{pl}, T) = n_0 \left\langle 1 - D_2 \left(\frac{T}{T_m}\right) \log\left(\frac{\dot{\varepsilon}^{pl}}{\dot{\varepsilon}_{\min}}\right)\right\rangle, \tag{2.8}$$

$$B(\dot{\varepsilon}^{pl}, T) = B_0 \left\langle \frac{T}{T_m} \log\left(\frac{\dot{\varepsilon}_{\max}}{\dot{\varepsilon}^{pl}}\right)\right\rangle^{-\nu_{CR}}, \tag{2.9}$$

where $\dot{\varepsilon}_{\min} = 10^{-5}\ \mathrm{s}^{-1}$ is the lower strain rate limit of the model, ν_{CR} is the temperature sensitivity coefficient, D_2, B_0 and n_0 are the constants for the material studied.

In addition, this model called RK has been developed originally with an algorithm allowing to define in a precise way all the constants of the model [7]. Therefore, the constants are independent of the user and the set of constants is unique for each material. The constants are defined step by step following physical restrictions. This model is used with success to describe the behaviour of different materials [24–26].

2.4. Perzyna's type viscoplasticity model

2.4.1. Introductory remarks

The material model is stated in the framework of the thermodynamical theory of viscoplasticity together with a phenomenological approach [4, 22, 32]. Formally, the constitutive structure belongs to the class of simple materials with fading memory. Due to its final form and the way of incorporating the fundamental variables, it also belongs to the class of rate dependent material with internal state variables [33]. Such an approach locates the model in the macro (meso-macro) space scale, thus all variables in the model reflect the homogenised reactions from smaller scales.

Let us shortly describe the key features of mathematical model for adiabatic process (for detailed and more general formulation see [31]). They are: (i) the description is invariant with respect to any diffeomorphism, (ii) the obtained evolution problem is well-posed, (iii) sensitivity to the rate of deformation, (iv) finite elasto-viscoplastic deformations, (v) plastic non-normality, (vi) dissipation effects, (vii) thermo-mechanical couplings and (viii) length scale sensitivity. It should be emphasised also that every variable in the model has a physical interpretation derived from analysis of single crystal and polycrystal behaviour.

In the discussed model, an important role plays the description of damage. We introduce the second order microdamage tensorial field (as a state variable), denoted by $\boldsymbol{\xi}$ cf. [4, 22, 31], which reflects the experimentally observed anisotropy of metals in the mathematical (constitutive) model. Such approach enables us to keep good global damage approximation (GDA) (strain-stress curves fitting from experiment and mathematical model) but especially good local damage approximation (LDA) (GDA plus coincidence in: macrodamage initiation time, velocity of macrodamage evolution and the geometry of macrodamage pattern). Let us emphasise that the Euclidean norm of the microdamage field defines the scalar quantity called the *volume fraction porosity* or simply *porosity* [22] while its principal values are proportional to the ratio of the damaged area to the assumed characteristic area of the representative volume element [31], thus they indicate damage plane as one perpendicular to maximal principal value of $\boldsymbol{\xi}$ (cf. Fig. 1).

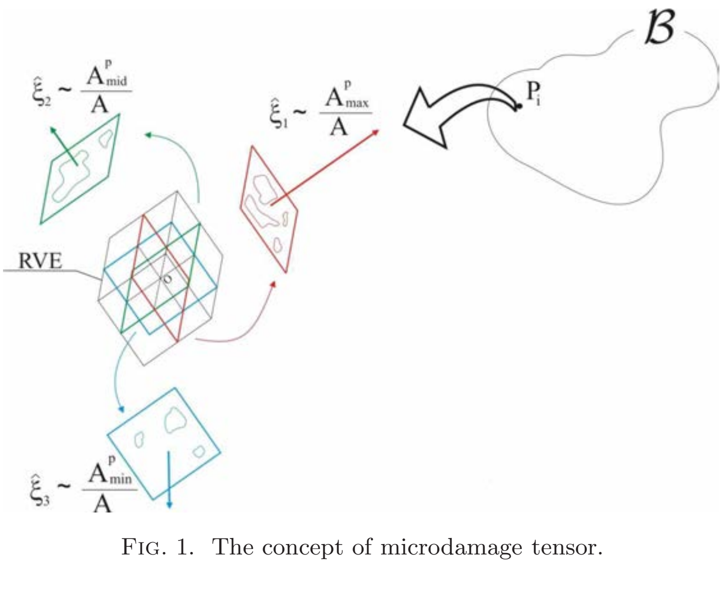

FIG. 1. The concept of microdamage tensor.

2.4.2. Adiabatic process

Kinematics. The abstract body is a differential manifold. The kinematics of the finite elasto-viscoplastic deformations is governed by the multiplicative decomposition of the total deformation gradient to the elastic and viscoplastic parts [8]

$$\mathbf{F}(\mathbf{X},t) = \mathbf{F}^e(\mathbf{X},t)\cdot\mathbf{F}^p(\mathbf{X},t), \tag{2.10}$$

where $\mathbf{F} = \dfrac{\partial\phi(\mathbf{X},t)}{\partial\mathbf{X}}$ is the deformation gradient, ϕ describes the motion, $\mathbf{X}$ denotes material coordinates, t is time and $\mathbf{F}^e$, $\mathbf{F}^p$ are elastic and viscoplastic parts, respectively.

From the spatial deformation gradient, denoted by $\mathbf{l}$,

$$\mathbf{l}(\mathbf{x},t) = \frac{\partial\boldsymbol{\upsilon}(\mathbf{x},t)}{\partial\mathbf{x}}, \tag{2.11}$$

where $\boldsymbol{\upsilon}$ denotes spatial velocity and $\mathbf{x}$ are spatial coordinates, we obtain

$$\mathbf{l} = \mathbf{d} + \mathbf{w} = \mathbf{d}^e + \mathbf{w}^e + \mathbf{d}^p + \mathbf{w}^p, \tag{2.12}$$

$$\mathbf{d} = \frac{1}{2}(\mathbf{l} + \mathbf{l}^T), \tag{2.13}$$

$$\mathbf{w} = \frac{1}{2}(\mathbf{l} - \mathbf{l}^T), \tag{2.14}$$

where $\mathbf{d}$ is the symmetric part and $\mathbf{w}$ is the antisymmetric part, of $\mathbf{l}$, respectively. Now, assuming that the Euler–Almansi strain is taken as a strain measure and applying Lie derivative we have the fundamental relation

$$\mathbf{d}^\flat = \mathrm{L}_{\boldsymbol{\upsilon}}(\mathbf{e}^\flat), \tag{2.15}$$

and simultaneously

$$\mathbf{d}^{e\flat} = \mathrm{L}_{\boldsymbol{\upsilon}}(\mathbf{e}^{e\flat}), \qquad \mathbf{d}^{p\flat} = \mathrm{L}_{\boldsymbol{\upsilon}}(\mathbf{e}^{p\flat}), \tag{2.16}$$

where $\mathrm{L}_{\boldsymbol{\upsilon}}$ stands for Lie derivative, $\mathbf{e}$ for the Euler–Almansi strain and $\flat$ indicates the tensor that has all its indices lowered. These relations show that the symmetric part of spatial deformation gradient $\mathbf{d}$ is directly Lie derivative of the Euler–Almansi strain.

Constitutive postulates [19]. Assuming that the balance principles hold: conservation of mass, balance of momentum, balance of moment of momentum and balance of energy and entropy production, we define four constitutive postulates [21]:

(i) Existence of the free energy function ψ. Formally we apply it in the following form

$$\psi = \widehat{\psi}(\mathbf{e}, \mathbf{F}, \vartheta; \boldsymbol{\mu}), \tag{2.17}$$

where $\boldsymbol{\mu}$ denotes a set of internal state variables governing the description of dissipation effects and ϑ denotes temperature.

(ii) Axiom of objectivity (spatial covariance). The material model should be invariant with respect to any superposed motion (diffeomorphism).

(iii) The axiom of the entropy production. For every regular process the constitutive functions should satisfy the second law of thermodynamics.

(iv) The evolution equation for the internal state variables vector $\boldsymbol{\mu}$ should be of the form

$$\mathrm{L}_{\boldsymbol{\upsilon}}\boldsymbol{\mu} = \widehat{\mathbf{m}}(\mathbf{e}, \mathbf{F}, \vartheta, \boldsymbol{\mu}), \tag{2.18}$$

where evolution function $\widehat{\mathbf{m}}$ has to be determined based on the experimental observations.

Initial boundary value problem. Under the above conditions the deforming body under adiabatic regime is governed by the following set of equations. They state the initial boundary value problem (IBVP).

Find ϕ, $\boldsymbol{\upsilon}$, ρ, $\boldsymbol{\tau}$, $\boldsymbol{\xi}$, ϑ as functions of t and position $\mathbf{x}$ such that [9, 11, 12, 20]:

(i) the field equations

$$\begin{aligned}
&\dot{\phi} = \boldsymbol{\upsilon},\\
&\dot{\boldsymbol{\upsilon}} = \frac{1}{\rho_{\mathrm{Ref}}}\left(\mathrm{div}\boldsymbol{\tau} + \frac{\boldsymbol{\tau}}{\rho}\cdot \mathrm{grad}\rho - \frac{\boldsymbol{\tau}}{1-(\boldsymbol{\xi}:\boldsymbol{\xi})^{1/2}}\mathrm{grad}(\boldsymbol{\xi}:\boldsymbol{\xi})^{1/2}\right),\\
&\dot{\rho} = -\rho\mathrm{div}\boldsymbol{\upsilon} + \frac{\rho}{1-(\boldsymbol{\xi}:\boldsymbol{\xi})^{1/2}}(\mathrm{L}_{\boldsymbol{\upsilon}}\boldsymbol{\xi}:\mathrm{L}_{\boldsymbol{\upsilon}}\boldsymbol{\xi})^{1/2},\\
&\dot{\boldsymbol{\tau}} = \mathcal{L}^e:\mathbf{d} + 2\boldsymbol{\tau}\cdot\mathbf{d} - \mathcal{L}^{th}\dot{\vartheta} - (\mathcal{L}^e + \mathbf{g}\boldsymbol{\tau} + \boldsymbol{\tau}\mathbf{g}):\mathbf{d}^p,\\
&\dot{\boldsymbol{\xi}} = 2\boldsymbol{\xi}\cdot\mathbf{d} + \frac{\partial g^*}{\partial\boldsymbol{\tau}}\frac{1}{T_m}\left\langle \Phi^g\left[\frac{I_g}{\tau_{eq}(\boldsymbol{\xi},\vartheta,\in^p)} - 1\right]\right\rangle,\\
&\dot{\vartheta} = \frac{\chi^*}{\rho c_p}\boldsymbol{\tau}:\mathbf{d}^p + \frac{\chi^{**}}{\rho c_p}\mathbf{k}:\mathrm{L}_{\boldsymbol{\upsilon}}\boldsymbol{\xi},
\end{aligned} \tag{2.19}$$

(ii) the boundary conditions

(a) displacement ϕ is prescribed on a part Γ_ϕ of $\Gamma(\mathcal{B})$ and tractions $(\boldsymbol{\tau}\cdot\mathbf{n})^a$ are prescribed on a part $\Gamma_{\boldsymbol{\tau}}$ of $\Gamma(\mathcal{B})$, where $\Gamma_\phi \cap \Gamma_{\boldsymbol{\tau}} = 0$ and $\Gamma_\phi \cup \Gamma_{\boldsymbol{\tau}} = \Gamma(\mathcal{B})$,

(b) heat flux $\mathbf{q}\cdot\mathbf{n} = 0$ is prescribed on $\Gamma(\mathcal{B})$,

(iii) the initial conditions $\phi, \boldsymbol{\upsilon}, \rho, \boldsymbol{\tau}, \boldsymbol{\xi}, \vartheta$ are given for each particle $\mathbf{X} \in \mathcal{B}$ at $t = 0$,

are satisfied. In above, we have denoted: ρ_{Ref} as a referential density, $\boldsymbol{\tau}$ as the Kirchhoff stress tensor, ρ as a current density, $\mathcal{L}^e$ as an elastic constitutive tensor, $\mathcal{L}^{th}$ as a thermal operator, $\mathbf{g}$ as a metric tensor, $\partial g^*/\partial\boldsymbol{\tau}$ as the evolution directions for anisotropic microdamage growth processes, T_m as a relaxation time of mechanical disturbances, I_g as a stress intensity invariant, τ_{eq} as the threshold stress, χ^*, χ^{**} as the irreversibility coefficients and c_p as a specific heat.

Material functions. For the evolution problem (2.19) we assume the following:

1. For elastic constitutive tensor $\mathcal{L}^e$

$$\mathcal{L}^e = 2\mu\mathcal{I} + \lambda(\mathbf{g}\otimes\mathbf{g}), \tag{2.20}$$

where μ, λ are Lamé constants.

2. For thermal operator $\mathcal{L}^{th}$

$$\mathcal{L}^{th} = (2\mu + 3\lambda)\theta\mathbf{g}, \tag{2.21}$$

where θ is thermal expansion coefficient.

3. For viscoplastic flow phenomenon $\mathbf{d}^p$ [16, 17]

$$\mathbf{d}^p = \Lambda^{vp}\mathbf{p}, \tag{2.22}$$

where

$$\Lambda^{vp} = \frac{1}{T_m}\left\langle \Phi^{vp}\left(\frac{f}{\kappa} - 1\right)\right\rangle = \frac{1}{T_m}\left\langle \left(\frac{f}{\kappa} - 1\right)^{m_{pl}}\right\rangle, \tag{2.23}$$

$$f = \left\{J_2' + \left[n_1(\vartheta) + n_2(\vartheta)(\boldsymbol{\xi}:\boldsymbol{\xi})^{1/2}\right]J_1^2\right\}^{1/2}, \tag{2.24}$$

$$n_1(\vartheta) = 0, \qquad n_2(\vartheta) = n = \mathrm{const.}, \tag{2.25}$$

$$\kappa = \{\kappa_s(\vartheta) - [\kappa_s(\vartheta) - \kappa_0(\vartheta)] \exp[-\delta(\vartheta) \in^p]\} \cdot \left[1 - \left(\frac{(\boldsymbol{\xi} : \boldsymbol{\xi})^{1/2}}{\xi_F}\right)^{\beta(\vartheta)}\right], \tag{2.26}$$

$$\begin{gathered} \overline{\vartheta} = \frac{\vartheta - \vartheta_0}{\vartheta_0}, \qquad \kappa_s(\vartheta) = \kappa_s^* - \kappa_s^{**}\overline{\vartheta}, \qquad \kappa_0(\vartheta) = \kappa_0^* - \kappa_0^{**}\overline{\vartheta}, \\ \delta(\vartheta) = \delta^* - \delta^{**}\overline{\vartheta}, \qquad \beta(\vartheta) = \beta^* - \beta^{**}\overline{\vartheta}, \end{gathered} \tag{2.27}$$

$$\xi^F = \xi^{F*} - \xi^{F**} \left\langle \left(\frac{\|\mathrm{L}_{\boldsymbol{\upsilon}}\boldsymbol{\xi}\| - \|\mathrm{L}_{\boldsymbol{\upsilon}}\boldsymbol{\xi}_c\|}{\|\mathrm{L}_{\boldsymbol{\upsilon}}\boldsymbol{\xi}_c\|} \right)^{m_F} \right\rangle, \tag{2.28}$$

$$\mathbf{p} = \left.\frac{\partial f}{\partial \boldsymbol{\tau}}\right|_{\boldsymbol{\xi}=\mathrm{const}} \left(\left\| \frac{\partial f}{\partial \boldsymbol{\tau}} \right\| \right)^{-1} = \frac{1}{[2J_2' + 3A^2(\mathrm{tr}\boldsymbol{\tau})^2]^{1/2}} [\boldsymbol{\tau}' + A\mathrm{tr}\boldsymbol{\tau}\boldsymbol{\delta}], \tag{2.29}$$

and f denotes the potential function [4, 18, 19, 29], κ is the isotropic work–hardening–softening function [15, 19], $\boldsymbol{\tau}'$ represents stress deviator, J_1, J_2' are the first and the second invariants of Kirchhoff stress tensor and deviatoric part of the Kirchhoff stress tensor, respectively, $A = 2(n_1 + n_2(\boldsymbol{\xi} : \boldsymbol{\xi})^{1/2})$, ξ^{F*} can be thought as a quasi-static fracture porosity and $\|\mathrm{L}_{\boldsymbol{\upsilon}}\boldsymbol{\xi}_c\|$ denotes equivalent critical velocity of microdamage. Notice, that Eq. (2.28) reflects experimental fact, that the fracture porosity changes for fast processes. Such an approach is consistent with the, so called, cumulative fracture criterion [2, 6], which assumes the existence of critical time needed for saturation of microdamage to its fracture limit.

4. For microdamage mechanism we take the additional assumptions [3, 4]:
   - increment of the microdamage state is coaxial with the principal directions of stress state,
   - only positive (tension) principal stresses induces the growth of the microdamage,

   we have

$$\frac{\partial g^*}{\partial \boldsymbol{\tau}} = \left\langle \frac{\partial \widehat{g}}{\partial \boldsymbol{\tau}} \right\rangle \left\| \left\langle \frac{\partial \widehat{g}}{\partial \boldsymbol{\tau}} \right\rangle \right\|^{-1}, \qquad \text{and} \qquad \widehat{g} = \frac{1}{2}\boldsymbol{\tau} : \mathcal{G} : \boldsymbol{\tau}, \tag{2.30}$$

$$\Phi^g \left(\frac{I_g}{\tau_{eq}(\boldsymbol{\xi}, \vartheta, \in^p)} - 1 \right) = \left(\frac{I_g}{\tau_{eq}} - 1 \right)^{m_g}, \tag{2.31}$$

where

$$\tau_{eq} = c(\vartheta)(1 - (\boldsymbol{\xi} : \boldsymbol{\xi})^{1/2}) \ln \frac{1}{(\boldsymbol{\xi} : \boldsymbol{\xi})^{1/2}} \cdot \{2\kappa_s(\vartheta) - [\kappa_s(\vartheta) - \kappa_0(\vartheta)] F(\xi_0, \boldsymbol{\xi}, \vartheta)\}, \qquad c(\vartheta) = \mathrm{const.}, \tag{2.32}$$

(2.33) $$F = \left(\frac{\xi_0}{1-\xi_0} \frac{1-(\boldsymbol{\xi}:\boldsymbol{\xi})^{1/2}}{(\boldsymbol{\xi}:\boldsymbol{\xi})^{1/2}} \right)^{\frac{2}{3}\delta} + \left(\frac{1-(\boldsymbol{\xi}:\boldsymbol{\xi})^{1/2}}{1-\xi_0} \right)^{\frac{2}{3}\delta},$$

and

(2.34) $$I_g = \overline{b}_1 J_1 + \overline{b}_2 (J_2^{'})^{1/2} + \overline{b}_3 (J_3^{'})^{1/3}.$$

$\overline{b}_i$ $(i = 1,2,3)$ are the material parameters, $J_3^{'}$ is the third invariant of deviatoric part of the Kirchhoff stress tensor.

Now, taking into account the postulates for microdamage evolution, and assuming that tensor $\mathcal{G}$ can be written as a symmetric part of the fourth order unity tensor $\mathcal{I}$ [10]

(2.35) $$\mathcal{G} = \mathcal{I}^s, \qquad \mathcal{G}_{ijkl} = \frac{1}{2}\left(\delta_{ik}\delta_{jl} + \delta_{il}\delta_{jk}\right),$$

we can write the explicit form of the growth function $\widehat{g}$ as

(2.36) $$\widehat{g} = \frac{1}{2}\left(\tau_I^2 + \tau_{II}^2 + \tau_{III}^2\right).$$

The gradient of $\widehat{g}$ with respect to the stress field gives us the following matrix representation of a tensor describing the anisotropic evolution of microdamage

(2.37) $$\frac{\partial \widehat{g}}{\partial \boldsymbol{\tau}} = \begin{bmatrix} g_{11}\tau_I & 0 & 0 \\ 0 & g_{22}\tau_{II} & 0 \\ 0 & 0 & g_{33}\tau_{III} \end{bmatrix}.$$

In (2.37) $\tau_I, \tau_{II}, \tau_{III}$ are the principal values of Kirchhoff stress tensor.

It can be noted, that the definition of the threshold stress for microcrack growth function τ_{eq} indicates that the growth term in evolution function for microdamage is active only after nucleation whereas before nucleation we have infinite threshold $\lim_{\boldsymbol{\xi}\to\mathbf{0}} \tau_{eq} = \infty$.

5. For temperature evolution Eq. (2.19) we consider the following relation

(2.38) $$\mathbf{k} = \boldsymbol{\tau}.$$

3. Numerical aspects and some examples

The main purpose of the HSM modeling and computations is to estimate properly the forces that act in the cutting machine tools. It helps to design the elements of HSM-machines. For description of the material itself and particularly its thermo-plastic behaviour we use the constitutive relations of different order of complexity. More or less these properties combines the physical observation with mathematical elegance. One of the fundamental problem is to estimate properly (identify) the constitutive parameters placed in the mathematical structure. This could be the topic of a separate study. So, let us allow to use the set of parameters which describe the same mild steel for three used formulations (JC, RK, Perzyna models). We will show the results obtained for different speed of machining and different friction coefficient between specimen and the tool. The other numerical aspects also will be stressed.

3.1. *Orthogonal cutting – geometry, boundary and initial conditions*

The analysed HSM set up is presented in Fig. 2. The tool is rigid and its geometry is described be an exterior angle equal 7° and the fillet radius equal 3 μm. The dimensions of the machined sample (3D) are length 2000 μm, height 200 μm and out of plane thickness 5 μm.

The boundary conditions on a sample are applied at the bottom, front and rear surfaces, while rigid tool can move in horizontal direction only with constant velocity 12 ms^{-1}. The initial conditions assume room temperature.

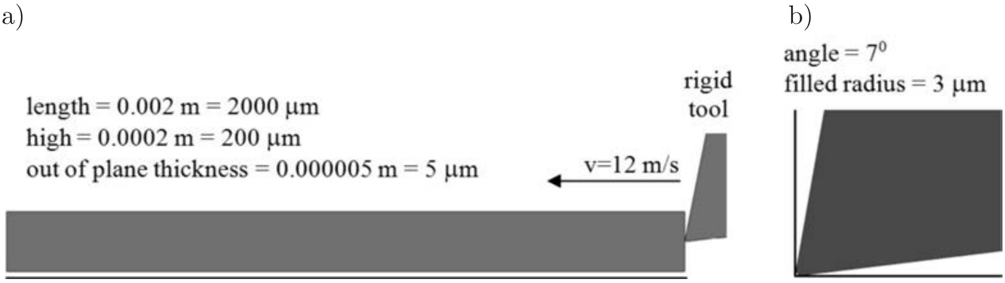

Fig. 2. a) Configuration of the High Speed Machining; b) Geometry of the rigid tool.

3.2. *Material models implementation*

The discussed material models are all implemented in Abaqus/Explicit commercial finite element code. While Johnson–Cook model is pre-implemented in Abaqus/Explicit code, the two other, namely Rusinek–Klepaczko and Perzyna's viscoplasticity models are added to the software by taking advantage of a user subroutine VUMAT, which is coupled with Abaqus system [1]. Let us mention that the Abaqus/Explicit utilises central-difference time integration rule along with the diagonal ("lumped") element mass matrices. The details concerning implementation of Rusinek–Klepaczko and Perzyna's viscoplasticity models as Abaqus subroutine VUMAT can be found in [27, 34] and [31], respectively.

3.3. *Material parameters for ES mild steel*

The material parameters for the ES mild steel for Johnson–Cook, Rusinek–Klepaczko and Perzyna's viscoplasticity type models are collected in Tables 1–3, respectively.

Table 1. Material parameters for ES mild steel – Johnson–Cook model.

$T_{\mathrm{melt}} = 1600$ K	$\beta = 0.9$	$\rho = 7800$ kg/m^3	$C_p = 470$ J/kgK
$\alpha = 10^{-5}$ K^{-1}	$E = 210$ GPa	$\nu = 0.3$	$A = 57.27$ MPa
$B = 479.93$ MPa	$n = 0.316$	$C = 0.0362$	$\dot{\varepsilon_0} = 0.001$ 1/s
$T_0 = 300$ K	$m = 0.28$		

Table 2. Material parameters for ES mild steel – Rusinek–Klepaczko model.

$T_m = 1600$ K	$\beta = 0.9$	$\rho = 7800$ kg/m^3	$C_p = 470$ J/kgK
$\alpha = 10^{-5}$ K^{-1}	$E_0 = 210$ GPa	$\nu = 0.3$	$\theta^* = 0.59$
$T_0 = 300$ K	$B_0 = 591.6$ MPa	$n_0 = 0.285$	$\varepsilon_0 = 0.018$
$D_1 = 0.48$	$\nu_{CR} = 0.2$	$\sigma_0^* = 406.3$ MPa	$m^* = 2.8$
$D_2 = 0.19$			

Table 3. Material parameters for ES mild steel – Perzyna's type viscoplasticity model.

$\lambda = 121.154$ GPa	$\mu = 80.769$ GPa	$\rho_{\mathrm{Ref}} = 7800$ kg/m^3	$m_g = 1$
$c = 0.067$	$b_1 = 0.02$	$b_2 = 0.5$	$b_3 = 0$
$\xi^{F^*} = 0.36$	$\xi^{F^{**}} = 0$	m_F –	$\Vert \mathrm{L}_{\upsilon}\boldsymbol{\xi}_c \Vert$ – s^{-1}
$\delta^* = 6.0$	$\delta^{**} = 1.4$	$T_m = 2.5$ µs	$m_{pl} = 0.14$
$\kappa_s^* = 430$ MPa	$\kappa_s^{**} = 97$ MPa	$\kappa_0^* = 317$ MPa	$\kappa_0^{**} = 71$ MPa
$\beta^* = 11.0$	$\beta^{**} = 2.5$	$n_1 = 0$	$n_2 = 0.25$
$\chi^* = 0.8$	$\chi^{**} = 0.1$	$\theta = 10^{-5}$ K^{-1}	$c_p = 470$ J/kgK

3.4. *Numerical results*

Johnson–Cook model

Plane stress versus plane stress conditions

During the orthogonal cutting (HSM) three dimensional block (volume) is cut and for simulation of this process the solid elements are used together with proper description of boundary conditions to assure the plane strain conditions. We do not use directly plane strain elements because for 3D cases the general contact algorithm is more efficient.

It is the reason that in our simulations we have only one layer of finite elements with out of plane thickness 5 μm. For this thickness and for element size 10 μm in plane XY we present the distribution of equivalent stresses for two conditions (plane strain and plain stress), Fig. 3.

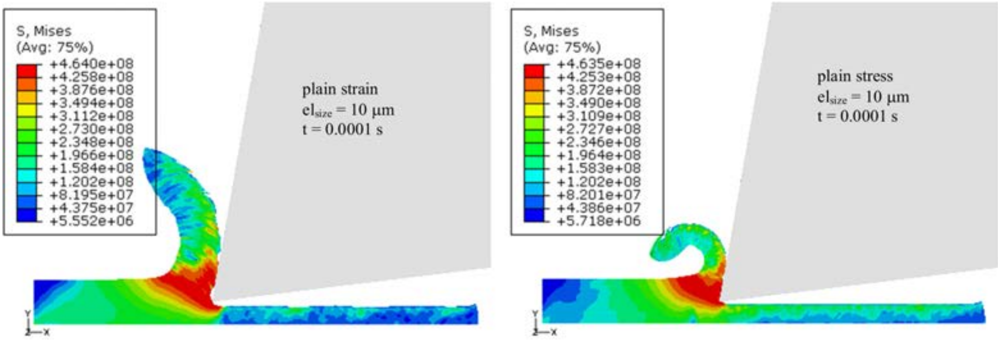

Fig. 3. The maps of equivalent stresses for plain stress and plane strain cases; element size is 10 μm.

The state of deformation presented in Fig. 3 for two cases shows that more real formation of chip is using plane strain condition [13, 30]. For plane stress condition the large influence is played by the strain tensor component perpendicular to the plane XY. It leads to fast failure of the material (the chip is very thin). The force which acts on the tool during cutting process is similar in both considered cases. The average forces are 0.45 N for both cases for 5 μm thickness of the model. The force is proportional to the thickness and for example if the thickness is 1000 μm (1 mm) the cutting force is equal to 90 N (0.45 N · 1000 μm/5 μm).

Finite elements size

Previous simulations and analyzes lead to the conclusion that in the case of orthogonal cutting (HSM) the plane strain condition should be used (all nodes of the cut material have blocked displacement U3). The important aspect of numerical modelling with strain and strain rate hardening but with temperature softening (adiabatic condition), is the description of the mesh size dependency that proofs the well-possedness of the IBVP. It is presented in this section.

The maps of equivalent stresses and strains for different element sizes: 20 μ m, 15 μm, 10 μm are presented in Fig. 4. The used FE meshes are shown above the HMH stresses maps. The average cutting forces for one layer of finite elements (5 μm) are of order 0.7 N, 0.5 N and 0.45 N. The important is also that for larger finite elements the higher fluctuations are obtained, see Fig. 5. In the next simulations we will use the smallest finite elements size (10 μm). The real localization zones in the described processes are approximately of the dimensions of the smallest used elements (10 μm).

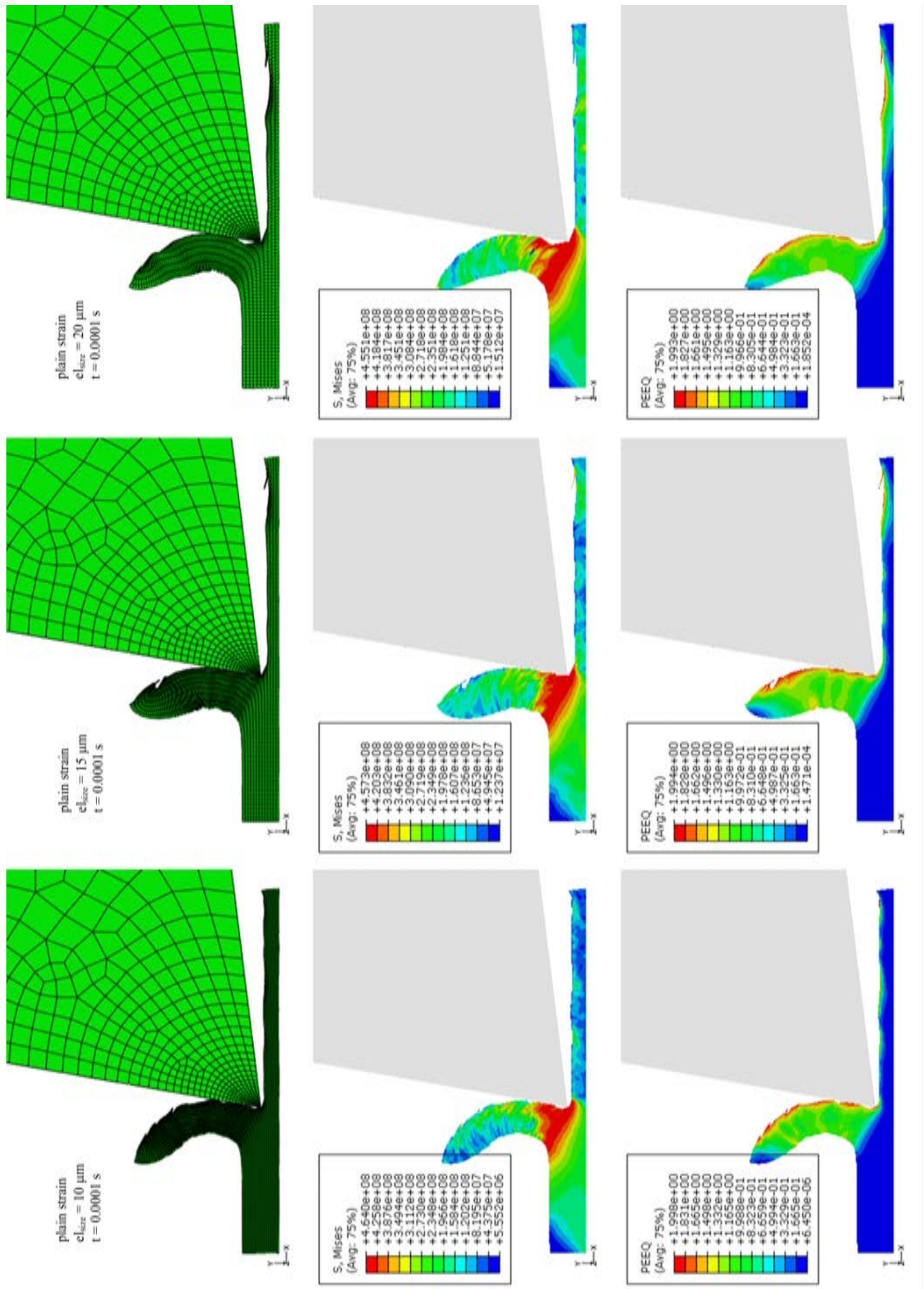

FIG. 4. The equivalent stresses and strains maps for different element size: 10 µm, 15 µm, 20 µm.

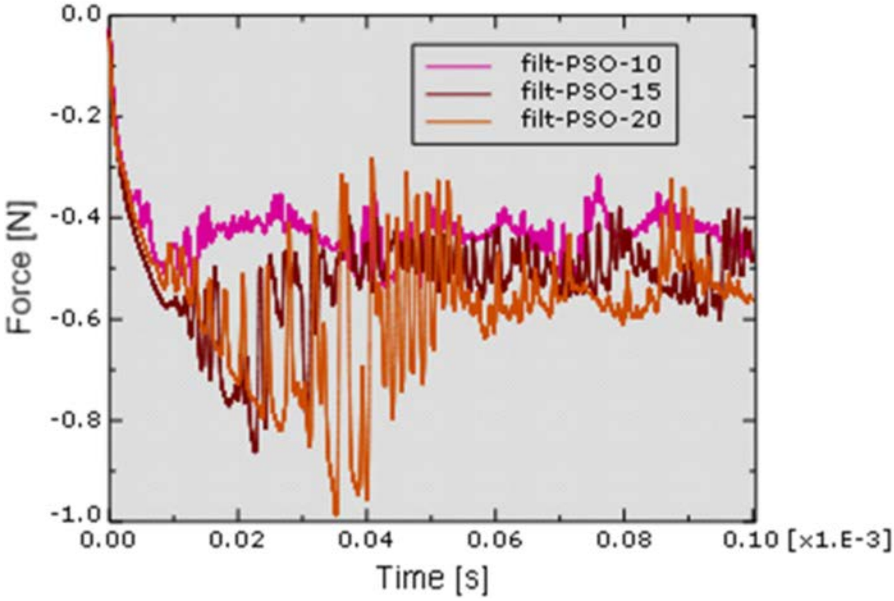

Fig. 5. The cutting force for different element sizes.

Friction

The influence of friction coefficient is significant. Figure 6 present the maps of the equivalent stresses, strains and temperatures for different friction coefficients (0.3, 0.1). We can observe the deformation and chip formation processes. For smaller friction coefficient the chip behaves in more ductile way, however the maximal temperature and plastic deformation are of the same order. The maximum value of stresses, strains and temperatures are close for two considered cases. The cutting force is smaller for friction coefficient 0.1 (0.4 N) than for friction coefficient 0.3 (0.45 N).

Rectangle versus triangle finite elements

It is well known that the different shapes of the elements can introduce to the IBVP a kind of numerical anisotropy (dispersion effect). The most cases this drives to uncorrected estimation of the localization zones. In this section the influence of alignment for two types of finite elements (rectangle and triangle) is presented. The density of finite elements is similar ($el_{size} = 10$ μm) in both cases and only element type (el_{type}) is different.

The deformation of the models is different. In model with the triangle elements the partitioning of the chip is clearly visible while visible using rectangle finite element the chip is continuous. Additionally, the cutting forces were compared and in case of triangle elements the average force is about 0.7 N (for el_{type} = rectangle it is 0.45 N).

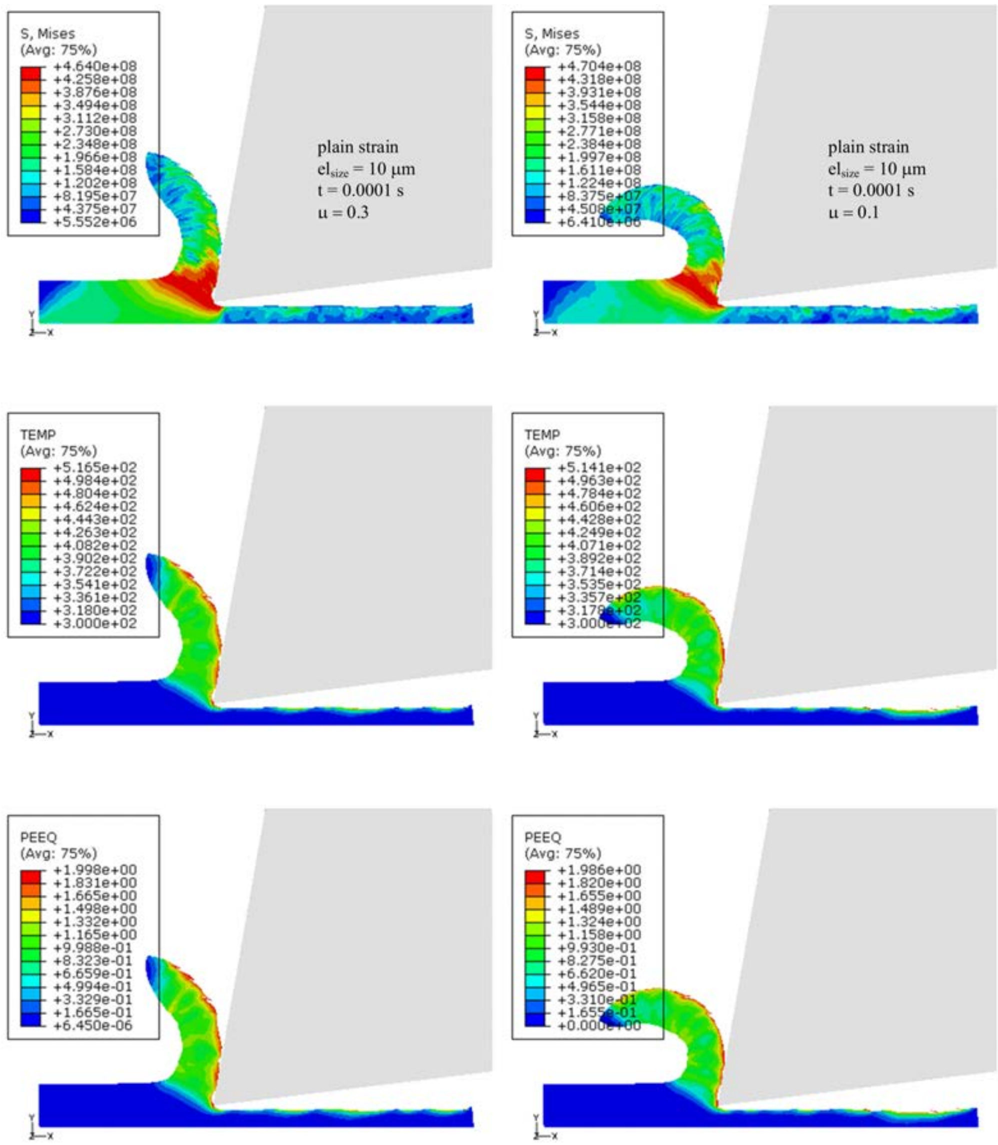

FIG. 6. The maps of equivalent stresses, temperatures and strains for two friction coefficients: 0.3 and 0.1 for fixed element size 10 μm.

The different effects in JC modelling

The next considered aspect is the influence of constitutive parameters on failure mode and chip formation. Four cases were taken into account, see Fig. 8. In Fig. 8a the all effects are included it means, strain hardening, strain rate hardening and temperature softening. The results (Fig. 8a) are presented also in Fig. 6a and Fig. 7a. In Fig. 8b, the yield stress is independent of strains,

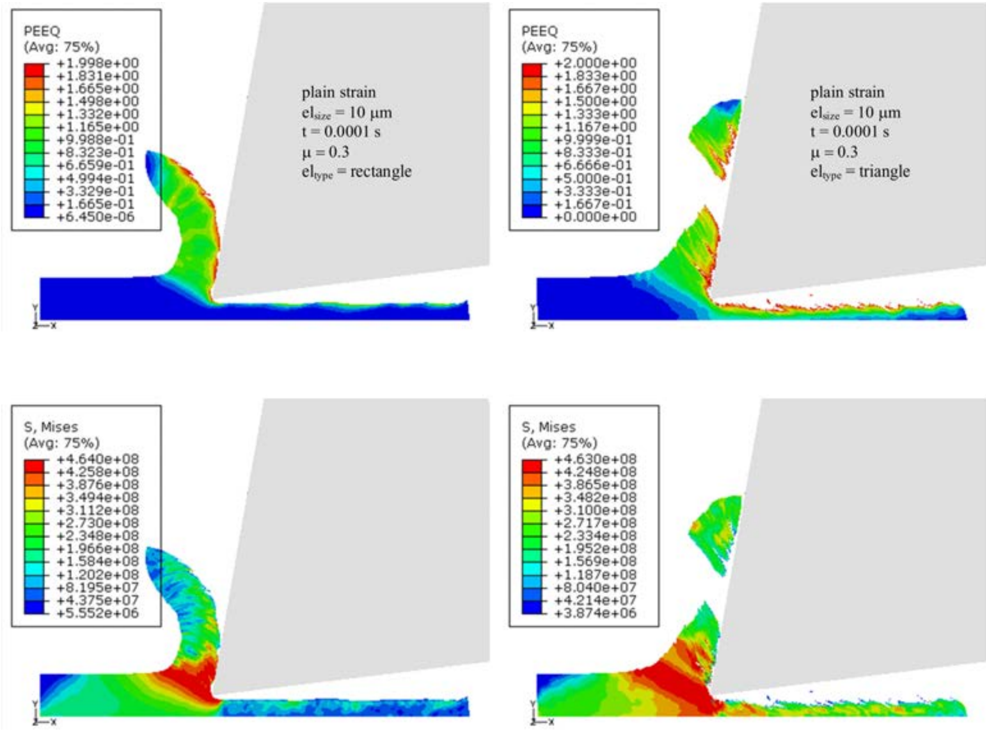

Fig. 7. The maps of equivalent plastic strains, stresses, for two mesh alignments.

strain rates and temperatures. The Fig. 8c presents the situation where yield stress depends only on strain. The last map of equivalent strains presents the case where yield stress is a function of strain (hardening) and temperature (softening), see Fig. 8d. In Fig. 8e the plot of cutting forces for all cases is presented. In case A the average cutting force is 0.45 N, for case B it is only 0.07 N, for case C the cutting force is 0.6 N but for case D it is 0.3 N. The results show the effects of taking into consideration some parts of Eq. (2.1) into JC model and also using the simplifications.

The depth of cut

As the last effect in this section the depth of the cut is discussed. Previous results took into account only one depth (100 μm). Now we present the results for the other depth cut equal (50 μm). The comparison of the obtained results is presented in Fig. 9. In Fig. 9c one can observe the history of the cutting force for two depths of cut. The force varies in time but the average cutting force for cut depth 100 μm is 0.45 N and for 50 μm is 0.27 N. These results are also in agreement with other reported simulations and with laboratory test for other materials [13, 30].

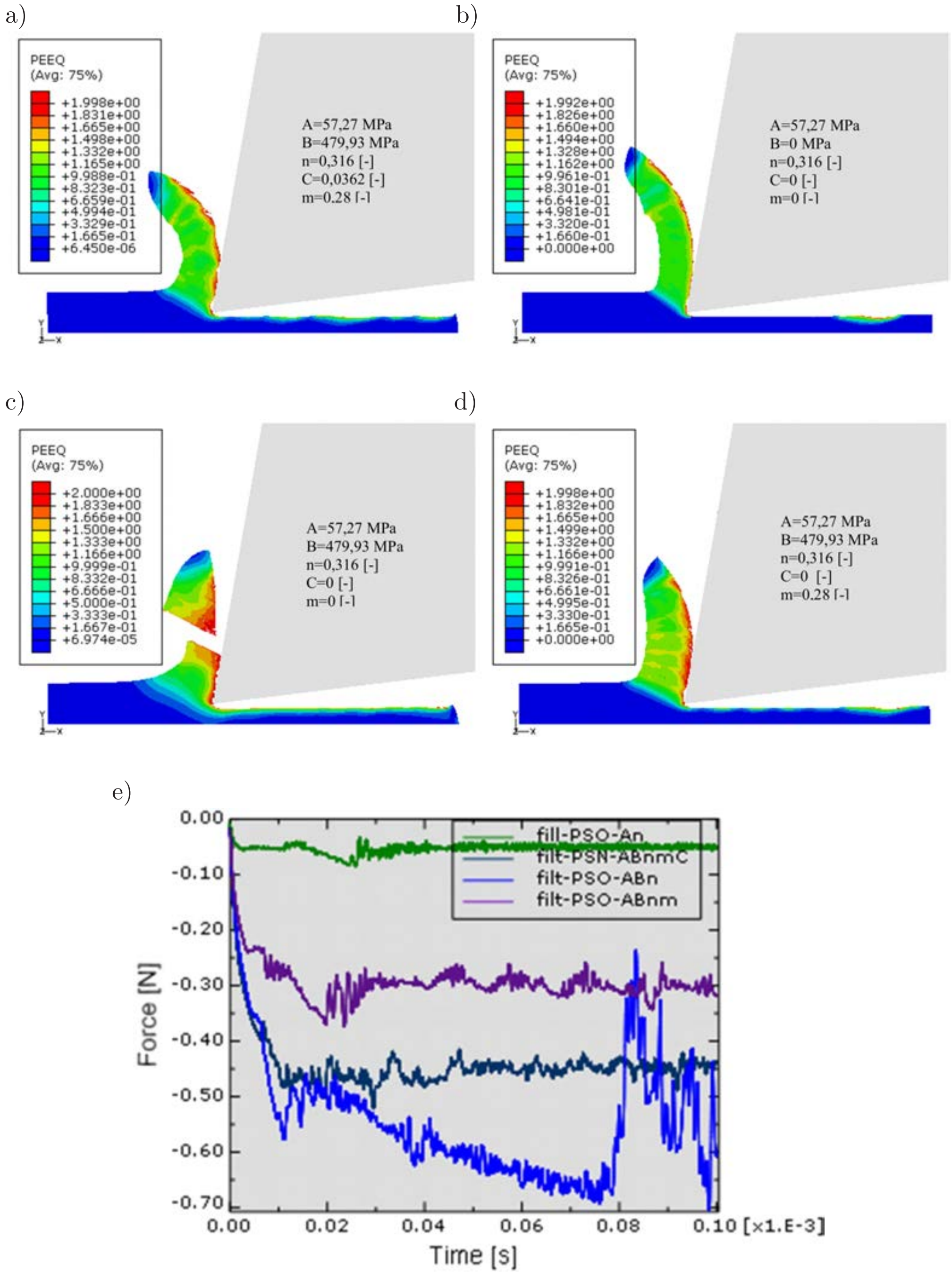

FIG. 8. The maps of equivalent strains for four cases with different effects: a) all effects are included, b) independent yield stress only, c) yield stress with strain hardening, d) yield stress with strain hardening and temperature softening, e) the plot of cutting forces for the all studied cases.

a)

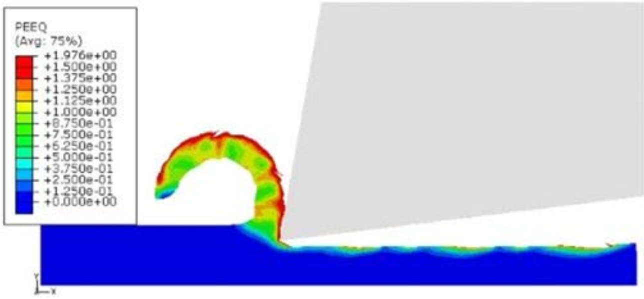

b)

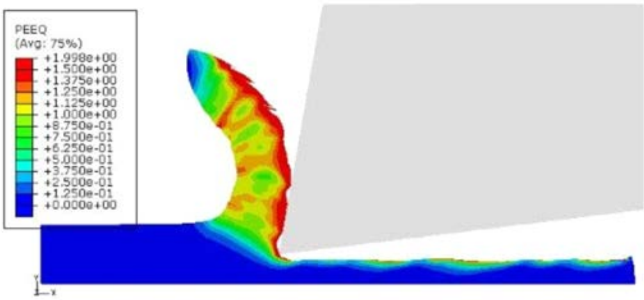

c)

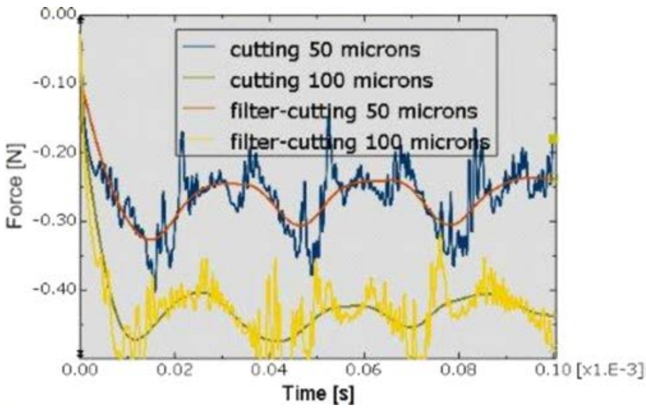

FIG. 9. The maps of equivalent strains for different depth cut cases with: a) 50 μm, b) 100 μm, c) cutting force comparison.

Rusinek-Klepaczko model. The depth of the cut is discussed also in this section for RK model. These results, as before, took into account two depths (50 μm and 100 μm). The comparison of the obtained results is presented in Fig. 10. In Fig. 10c one can observe the history of the cutting force for two cut depths. The force varies in time but the average cutting force for cut depth 100 μm is 0.55 N (in case of JC it was 0.45 N) and for 50 μm is 0.35 N (in case of JC it was 0.27 N).

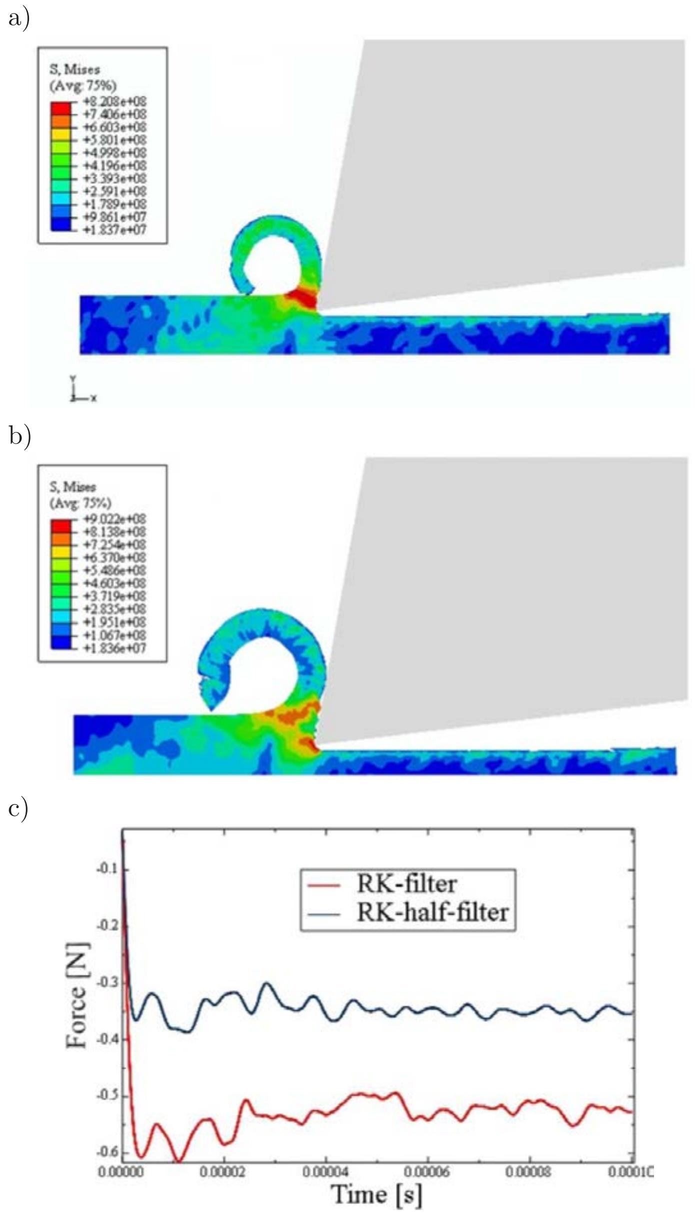

FIG. 10. The maps of equivalent strains for two cases with different depth of cut: a) 50 μm, b) 100 μm, c) cutting force comparison.

Perzyna's type viscoplasticity model. Finally, the results obtained using Perzyna's type viscoplasticity model for the machined sample are discussed. Through the analyses we have accepted mesh refinement or alignment like in previous examples, so we have used C3D8R element with approximate size 10 μm. As a case study we have consider two cut depths (50 μm and 100 μm) and we have repeted the computations with and without adaptive mesh technique (Arbitrary Lagrangian Eulerian (ALE) adaptive mesh technique cf. [1]).

Let us point out, that the analysis with Perzyna's type viscoplasticity model needs additional assumption concerning the initial microdamage state (distribution of $\boldsymbol{\xi}_0$), what has a serious consequences on final macrodamage evolution [32]. Because of lack of detailed experimental data, we have assumed in all analyses homogenous and isotropic initial microdamage state, such that initial porosity was in every material point equal $\|\boldsymbol{\xi}_0\| = 6 \cdot 10^{-4}$ [14]. Notice, that anisotropy introduced by $\boldsymbol{\xi}$ involves full spatial modeling.

Global response

The comparison of the reaction on a tool for cutting depths 50 μm and 100 μm including influence of ALE adaptive mesh technique is presented in Fig. 11. Recall, that those results are the most important for machinery designers. Like for previously presented results an average force that acts on the tool for cutting depth 50 μm is around 0.3 N while for cutting depth 100 μm reaches approximately 0.6 N. Notice, that like in a real experiment resultant force changes due to chip sticking to the tool. Nevertheless this small influence of ALE technique on global level is more distinct on local one concerning e.g. chip geometry and its damage as will be shown in the following.

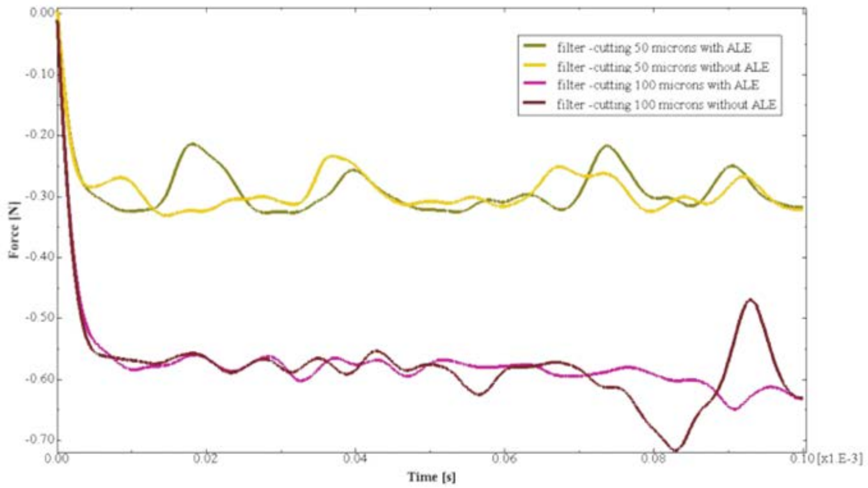

FIG. 11. Comparison of the reaction on the tool for cutting depth 50 μm and 100 μm including influence of ALE adaptive mesh technique.

Local response

The comparison of the HMH stresses, the equivalent viscoplatic strains, the temperature and the porosity maps for cutting depths 50 μm and 100 μm at time instant 10^{-4} s are presented in Figs. 12 and 13, respectively. For both cases

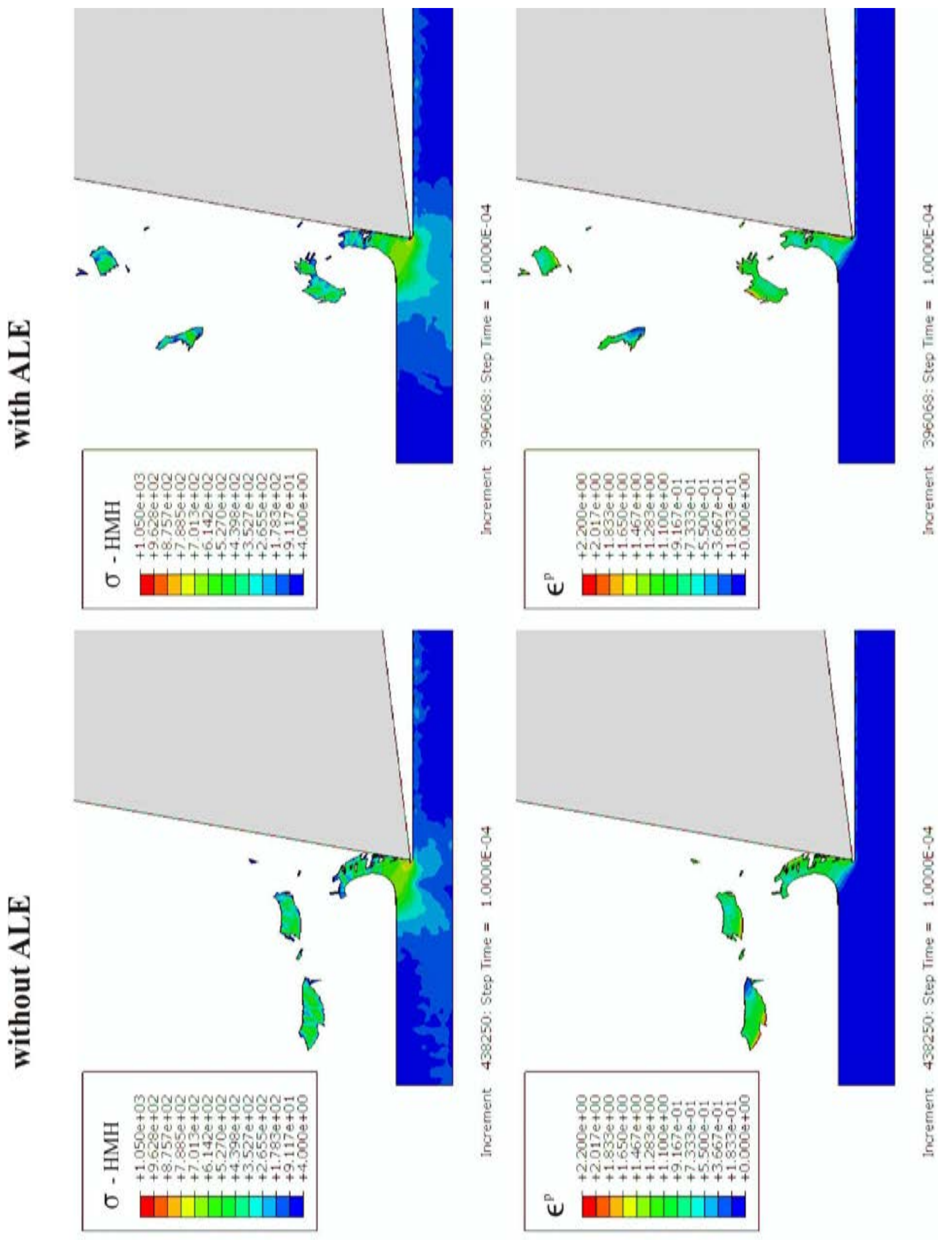
without ALE
with ALE
σ - HMH
+1.050e+03
+9.628e+02
+8.757e+02
+7.885e+02
+7.013e+02
+6.142e+02
+5.270e+02
+4.398e+02
+3.527e+02
+2.655e+02
+1.783e+02
+9.117e+01
+4.000e+00
ε^p
+2.200e+00
+2.017e+00
+1.833e+00
+1.650e+00
+1.467e+00
+1.283e+00
+1.100e+00
+9.167e-01
+7.333e-01
+5.500e-01
+3.667e-01
+1.833e-01
+0.000e+00
Increment 438250: Step Time = 1.0000E-04
Increment 396068: Step Time = 1.0000E-04

[Fig. 12]

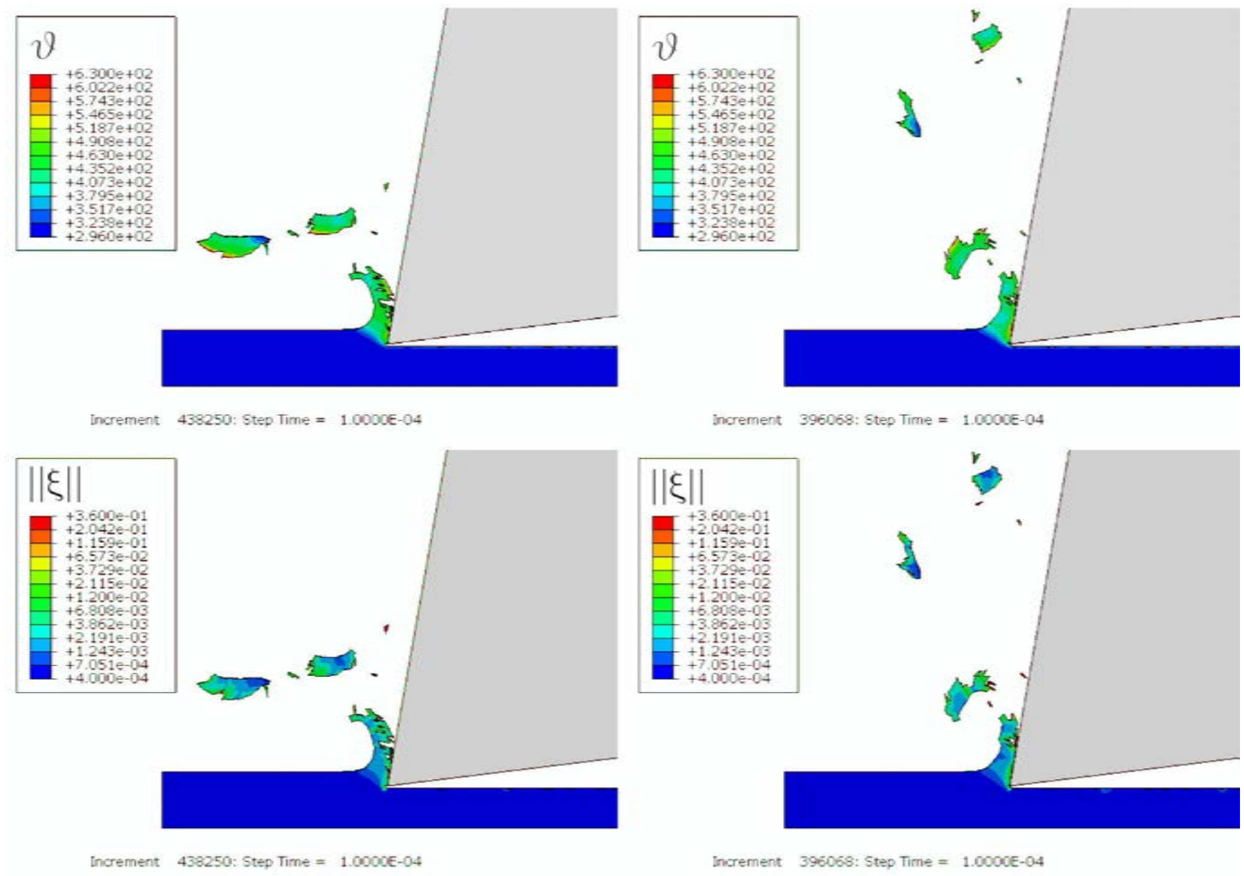

FIG. 12. The comparison of the HMH stresses, the equivalent viscoplatic strains, the temperature and the porosity maps for cutting depth 50 μm at time instant 10^{-4} s, without and with ALE technique in left and right columns, respectively.

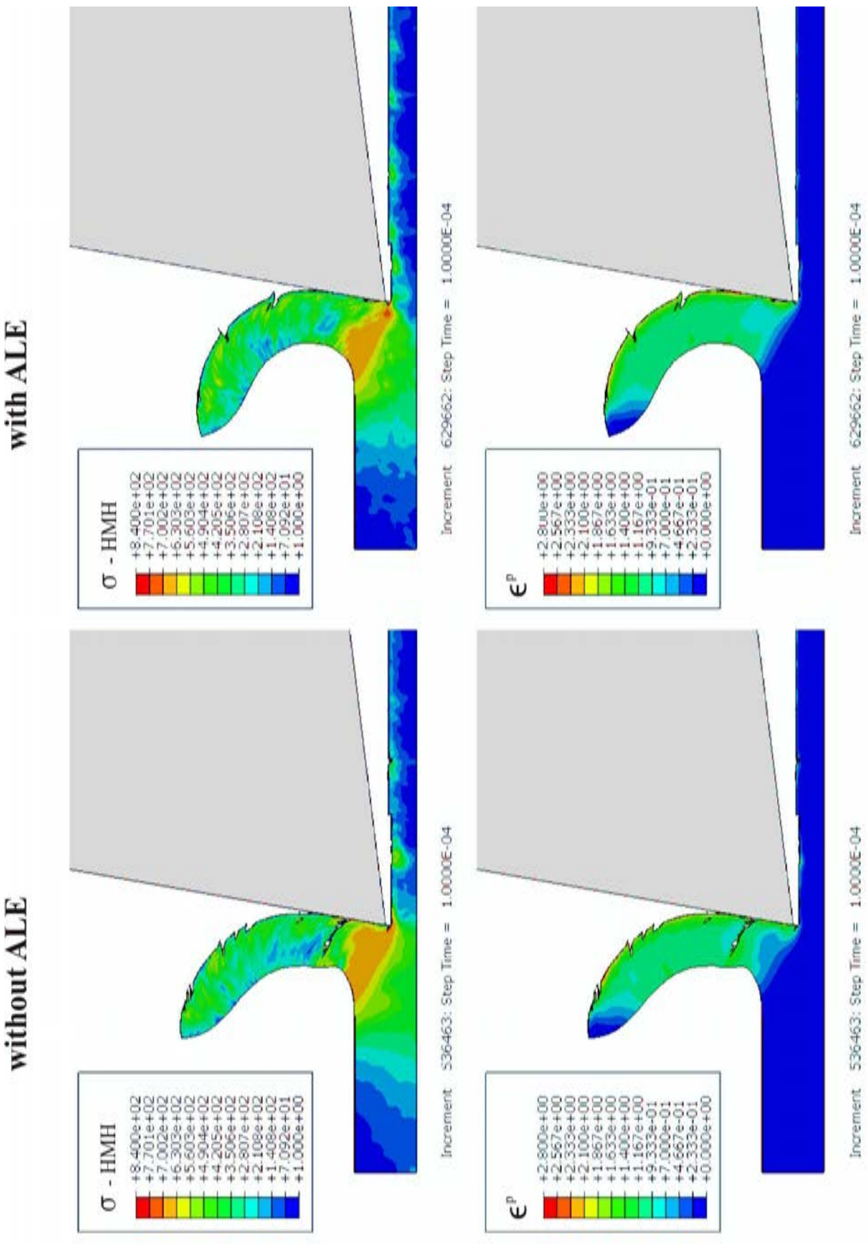

without ALE
with ALE
σ - HMH
+8.400e+02
+7.701e+02
+7.002e+02
+6.303e+02
+5.603e+02
+4.904e+02
+4.205e+02
+3.506e+02
+2.807e+02
+2.108e+02
+1.408e+02
+7.092e+01
+1.000e+00
ϵ^p
+2.800e+00
+2.567e+00
+2.333e+00
+2.100e+00
+1.867e+00
+1.633e+00
+1.400e+00
+1.167e+00
+9.333e-01
+7.000e-01
+4.667e-01
+2.333e-01
+0.000e+00
Increment 536463: Step Time = 1.0000E-04
Increment 629662: Step Time = 1.0000E-04

[Fig. 13]

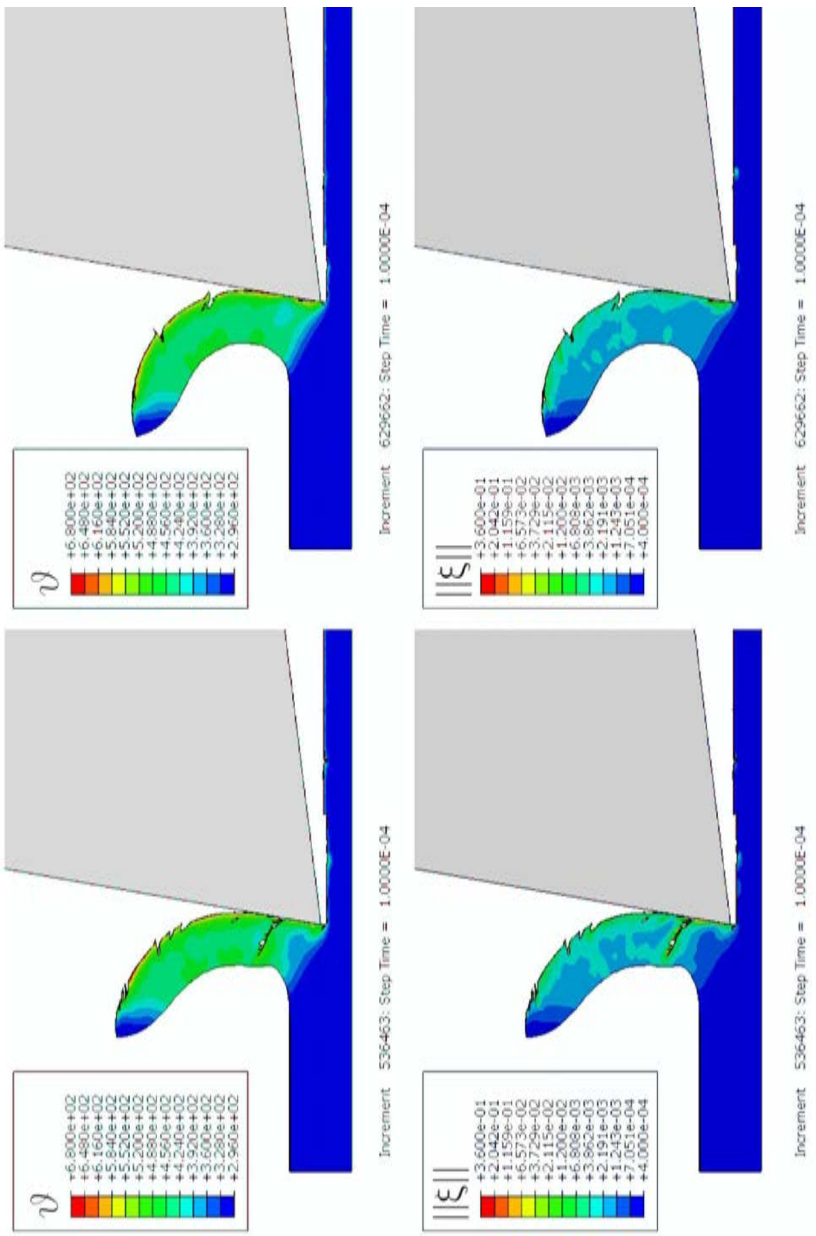

FIG. 13. The comparison of the HMH stresses, the equivalent viscoplatic strains, the temperature and the porosity maps for cutting depth 100 μm at time instant 10^{-4} s, without and with ALE technique in left and right columns, respectively.

we present the results obtained without and with using ALE technique. Notice, that for easier analysis of the maps, each time in rows we use legend with the same upper and lower bounds.

The first notice from Figs. 12 and 13 is that the chip geometry is different. For the case of cutting depth 50 μm it is hard to interpret the difference due to severe fragmentation of the chip, however for cutting depth 100 μm we observe that without ALE technique the chip bends less and there exist a macrodamage. Let us emphasise that fragmentation is due to shear banding.

The maps in Figs. 12 and 13 show that the distribution of presented quantities is very similar. We observe that locally (at a tool tip) the HMH stresses reaches around 1000 MPa, the equivalent viscoplatic strains can obtain even 2.8 and the temperature in close to 680 K. Moreover, the local strain rates (what is not presented graphically), described by the tensor $\mathbf{d}$ (Eq. (2.15), are of the order $4 \cdot 10^6$ s^{-1}. Notice, that cutting of local extrema in plots we have similar results as for previously presented results concerning J-C and RK material models.

4. Conclusions

The comparison of the results that describe the distribution of stresses and strains, influence of mesh refinement and alignment also using ALE formulation as well as friction between tool and specimen were discussed for accepted three constitutive models (JC, RK, and Perzyna). The obtained results differ in details but qualitatively gave very similar effects in particular in estimation of forces that acts on tools.

Using of one of the above constitutive relations in numerical simulations depends significantly on the possibility of proper identification of material parameters. Let us stress at the end that in practical engineering easier accepted are simpler relations (those which have smaller amount of parameters), sometimes not so strongly physically and mathematically proven.

Acknowledgment

The support of the Polish Ministry of Science and Higher Education under grants N N519 419435 and R00 0097 12 is kindly acknowledged.

Prof. A. Rusinek thanks Prof. R. Zaera from UC3M for the development of RK model in ABAQUS.

References

1. *Abaqus Version 6.10ef1 Theory Manual.* 2010.
2. Campbell J.D., *The dynamic yielding of mild steel*, Acta Metallurgica, **1**, 6, 706–710, 1953.

3. Dornowski W., *Influence of finite deformations on the growth mechanism of microvoids contained in structural metals*, Archives of Mechanics, **51**, 1, 71–86, 1999.

4. Glema A., Łodygowski T., Sumelka W., Perzyna P., *The numerical analysis of the intrinsic anisotropic microdamage evolution in elasto-viscoplastic solids*, International Journal of Damage Mechanics, **18**, 3, 205–231, 2009.

5. Johnson G.R., Cook W.H., *A constitutive model and data for metals subjected to large strains, high strain rates and high temperatures*, [in:] Proceedings of the sevens international symposium on ballistics, pp. 541–547, The Hague, The Netherlands, 1983.

6. Klepaczko J.R., *Behavior of rock like materials at high strain rates in compression*, International Journal of Plasticity, **6**, 415–432, 1990.

7. Klepaczko J.R., Rusinek A., Rodríguez–Martínez J.A., Pęcherski R.B., Arias A., *Modelling of thermo-viscoplastic behaviour of DH-36 and Weldox 460-E structural steels at wide ranges of strain rates and temperatures, comparison of constitutive relations for impact problems*, Mechanics of Materials, **41**, 5, 599–621, 2009.

8. Lee E.H., *Elastic-plastic deformation at finite strain*, ASME Journal of Applied Mechanics, **36**, 1–6, 1969.

9. Łodygowski T., *Theoretical and numerical aspects of plastic strain localization*, D.Sc. Thesis, Publishing House of Poznan University of Technology, **312**, 1996.

10. Łodygowski T., Glema A., Sumelka W., *Anisotropy induced by evolution of microstructure in ductile material*, [in:] 8th World Congress on Computational Mechanics (WCCM8), 5th European Congress on Computational Methods in Applied Sciences and Engineering (ECCOMAS 2008), Venice, Italy, June 30 – July 5 2008.

11. Łodygowski T., Perzyna P., *Localized fracture of inelastic polycrystalline solids under dynamic loading process*, International Journal Damage Mechanics, **6**, 364–407, 1997.

12. Łodygowski T., Perzyna P., *Numerical modelling of localized fracture of inelastic solids in dynamic loading process*, International Journal for Numerical Methods in Engineering, **40**, 4137–4158, 1997.

13. Molinari A., Musquar C., Sutter G., *Adiabatic shear banding in high speed machining of Ti-6Al-4V: experiments and modeling*, International Journal of Plasticity, **18**, 443—459, 2002.

14. Nemes J.A., Eftis J., *Several features of a viscoplastic study of plate-impact spallation with multidimensional strain*, Computers and Structures, **38**, 3, 317–328, 1991.

15. Nemes J.A., Eftis J., *Constitutive modelling of the dynamic fracture of smooth tensile bars*, International Journal of Plasticity, **9**, 2, 243–270, 1993.

16. Perzyna P., *The constitutive equations for rate sensitive plastic materials*, Quarterly of Applied Mathematics, **20**, 321–332, 1963.

17. Perzyna P., *Fundamental problems in viscoplasticity*, Advances in Applied Mechanics, **9**, 243–377, 1966.

18. Perzyna P., *Constitutive modelling for brittle dynamic fracture in dissipative solids*, Archives of Mechanics, **38**, 725–738, 1986.

19. Perzyna P., *Internal state variable description of dynamic fracture of ductile solids*, International Journal of Solids and Structures, **22**, 797–818, 1986.

20. Perzyna P., *Instability phenomena and adiabatic shear band localization in thermoplastic flow process*, Acta Mechanica, **106**, 173–205, 1994.

21. Perzyna P., *The thermodynamical theory of elasto-viscoplasticity*, Engineering Transactions, **53**, 235–316, 2005.

22. Perzyna P., The thermodynamical theory of elasto-viscoplasticity accounting for microshear banding and induced anisotropy effects. Mechanics, **27**, 1, 25–42, 2008.

23. Rusinek A., Klepaczko J.R., *Shear testing of a sheet steel at wide range of strain rates and a constitutive relation with strain-rate and temperature dependence of the flow stress*, International Journal of Plasticity, **17**, 1, 87–115, 2001.

24. Rusinek A., Rodríguez–Martínez J.A., *Thermo-viscoplastic constitutive relation for aluminium alloys, modeling of negative strain rate sensitivity and viscous drag effects*, Materials and Design, **30**, 10, 4377–4390, 2009.

25. Rusinek A., Rodríguez–Martínez J.A., Arias A., *A thermo-viscoplastic constitutive model for FCC metals with application to OFHC copper*, International Journal of Mechanical Sciences, **52**, 2, 120–135, 2010.

26. Rusinek A., Rodríguez–Martínez J.A., Klepaczko J.R., Pęcherski R.B., *Analysis of thermo-visco-plastic behaviour of six high strength steels*, Materials and Design, **30**, 5, 1748–1761, 2009.

27. Rusinek A., Zaera R., *Finite element simulation of steel ring fragmentation under radial expansion*, International Journal of Impact Engineering, **34**, 799—822, 2007.

28. Rusinek A., Zaera R., Klepaczko J.R., *Constitutive relations in 3-*D *for a wide range of strain rates and temperatures: Application to mild steels*, International Journal of Solids and Structures, **44**, 17, 5611–5634, 2007.

29. Shima S., Oyane M., *Plasticity for porous solids*, International Journal of Mechanical Sciences, **18**, 285–291, 1976.

30. Sima M., Özel T., *Modified material constitutive models for serrated chip formation simulations and experimental validation in machining of titanium alloy Ti-6Al-4V*, International Journal of Machine Tools and Manufacture, **50**, 943—960, 2010.

31. Sumelka W., *The Constitutive Model of the Anisotropy Evolution for Metals with Microstructural Defects*, Publishing House of Poznan University of Technology, Poznań, Poland, 2009.

32. Sumelka W., Łodygowski T., *The influence of the initial microdamage anisotropy on macrodamage mode during extremely fast thermomechanical processes*, Archive of Applied Mechanics, **81**, 12, 1973–1992, 2011.

33. Truesdell C., Noll W., *The non-linear field theories of mechanics*, [in:] Handbuch der Physik, vol. III/3, Springer-Verlag, Berlin, S. Flügge [Ed.], 1965.

34. Zaera R., Fernández–Sáez J., *An implicit consistent algorithm for the integration of thermoviscoplastic constitutive equations in adiabatic conditions and finite deformations*, International Journal of Solids and Structures, **43**, 6, 1594–1612, 2006.

Received September 29, 2011; revised version March 12, 2012.

DIRECTIONS FOR THE AUTHORS

The periodical *ENGINEERING TRANSACTIONS (ROZPRAWY INŻYNIERSKIE)* presents original papers which should not be published elsewhere.

As a rule, the volume of a paper should not exceed 40 000 typographic signs. The following directions are particularly important:

1. **The paper submitted for publication should be written in English.**
2. The title of the paper should be as short as possible. The text should be preceded by a brief introduction; it is also desirable that a list of notations used in the paper should be given.
3. Short papers should be divided into section and subsection, long papers into sections, subsections and points. Each section, subsection or point must bear a title.
4. The formula number consists of two figures: the first represents the section number and the other the formula number in that section. Thus the division into subsections does not influence the numbering of formulae. Only such formulae should be numbered to which the author refers throughout the paper. This also applies to the resulting formulae. The formula number should be written on the left-hand side of the formula; round brackets are necessary to avoid any misunderstanding. For instance, if the author refers to the third formula of the set (2.1), a subscript should be added to denote the formula, viz. $(2.1)_3$.
5. All the notations should be written very distinctly. Special care must be taken to distinguish between small and capital letters as precisely as possible. Semi-bold type must be underlined in black pencil. Explanations should be given on the margin of the manuscript in case of special type face.
6. Vectors are to be denoted by semi-bold type, transforms of the corresponding functions by tildes symbols. Trigonometric functions are denoted by sin, cos, tg and ctg, inverse functions – by arc sin, arc cos, arc tg and arc ctg; hyperbolic functions are denoted by sh, ch, th and cth, inverse functions – by Arsh, Arch, Arth and Arcth.
7. The figures in square brackets denote reference titles. Items appearing in the reference list should include the initials of the first name of the author and his surname, also the full of the paper (in the language of the original paper); moreover;
   a) In the case of books, the publisher's name, the place and year of publication should be given, e.g., 5. S. Ziemba, *Vibration analysis*, PWN, Warszawa 1970;
   b) In the case of a periodical, the full title of the periodical, consecutive volume number, current issue number, pp. from ... to ..., year of publication should be mentioned; the annual volume number must be marked in semi-bold type as to distinguish it from the current issue number, e.g., 6. M. Sokołowski, *A thermoelastic problem for a strip with discontinuous boundary conditions*, Arch. Mech., **13**, 3, 337–354, 1961.
8. The authors should enclose a summary of the paper. The volume of the summary is to be about 100 words, also key words are requested.
9. The preferable format for the source file is TeX or LaTeX while MS Word is also acceptable. Separate files for the figures should be provided in one of the following formats: EPS or PostScript (preferable), PDF, TIFF, JPEG, BMP, of at least 300 DPI resolution. The figures should be in principle in gray-scale and only if necessary the color will be accepted.

Upon receipt of the paper, the Editorial Office forwards it to the reviewer. His opinion is the basis for the Editorial Committee to determine whether the paper can be accepted for publication or not.

Once the paper is printed, the issue of Engineering Transactions free of charge is sent to the author. Also the PDF file of the paper is forwarded by the e-mail to the authors.

Editorial Committee
ENGINEERING TRANSACTIONS